Surface Acoustic Wave Filters on Diamond Layered Structures

By

HIROYUKI KITABAYASHI, B.Sc., M.Sc.

A Thesis
Submitted to the School of Graduate Studies
in Partial Fulfilment of the Requirements
for the Degree
Doctor of Philosophy

McMaster University

Surface Acoustic Wave Filters on Diamond Layered Structures

DOCTOR OF PHILOSOPHY (2001)
(Electrical and Computer Engineering)

MCMASTER UNIVERSITY
Hamilton, Ontario

TITLE: **Surface Acoustic Wave Filters on Diamond Layered Structures**

AUTHOR: Hiroyuki Kitabayashi
B.Sc., M.Sc. (The University of Tokyo, Tokyo, Japan)

SUPERVISOR: Dr. Peter M. Smith

NUMBER OF PAGES: xiv, 143

Abstract

Surface acoustic wave (SAW) devices are an enabling technology for high-performance wireless communication systems. They are able to meet performance specifications that are beyond the scope of competing technologies, particularly in the front-end of the receivers, and establish the ultimate performance that is achievable. Current spectrum congestion is forcing a move to higher operating frequencies, and this is leading to a search for low-cost SAW devices that are able to operate at frequencies above 2 GHz. To this end, there has been considerable interest in devices that employ the high acoustic velocity of diamond. Diamond, however, is not piezoelectric, and it must be layered with other materials such as zinc oxide (ZnO) to permit the electrical generation and detection of acoustic waves. There is therefore a need for modeling tools that accurately predict the behaviour of multi-layered SAW substrates in the presence of surface transducers and reflectors.

This Thesis presents a study of SAW propagation and generation under infinite periodic grating structures on multi-layered ZnO/Diamond substrates. The study is based on the space harmonic method (SHM) and predicts the SAW behaviour under both open and shorted surface electrodes. Dispersion diagrams are obtained around the first Bragg wavenumber and stopbands of finite bandwidth are observed. The method is then extended to the generation of SAWs by interdigital transducers. Admittance curves and static capacitances are calculated. The physical propagation behaviour of ZnO/Diamond multi-layered substrates is also investigated. The displacement distributions and the standing wave patterns are calculated within each layer. The energy contained in each layer is computed for different propagation modes and different ZnO layer thicknesses.

The results are interpreted within the framework of the coupling-of-modes (COM) theory. The COM parameters are derived for the first and second Sezawa modes as a function of aluminum and zinc oxide thicknesses. The results and the COM parameters can be directly used in the design of SAW devices. The established analytical treatments can be easily applied to other multi-layered substrates with an arbitrary configuration including additional layers.

Acknowledgements

I would like to express deep gratitude to my supervisor Dr. P.M. Smith for his continuous help and support throughout this study. I am very grateful and proud to have worked under his supervision. I would also like to deeply thank Dr. D. Conn and Dr. P. Jessop, members of my supervisory committee, for their guidance and suggestions to this Thesis.

I am pleased to acknowledge the financial support of Sumitomo Electric Industries, Ltd., Japan (SEI) who gave me the opportunity to study at McMaster University. The financial support provided by the Nortel Networks, Canada is gratefully acknowledged.

I also would like to thank my superior Mr. S. Shikata at SEI, without whom I would have never dreamed of studying abroad.

I particularly wish to show my appreciation to my family, especially to my wife, Akiko and our lovely son, Ryota, for their continuous supports, patience and smiles.

Contents

1 Introduction 1

1.1 Surface Acoustic Waves 4

1.2 Surface Acoustic Wave Filters 9

1.3 Diamond SAW Filters 12

1.4 SAW Filter Design 14

1.5 Motivation of This Study 17

1.6 Scope of the Thesis 18

2 Coupling-of-Modes Theory 22

2.1 Introduction 22

2.2 COM Description 24

2.3 Low Loss Approximation 28

2.4 Dispersion Analysis using COM Theory 31

2.4.1 Dispersion Relation 31

2.4.2 Derivation of Coupling Coefficients 33
2.4.3 Derivation of Transduction Coefficient 37
2.5 Admittance Curve using the COM Equations 39
2.6 COM Parameter Derivation Using Admittance Curve 41
2.7 Conclusion 44

3 Space Harmonic Method 46

3.1 Introduction 46
3.2 Space Harmonic Method 48
3.2.1 Floquet's Theorem 48
3.2.2 Space Harmonic Solutions 49
3.2.3 Boundary Condition Integral 55
3.2.4 The Procedure for Simulation 63
3.2.5 Energy Distribution 64
3.3 Results and Discussion 68
3.3.1 Dispersion Diagram 69
3.3.2 Displacement Distribution 78
3.3.3 Energy distribution 91
3.3.4 COM Parameter Derivation 104
3.4 Generation Problem 108

3.4.1 Space Harmonic Description 108

3.4.2 The Procedure for Simulation 117

3.5 Results and Discussion for the Generation Problem 119

3.6 Conclusion 127

4 Conclusion **131**

4.1 Suggestions for future work 133

List of Tables

3.1 Energy inside each layer at the lower stopband edge for shorted gratings normalized to the total wave energy inside ZnO. $H_A = 0.03P$. 103

3.2 Energy inside each layer at the lower stopband edge for shorted gratings normalized to the total wave energy inside ZnO. $H_A = 0.03P$. 103

3.3 Energy inside the diamond up to specified depth for the second mode when $H_Z = P/\pi$ and $H_A = 0.03P$. 105

3.4 Energy inside the diamond up to specified depth for the first mode when $H_Z = 1.75P/\pi$ and $H_A = 0.03P$. 105

List of Figures

1.1 Slowness curves of ZnO. 6

1.2 Instantaneous displacement for the Rayleigh wave in isotropic material [5]. 8

1.3 The typical displacement for the Rayleigh wave in isotropic material [5]. 8

1.4 Typical SAW filter 10

1.5 The typical Diamond SAW filter based on the ZnO/Diamond substrate. 13

2.1 Grating structure with grating period Λ. 25

2.2 The dispersion diagram for shorted gratings without the propagation loss. 34

3.1 A periodic Al grating structure on a ZnO/Diamond substrate. 51

3.2 Slowness curves for the diamond. 56

3.3 The mechanical and the electrical boundary conditions. 58

3.4 Block diagram of our calculation procedure. 65

3.5 SAW velocity of the ZnO/Diamond substrate as a function of the ZnO thickness. 70

3.6 Dispersion curves of the second Sezawa wave under a infinite periodic grating structure, where $H_Z = P/\pi$ and $H_A = 0$. 71

3.7 Dispersion curves of the second Sezawa wave under an infinite periodic grating structure, where $H_Z = P/\pi$ and $H_A = 0.03P$. 73

3.8 Dispersion curves of the second Sezawa wave under an infinite periodic grating structure, where $H_Z = 1.5P/\pi$ and $H_A = 0.03P$. 74

3.9 The stopband widths of the second Sezawa wave when $H_Z = P/\pi$ as a function of Al grating thickness. 76

3.10 Dispersion curves of the first Sezawa wave under an infinite periodic grating structure, where $H_Z = 1.75P/\pi$ and $H_A = 0.03P$. 77

3.11 Displacement distribution of the second Sezawa mode inside Al/ZnO/Diamond structure at $t = 0$ for shorted gratings at the lower stopband edge for $H_Z = P/\pi$ and $H_A = 0.03P$. 79

3.12 Displacement distribution of the second Sezawa mode inside Al/ZnO/Diamond structure at $t = 0$ for shorted gratings at the lower stopband edge for $H_Z = P/\pi$ and $H_A = 0.03P$. 81

3.13 Displacement distribution of the first Sezawa mode inside Al/ZnO/Diamond structure at $t = 0$ for shorted gratings at the lower stopband edge for $H_Z = 1.75P/\pi$ and $H_A = 0.03P$. 82

3.14 Displacement distribution of the first Sezawa mode inside Al/ZnO/Diamond structure at $t = 0$ for shorted gratings at the lower stopband edge for $H_Z = 1.75P/\pi$ and $H_A = 0.03P$. 83

3.15 Standing wave pattern of the second mode at the lower stopband edge for shorted gratings when $H_Z = P/\pi$ and $H_A = 0.03P$. 84

3.16 Standing wave pattern of the second mode at the upper stopband edge for shorted gratings when $H_Z = P/\pi$ and $H_A = 0.03P$. 85

3.17 Standing wave pattern of the second mode at the stopband center for shorted gratings when $H_Z = P/\pi$ and $H_A = 0.03P$. 86

3.18 Standing wave pattern of the second mode at the lower stopband edge for shorted gratings when $H_Z = P/\pi$ and $H_A = 0.005P$. 88

3.19 Standing wave pattern of the second mode at the upper stopband edge for shorted gratings when $H_Z = P/\pi$ and $H_A = 0.005P$. 89

3.20 Standing wave pattern of the second mode at the stopband center for shorted gratings when $H_Z = P/\pi$ and $H_A = 0.005P$. 90

3.21 Standing wave pattern of the first Sezawa mode at the lower stopband edge for shorted gratings when $H_Z = 1.75P/\pi$ and $H_A = 0$. 92

3.22 Standing wave pattern of the first Sezawa mode at the upper stopband edge for shorted gratings when $H_Z = 1.75P/\pi$ and $H_A = 0$. 93

3.23 Standing wave pattern of the first Sezawa mode at the lower stopband edge for shorted gratings when $H_Z = 1.75P/\pi$ and $H_A = 0.03P$. . . . 94

3.24 Standing wave pattern of the first Sezawa mode at the upper stopband edge for shorted gratings when $H_Z = 1.75P/\pi$ and $H_A = 0.03P$. . . . 95

3.25 Standing wave pattern of the first Sezawa mode at the stopband center for shorted gratings when $H_Z = 1.75P/\pi$ and $H_A = 0.03P$. 96

3.26 Energy density distribution of the second Sezawa mode inside ZnO layer at the lower stopband edge for shorted gratings when $H_Z = P/\pi$ and $H_A = 0.03P$. 97

3.27 Energy density distribution of the second Sezawa mode inside diamond layer at the lower stopband edge for shorted gratings when $H_Z = P/\pi$ and $H_A = 0.03P$. 98

3.28 Energy density distribution of the second Sezawa mode inside ZnO layer at the stopband center for shorted gratings when $H_Z = P/\pi$ and $H_A = 0.03P$. 99

3.29 Energy density distribution of the second Sezawa mode inside diamond layer at the stopband center for shorted gratings when $H_Z = P/\pi$ and $H_A = 0.03P$. 100

3.30 The coupling-of-modes (COM) parameters as a function of Al thickness for the second Seazwa mode. 106

3.31 The coupling-of-modes (COM) parameters as a function of Al thickness for the first Sezawa mode. 109

3.32 An infinite grating structure on ZnO/Diamond substrate. 110

3.33 The equivalent circuit for one electrode pair. 116

3.34 A flowchart of our calculation procedure. 118

3.35 The real part of the total charge as a function of the normalized frequency when $H_Z = P/\pi$ and $H_A = 0.005P$. 120

3.36 The static capacitance for one electrode pair per unit length as a function of Al grating thickness. 122

3.37 The admittance curves for the second Sezawa mode when $H_Z = P/\pi$ and $H_A = 0.005P$. 123

3.38 The calculated conductance curves for the second Sezawa mode when $H_Z = P/\pi$ and $H_A = 0.005P$ where only the contributions from the positive travelling waves are summed up. 125

3.39 The conductance curves for the second Sezawa mode when $H_Z = P/\pi$ and $H_A = 0.005P$ calculated from the Hilbert transform. 126

3.40 Displacement distribution of the second Sezawa mode for an applied voltage of $1(V)$. $H_Z = P/\pi$ and $H_A = 0.005P$. $f \cdot 2P = 11,544(m/s)$. 128

Chapter 1

Introduction

Surface acoustic wave (SAW) is a general term for the type of mechanical waves which concentrate all or most of their energies on the surface area of a solid. This behaviour is in contrast to bulk waves, where the energy propagates throughout the solid.

Amongst all, the most popular SAW is the Rayleigh wave, which was predicted theoretically for free boundary surfaces on semi infinite isotropic elastic bodies by Lord Rayleigh in 1885 [1] and observed experimentally in earthquakes. The phase velocity of Rayleigh wave is lower than that of any bulk waves. Since then, surface waves have been extensively investigated in the seismology field. In 1935, so-called Sezawa waves were analysed on an isotropic plate over an isotropic half space [2]. These waves were later shown to be higher order Rayleigh modes. The application of Sazawa type waves is being researched nowadays in order to realize a high velocity SAW and multiple desired properties such as simultaneous high velocity and temperature stability.

Because the SAW is concentrated on the surface of the substrate, it can be easily excited or detected on the surface. In the field of signal processing, surface acoustic wave devices were not practical until the invention of the interdigital transducer (IDT) by R. M. White and F. W. Voltmer in 1965 [3]. Since then, a variety of sophisticated SAW devices have been invented and are in use in most modern communication systems.

The recent trend is to realize high frequency SAW devices for current high speed communication systems. One way to realize this goal is to reduce the wavelength of the SAW, because the frequency of the wave is inversely proportional to the wavelength. This needs a reduction of the IDT period, in other words, a reduction of the electrode width, which, however, is limited by the lithographic resolution in the fabrication of the IDT's. The other solution is to increase the phase velocity of the SAW. For this purpose, several types of leaky SAW and new materials with higher SAW velocity have been investigated. The phase velocity of a leaky SAW is faster than that of the Rayleigh SAW, and it ranges from around 4,000 m/s for quartz to 7,500 m/s for lithium tetraborate ($Li_2B_4O_7$). As an alternative, Diamond has attracted a great deal of attention as a new material with high phase velocity of over 10,000 m/s. However, the Diamond substrate doesn't have a piezoelectricity, which requires the piezoelectric layer for the electrical wave excitation and detection. The multi-layered nature of the Diamond substrates cause dispersion that is a function of the piezoelectric material thickness. This means that the SAW propagation and generation properties such as phase velocity, temperature stability and electro-mechanical coupling are dependent on the substrate thickness conditions. The quantification of properties that is necessary for SAW filter design and the specification of these is becoming more and more stringent. The substrate properties have been usually derived from the experiments. For multi-layered substrates, however, this requires expensive and time consuming experiments that must be repeated for each thickness condition, making a complete characterization unrealistic. Therefore, it is especially necessary to establish a rigorous theoretical treatment of SAW propagation and excitation which can predict SAW properties precisely for multi-layered substrates.

A theoretical study is also necessary if one is to exploit potential properties of multi-layer substrates such as high coupling and temperature stability, which are usually contradictory on semi-infinite substrates. The physical behaviour inside multi-layered structure is also interesting, because the wave property will be governed partially by each layer simultaneously.

For these reasons, we will establish a rigorous analytical method to describe the SAW propagation on multi-layered substrates using the space harmonic method (SHM). The SHM is then extended to the SAW generation problem. From these theoretical analyses, the SAW design parameters will be derived precisely for Al/ZnO/Diamond multi-layered substrates.

In this chapter, we will discuss the propagation of surface acoustic waves, the principle of SAW devices and of Diamond SAW filters. With this background, the motivation of this study will be restated, where the significance and the kernel of this study will be emphasized. Finally, the major contribution of this Thesis will be summarised.

1.1 Surface Acoustic Waves

Acoustic waves propagating inside piezoelectric materials are governed by Newton's equation of motion and Maxwell's equation under the quasi-static approximation

$$\rho\frac{\partial^2\mathbf{U}}{\partial t^2}=\nabla\cdot\mathbf{T}=\nabla\cdot(\mathbf{c}\cdot\mathbf{S}-\mathbf{e}\cdot\mathbf{E}) \tag{1.1}$$

$$\nabla\cdot\mathbf{D}=0 \tag{1.2}$$

where **U** is the particle displacement, **T** and **S** are the stress and the strain, respectively. **D** and **E** are the electrical displacement and the electrical field, **c** and **e** are the elastic and the piezoelectric tensors. ρ is the mass density.

The plane wave solution to these equations, with frequency ω, has fields proportional to

$$\exp\{j(\mathbf{k}\cdot\mathbf{r}-\omega t)\} \tag{1.3}$$

where **k** is a wavenumber vector. The plane wave solution assumes an infinitely long line source of the wave, and this will usually hold for SAW excitation with IDT's. In fact, throughout our analysis, we will assume that the wave excitation line source, IDT, is long enough in the y direction so that the spatial variation of the wave is uniform in that direction, and $\mathbf{k} = (k_x, 0, k_z)$.

The above governing equations give us an 8th order polynomial in terms of k_z for each specific value of k_x. 8 solutions of this polynomial can be classified into 4 pairs according to their dominant spatial components, which are:

1. electromagnetic wave
2. quasi longitudinal acoustic wave
3. quasi fast shear acoustic wave
4. quasi slow shear acoustic wave

The solutions for three acoustic waves can be plotted as a function of propagation direction. The result is called a slowness curve. The slowness curve for Zinc Oxide (ZnO) is shown in fig. 1.1. Right-handed Euler angle of ZnO is <0°, 0°, 0° >. x and z are along the a-axis and c-axis of the crystal, respectively. In this figure, $k_{x,ss}/\omega$ corresponds to the intersection between the quasi slow shear wave slowness curve and the positive k_x/ω axis and to the branch point below which the quasi slow shear partial wave becomes bulky. Similarly, $k_{x,fs}/\omega$ and $k_{x,l}/\omega$ are the intersections between the slowness curves and the positive k_x/ω axis for the quasi fast shear wave and quasi longitudinal wave, respectively.

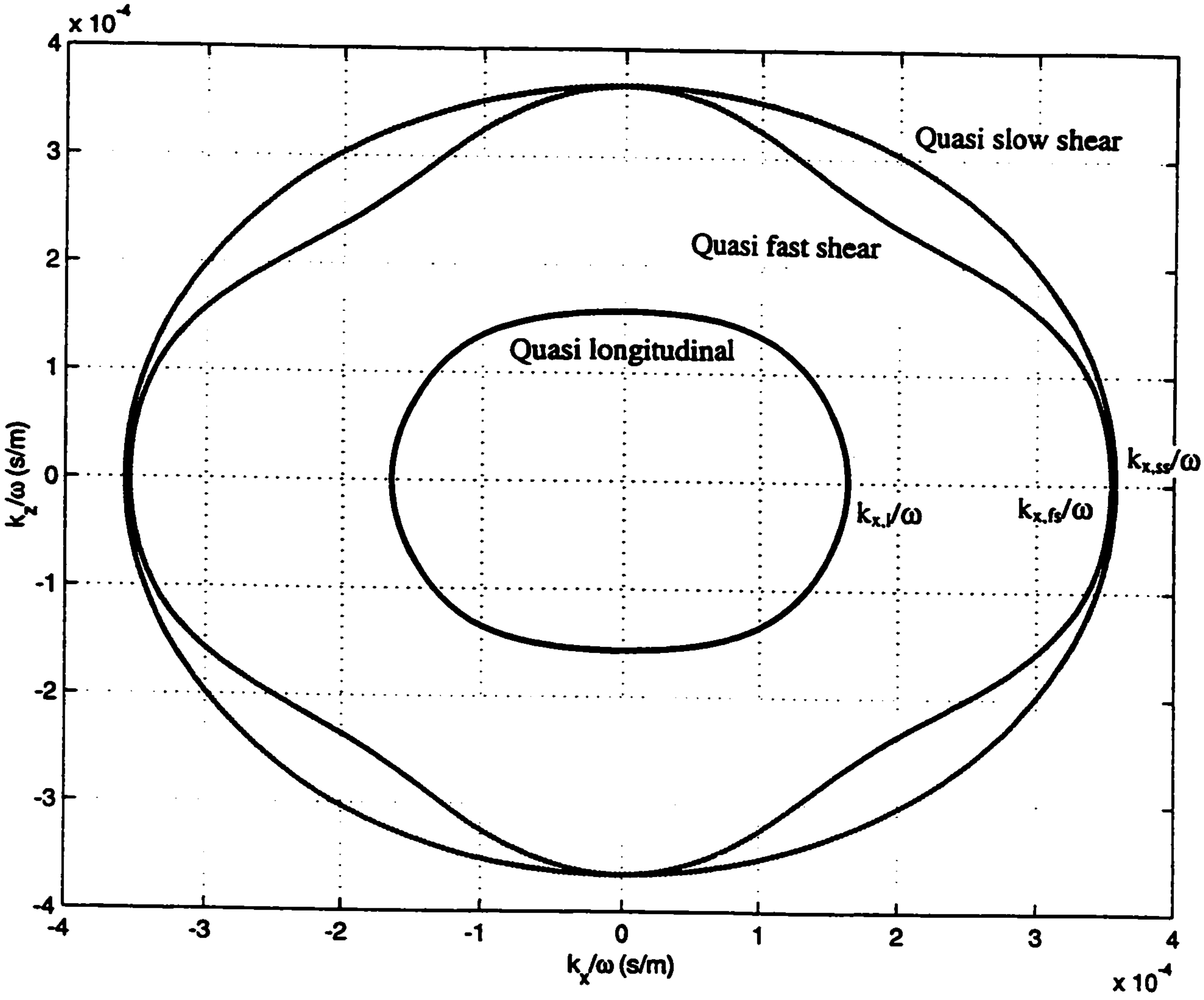

Figure 1.1: Slowness curves of ZnO.

For k_x larger than $k_{x,ss}$, the solution for k_z, in general, consists of 4 complex conjugate pairs. A value of k_z with a negative imaginary part corresponds to a partial wave decaying in the negative z direction. On the other hand, the positive imaginary part corresponds to a partial wave increasing in the negative z direction.

Now, consider a semi-infinite material which lies in the negative z direction. For given k_x ($k_x > k_{x,ss}$), we can construct the wave from the 4 partial waves which have negative imaginary components, because the amplitudes of the partial waves with positive imaginary parts grow exponentially inside the material and these partial waves can't be allowed due to physical considerations. The resulting wave is concentrated on the surface with no energy flow in the z direction. This type of wave is called a generalized Rayleigh wave and the phase velocity is in general determined by numerical computations. The Rayleigh wave is a special form of this generalized Rayleigh wave inside the isotropic material. It can be constructed from the longitudinal and the vertical shear waves coupled together to satisfy the boundary conditions. The phase velocity for a Rayleigh wave in an isotropic material, can be given by the analytic form as follows [4].

$$\left(\frac{V_R}{V_s}\right)^6 - 8\left(\frac{V_R}{V_s}\right)^4 + 8\left\{3 - 2\left(\frac{V_s}{V_l}\right)^2\right\}\left(\frac{V_R}{V_s}\right)^2 - 16\left\{1 - \left(\frac{V_s}{V_l}\right)^2\right\} = 0 \qquad (1.4)$$

where V_R, V_s and V_l are the phase velocity of Rayleigh wave, shear wave and longitudinal wave, respectively.

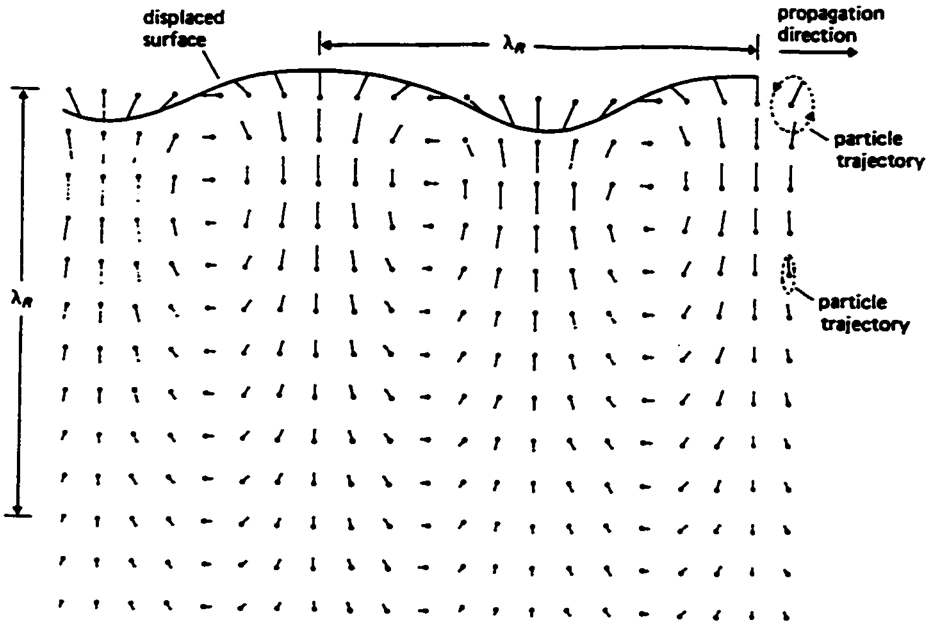

Figure 1.2: Instantaneous displacement for the Rayleigh wave in isotropic material [5].

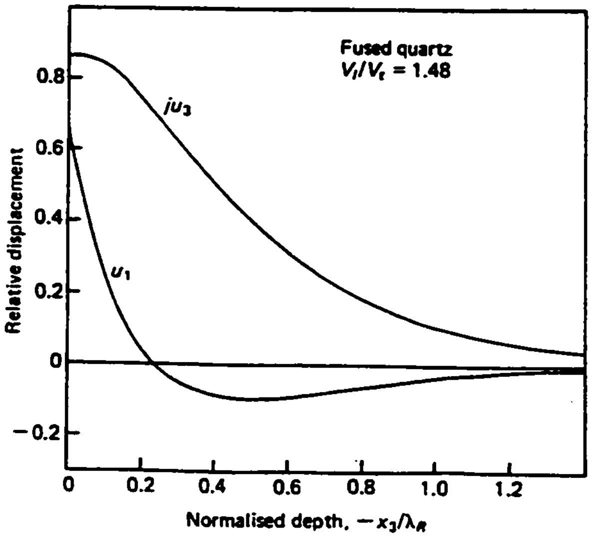

Figure 1.3: The typical displacement for the Rayleigh wave in isotropic material (u_1 is the displacement of the direction of propagation, u_3 is the displacement in the direction perpendicular to the surface) [5].

Fig. 1.2 and fig. 1.3 show the field pattern of the Rayleigh wave. The displacement u_3 in the z direction is in quadrature with u_1 in the x direction. Therefore, the particle motion is an ellipse. At the surface, the motion is retrograde, while it is prograde below the surface.

If the given k_x is less than the value of the slow shear wave ($k_x < k_{x,ss}$), some of the k_z solutions become pure real values. This means that part of the energy flows into the material and is no longer concentrated on the surface. This type of wave is called a leaky SAW and its phase velocity is higher than that of the Rayleigh wave, because k_x is less than that of SAW and the phase velocity is $v = \omega/k_x$. For some cases, the propagation loss due to this energy leakage is acceptable and leaky SAW can be used for practical SAW devices.

1.2 Surface Acoustic Wave Filters

SAW devices are electrical devices that utilize conversions between acoustic waves and electric signals on piezoelectric substrates. They can be classified into filters, delay lines, resonators, convolvers and so on. Fig. 1.4 shows the typical structure of the SAW filter. The input and the output IDT's are fabricated on top of a piezoelectric substrate. At the input IDT, the applied ac electric signal induces an acoustic wave due to the piezoelectricity of the substrate. The traveling SAW is reconverted into an electric signal at the output IDT.

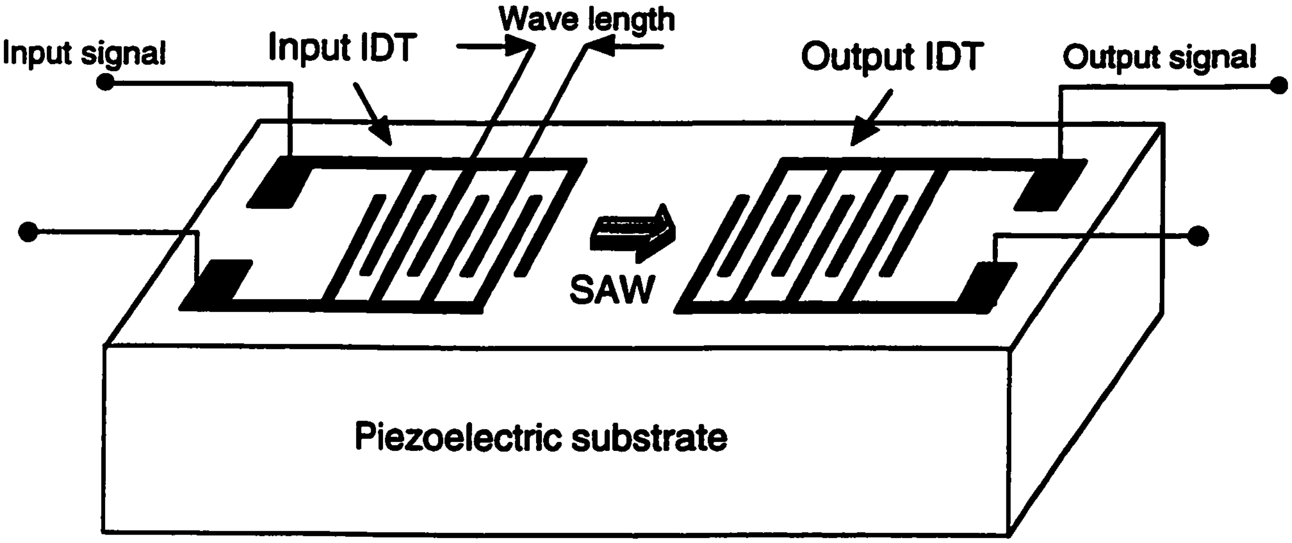

Figure 1.4: Typical SAW filter

The frequency, f, of the applied signal will satisfy the following relation

$$v = f\lambda \tag{1.5}$$

where v is the phase velocity of SAW and λ is the wavelength of the wave. In order to get the efficient conversion, λ must correspond to the period between IDT finger pairs. Typical operating frequencies range from 30 MHz to several GHz.

From a signal processing point of view, SAW filters can be viewed as Finite Impulse Response (FIR) transversal filters, whose tap weights correspond to the IDT finger overlaps and the delays to the finger spacings. Utilizing FIR filter design methods, frequency responses can be designed by the geometry of the finger locations and overlaps.

For high frequency applications, either the increase of v or the decrease of λ is necessary from eq.(1.5). The minimum value of λ is limited by the lithographic resolution of the fabrication tools. An increase of v can be achieved with the use of new materials or leaky SAW waves.

In order for SAW filters to be effective, the electro-mechanical coupling must be strong. In SAW filters, the minimum insertion loss and the maximum bandwidth are closely related to this coupling coefficient.

The temperature coefficient of the substrate material is also important, especially for the narrow band applications such as resonators.

1.3 Diamond SAW Filters

The recent rapid development of high-speed communication systems has increased the demand for low-loss surface acoustic wave (SAW) filters with high operating frequencies.

Diamond substrates are promising candidates for this type of application because of their high phase velocity. However, Diamond is an covalent crystal without inversion symmetry, which leads to a lack of piezoelectricity. Therefore, it must be used in a composite layered substrate with a piezoelectric material for the excitation and the detection of the SAW. Several piezoelectric materials, such as ZnO [6], $LiNbO_3$, $LiTaO_3$ [7] and so on, have been investigated over the years. The typical Diamond SAW filter based on the ZnO/Diamond substrate is shown in fig. 1.5. After the Diamond thin film is synthesized on the substrate, the ZnO thin film is formed on the top of the Diamond. The metal IDT's can be either on the top of the ZnO or between the ZnO/Diamond interface.

These piezoelectric materials are deposited on the Diamond by RF magnetron sputtering or ECR (Electron Cyclotron Resonance) sputtering. Because Diamond is not in a stable state under high temperature with oxygen, the deposition conditions are critical. Due to this fact, only ZnO is practical at this moment as a compatible piezoelectric layer.

A single crystalline Diamond wafer is unfortunately not available yet. In

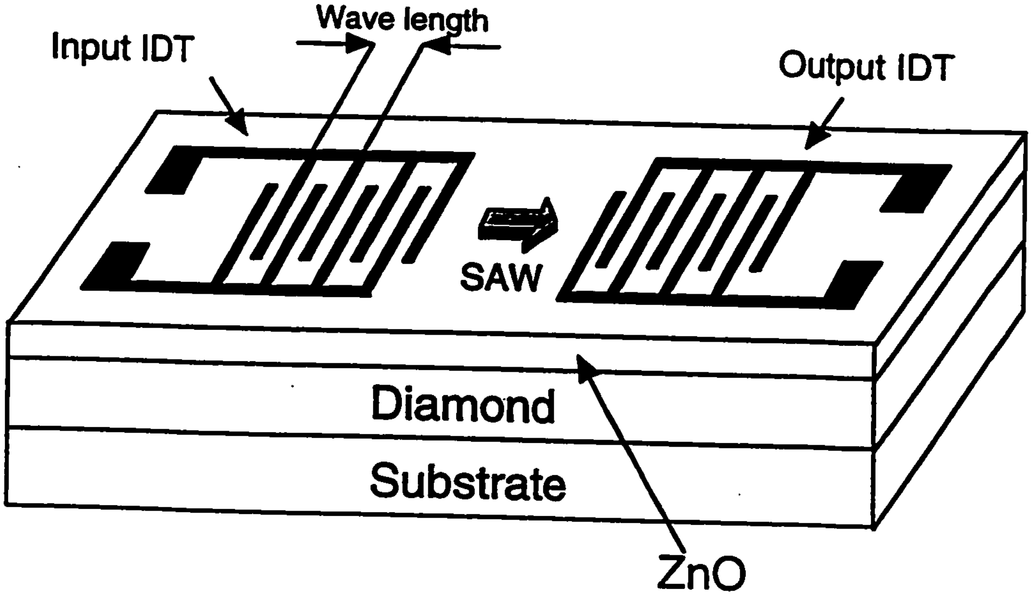

Figure 1.5: The typical Diamond SAW filter based on the ZnO/Diamond substrate.

practice, only polycrystalline Diamond thin films grown on a silicon substrate by chemical vapor deposition (CVD) are commercially available. Diamond SAW filters have been reported to have a high power durability [8]. SiO_2/ZnO/Diamond multi-layered substrate also have good temperature stability, and find applications in narrow band filters for optical fiber communications [9] [10].

As was stated before, the multi-layered nature of the Diamond SAW substrates causes multiple dispersive propagation modes. These higher modes are known as Sezawa waves. The wave propagation properties are different for each Sezawa wave. The properties will be discussed later in this Thesis.

1.4 SAW Filter Design

For SAW filter design, the coupling-of-modes (COM) and the equivalent circuit design methods are commonly used. The equivalent circuit model (ECM), first proposed by W. R. Smith [11], expresses the IDT structure as an equivalent electrical circuit. The frequency response is calculated from the admittance of this equivalent circuit.

As will be shown in Chap.2 (p.22), the COM model is an efficient and powerful design tool. However, it is a phenomenological one that, like the equivalent circuit model, requires parameters that are usually determined experimentally.

In order to meet the stringent demands of modern communication systems, accurate modeling tools that can predict the propagation characteristics under the metal electrodes are necessary. Two effects due to the existence of the electrodes affect the response of the device. One is the electrical shortening effect and the other is the mass loading effect. Due to the complexity of the problem, only the electrical effects are usually considered, which leads to a good approximation for low frequency filter designs. However, as the operating frequency gets higher and λ gets smaller, the relative thickness of the electrode becomes larger. In this case, we can't neglect the mechanical effects.

Several rigorous analysis techniques have been developed for considering both electrical and mechanical effects, including the dyadic Green's function method [12] [13], the finite element method (FEM) [14] [15] and the space harmonic method (SHM) [16].

For the Green's function method, the entire response of the system is described by the Green's function, which corresponds to the response to a delta function source on the surface. Therefore, if we know the charge and stress distribution on the surface, we can rigorously predict the entire behaviour. When R. F. Milson *et al.* [17] first used Green's function analysis, only the electrical effect was taken into account for the simplification of the problem. In mid-1990's, several authors extended this method to the dyadic Green's function method, which not only includes electric effects but also mechanical effects [18] [19] [12]. Recently, the Green's function for multi-layered substrates has been derived [20]. Green's functions alone do not, however, provide the propagation properties under grating structures, because the direct calculation for hundreds of electrodes is not realizable. Some hybrid methods, such as the FEM and the periodic Green's function [21] [22], offer this information under the infinite grating structure approximation. FEM has the drawback that it is time consuming, especially for multi-layered substrates.

For the propagation analysis under an infinite grating structure, the space harmonic method (SHM) can also be used. As will be explained in Chap.3 (p. 46), this method uses a set of space harmonics as a complete set of basis functions.

This method was originally applied to the propagation analysis of leaky SAW by Q. Xue and Y. Shui in 1990 [23]. At that time, mechanical effects were neglected for the simplicity of the problem. Since then, V. M. Bright and W. D. Hunt, and Meier et al. applied the method to the case of thin metal electrodes using a first order approximation of the stress caused by the electrodes in 1991 [24] and 1992 [25], respectively.

The extension of this method with the introduction of the boundary condition integral by T. Sato and H. Abe in 1998 [16] enabled the SHM to take fully into account the mechanical effects with arbitrary shapes of electrodes.

We became aware of the potential of this method to extend to the analysis of multi-layered structures and started our research about the wave propagation analysis under an infinite grating structure on ZnO/Diamond structures in 1998. In parallel, Sato *et al.* applied the method to $SiO_2/Al/Li_2B_4O_7$ multi-layered substrates and published a paper in 1999 [26]. Our ZnO/Diamond substrate is, however, particularly interesting because, unlike the $SiO_2/Al/Li_2B_4O_7$ substrate, the piezoelectric wave excitation layer and the high velocity layer are distinct. The wave propagating properties can therefore be expected to be different from [26].

1.5 Motivation of This Study

Multi-layered substrates for surface acoustic wave (SAW) filters have received considerable attention, because they offer a possibility of meeting specifications for temperature stability, high center frequency, and high electro-mechanical coupling, simultaneously.

The specifications of modern communication systems such as wireless mobile communication systems, requires SAW filters with very stringent frequency responses. The two major SAW filter design methods (ECM and COM) both need device parameters, which correspond to the wave reflection and the electro-mechanical coupling at the electrodes. In order to satisfy stringent specifications, the accuracy of these parameters becomes critical. In the past, these parameters have usually been determined experimentally using test structures. Especially for multi-layered substrates, however, these costly and time-consuming experiments have to be repeated for all sets of film thicknesses. Therefore, it is necessary to develop a theoretical method which can handle multi-layered substrates and predict parameters with high precision, and this is the most significant goal of this Thesis.

In this Thesis, the space harmonic method (SHM) is extended to account for multi-layered structures in order to analyse SAW propagation properties under an infinite grating structure. The SHM is rigorous enough to consider both electrical and mechanical effects due to the existence of grating metals. SHM is also modified to account for SAW generation by an applied voltage. In ZnO/Diamond substrates, the piezoelectric wave excitation and the high velocity layers are expected to be distinct. Therefore, it is important to know the properties such as energy profile inside each layer.

By use of this theoretical analysis, the dispersion curves can be derived for each set of film thicknesses, from which the COM parameters can be theoretically determined. From the calculated admittance curves of substrates, the SAW generation behaviour will be examined. The physical behavior of the multi-layered material, such as the displacement and the energy distributions, can be examined. The data that we generate is sufficient for the full characterization and design of SAW filters with COM theory. These will form the kernel of this study.

1.6 Scope of the Thesis

The purpose of this Thesis is to develop rigorous analytical models to describe the acoustic wave excitation and propagation under multi-layered structures. The treatment presented in this Thesis links the physical models of acoustic propagation in multi-layer piezoelectric substrates to the phonomenological COM models that are commonly used in device design. The results lead to the ability to determine COM parameters without the need to build prototype devices. This ability is critical to the economical future development of devices based on multi-layer substrates.

The specific contributions of this work are the following:

1. Based on the space harmonic analysis used for single layer SAW substrates, we independently develop a rigorous analytical method for the evaluation of SAW propagation of multi-layered structures. In this analysis, both electrical and mechanical effects can be considered for arbitrary thickness and shape of grating electrodes. We apply this extended method to Al/ZnO/Diamond structures, where the wave exciting layer and the high velocity layer are distinct. From the calculated dispersion curves, SAW filter design parameters are derived as a function of film thicknesses. The most significant contribution of this development is that it provides SAW filter designers with all but one of the accurate COM device parameters directly (the static capacitance is obtained later) for a potentially infinite set of multi-layer thickness conditions, without the need for costly and time-consuming parameter extraction from experimental prototype devices. This analysis also gives us a new freedom to control multiple SAW device properties by including the layer thicknesses as a design parameter, which is not currently available. A discrepansy between the centers of reflection and transduction is predicted for the first time on structurally symmetric ZnO/Diamond substrates, which may enable the development of totally

new filter configrations. For the second Sezawa wave, we show that the self coupling coefficient increases and the mutual coupling coefficient (the reflection coefficient) decreases linearly as a function of Al grating thickness for ZnO thicknesses of $H_{ZnO} = P/\pi$ and $H_{ZnO} = 1.5P/\pi$, where P is a period of the grating structure. The transduction coefficient, which corresponds to electromechanical coupling, is almost insensitive to the grating thickness. For the first Sezawa wave of the ZnO thicknesses of $H_{ZnO} = 1.75P/\pi$, the mutual coupling coefficient becomes a pure imaginary value when the Al thicknesses is greater than $H_{Al} = 0.008P$. These parameters can be used for the precise design of SAW filters.

2. We examine the physical SAW propagation behaviour of multi-layered substrates. The displacement and the energy distributions inside ZnO/Diamond multi-layered substrates are presented for the first time. This information gives us a better understanding of what is happening inside multi-layered structures of this type, and it gives a further insight into device performance. It is also useful, for example, in studying power-handling ability of ZnO/Diamond substrates, which may form the basis for future high power-handling SAW filters such as front end RF filters for wireless satellite communications. For a ZnO thickness of $H_{ZnO} = P/\pi$, the total amount of energy inside the Diamond is of the same order as that inside the ZnO layer. At the ZnO/Diamond interface, the kinetic energy inside the Diamond is larger than the strain energy at the

electrode midpoint, while the strain energy is larger at the center of the spacing between electrodes.

3. We extend the SHM for the first time to handle the wave excitation problem in a multi-layered substrate by an applied voltage. Admittance curves are obtained which correspond to the SAW excitation and which provide the static capacitance of transducers built on multi-layered substrates, thereby theoretically providing the last remaining parameter needed for device design. The static capacitance for Al/ZnO/Diamond structures is shown to increase as the ZnO thickness increases.

This Thesis is organized into four chapters. Chapter 2 deals with the COM theory and the theoretical derivation of the COM parameters. Chapter 3 discusses the space harmonic method for multi-layered diamond SAW substrates. From the calculated results, the COM parameters for Al/ZnO/Diamond substrate are derived, and energy profiles computed. Finally, Chapter 4 will conclude the Thesis.

Chapter 2

Coupling-of-Modes Theory

2.1 Introduction

The coupling-of-modes (COM) theory is one of the most prevailing SAW filter design methods. It describes forward and backward propagating waves with slowly varying amplitudes represented by coupled differential equations. The COM model is, however, a phenomenological one. The analysis depends on only a few parameters, corresponding to the SAW velocity change, reflection, transduction and attenuation, as well as the static capacitance per electrode pair. These parameters can be obtained from rather time consuming and expensive experimental measurements, without considering the complexities of the underlying physics.

This method had its origin in microwave work in the 1950's [27] and found wide application in thick optical holograms [28], optical waveguides [29] and so on.

The first use of this method in the SAW field was a paper on gratings by Y. Suzuki *et al.* [30]. Later, Y. Koyamada and S. Yoshikawa [31] extended the method to include necessary transduction terms for SAW transducers.

From the late 1980's to the early 1990's, the rigorous numerical calculations for these COM parameters were done with FEM [32] [33], assuming that these parameters did not vary much with frequency. This assumption is valid for the Rayleigh wave.

In this chapter, the COM theory will be reviewed. The general COM equations with finite loss will be derived in detail based on [33] and [34]. The relation between two sets of COM equations is clarified. For the low loss approximation, the COM equations are simplified to require only five COM parameters, that is, the self coupling coefficient κ_{11}, the mutual coupling coefficient κ_{12}, the transduction coefficient ζ and the propagation loss α_L, as well as the static capacitance of one grating pair C_P.

The dispersion diagram is expressed by using COM. We show that the four required parameters except for C_P can be evaluated from the dispersion diagram. We then derive the admittance curve using the COM equations.

2.2 COM Description

In SAW devices, metal gratings are used for exciting and detecting the SAW. The discontinuities produced by these gratings cause reflection of the waves.

Consider the periodic grating structures shown in fig. 2.1. The period of the grating is Λ. We define the forward travelling wave as a_1 and the backward travelling wave as a_2.

$$a_1 \propto e^{-j(k_R - j\alpha_L)x} \tag{2.1}$$

$$a_2 \propto e^{j(k_R - j\alpha_L)x} \tag{2.2}$$

where k_R is the wavenumber of the free surface wave without gratings and α_L is a propagation loss.

If there are no perturbations, the two waves are independent and can be described by

$$\frac{da_1}{dx} = -j(k_R - j\alpha_L)a_1 \tag{2.3}$$

$$\frac{da_2}{dx} = j(k_R - j\alpha_L)a_2 \tag{2.4}$$

When subjected to reflections due to the gratings, the two waves affect each other. The wavenumber of the free surface wave also changes by Δk due to the SAW velocity change.

$$\frac{da_1}{dx} = -j(k - j\alpha_L)a_1 + j\kappa_{21}a_2 \exp\left(-j\frac{2\pi}{\Lambda}x\right) \tag{2.5}$$

$$\frac{da_2}{dx} = j(k - j\alpha_L)a_2 + j\kappa_{12}a_1 \exp\left(j\frac{2\pi}{\Lambda}x\right) \tag{2.6}$$

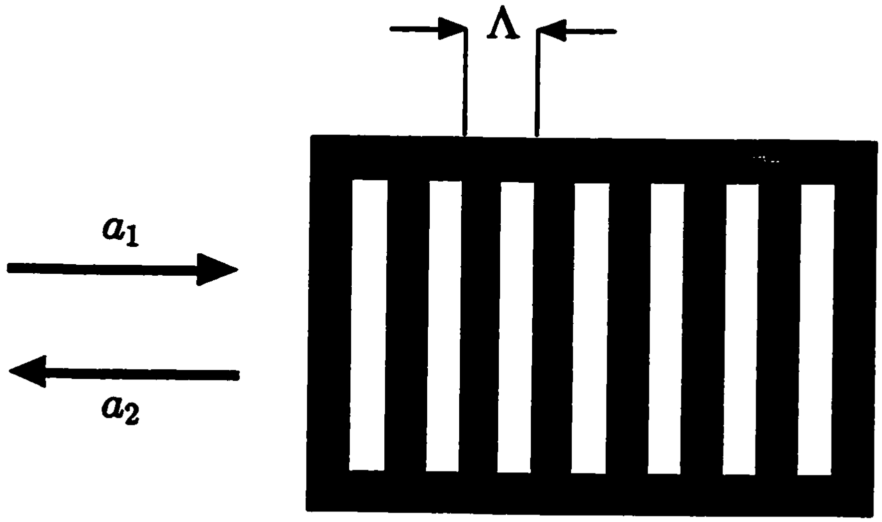

Figure 2.1: Grating structure with grating period Λ.

where

$$k = k_R + \Delta k \tag{2.7}$$

is a modified wavenumber of the surface waves.

Coupling coefficients, κ_{12} and κ_{21}, are functions of x. They have the same period as the gratings and they can be re-written by using a Fourier expansion. From Fourier series,

$$\kappa_{21} = \sum_n \kappa_{21}(n) \exp(jk_g nx) \tag{2.8}$$

$$\kappa_{12} = \sum_n \kappa_{12}(n) \exp(jk_g nx) \tag{2.9}$$

where the Bragg wavenumber k_g is

$$k_g = \frac{2\pi}{\Lambda} \tag{2.10}$$

Now, new variables $A_1(x)$ and $A_2(x)$ are introduced.

$$a_1(x) = A_1(x) \exp\left(-j\frac{k_g}{2}x\right) \tag{2.11}$$

$$a_2(x) = A_2(x) \exp\left(j\frac{k_g}{2}x\right) \tag{2.12}$$

where $A_1(x)$ and $A_2(x)$ are the slowly varying complex amplitudes of the travelling waves in the positive and the negative directions, respectively.

Substitution of (2.11) and (2.12) into (2.5) and (2.6) yields,

$$\frac{dA_1(x)}{dx} = -j\left(k - j\alpha_L - \frac{k_g}{2}\right) A_1(x) + j\sum_n \kappa_{21}(n) A_2(x) \exp\{j(n+1)k_g x\} \tag{2.13}$$

$$\frac{dA_2(x)}{dx} = j\left(k - j\alpha_L - \frac{k_g}{2}\right)A_2(x) + j\sum_n \kappa_{12}(n)A_1(x)\exp\{-j(n+1)k_g x\} \tag{2.14}$$

If we only keep the $n = -1$ term in the summation, then the coupling coefficients become independent of x.

$$\frac{dA_1(x)}{dx} = -j\delta_D A_1(x) + j\kappa_{21D}A_2(x) \tag{2.15}$$

$$\frac{dA_2(x)}{dx} = j\delta_D A_2(x) + j\kappa_{12D}A_2(x) \tag{2.16}$$

where

$$\delta_D \equiv k_R + \Delta k - j\alpha_L - \frac{k_g}{2} \tag{2.17}$$

$$\kappa_{21D} \equiv \kappa_{21}(-1) \tag{2.18}$$

$$\kappa_{12D} \equiv \kappa_{12}(-1) \tag{2.19}$$

We now generalize these equations to include the action of a voltage applied to the gratings by a pair of electrodes. If the excitation of surface acoustic waves per strip is small, the effect of the voltage V can be incorporated with eqs.(2.15) and (2.16) by terms proportional to V as

$$\frac{dA_1(x)}{dx} = -j\delta_D A_1(x) + j\kappa_{21D}A_2(x) + j\alpha V \tag{2.20}$$

$$\frac{dA_2(x)}{dx} = j\delta_D A_2(x) + j\kappa_{12D}A_1(x) + j\beta V \tag{2.21}$$

If the currents are small,

$$\frac{dI(x)}{dx} = j\zeta A_1(x) + j\eta A_2(x) + j\omega C V \tag{2.22}$$

where C is the static capacitance per unit length.

Eqs.(2.20)-(2.22) are the most general expressions for the COM equations.

2.3 Low Loss Approximation

For the case where loss is negligible, the above three COM equations (2.20)-(2.22) can be reduced to simpler forms. From power conservation for the shorted gratings case ($V = 0$),

$$\frac{d}{dx}(|a_1|^2 - |a_2|^2) = 0 \tag{2.23}$$

Using the relations, $|a_1|^2 = a_1^* \cdot a_1$ and $|a_2|^2 = a_2^* \cdot a_2$, and the expressions (2.5) and (2.6), (2.23) leads to

$$\alpha(|a_1|^2 + |a_2|^2) = Re\left[a_1^* a_2 e^{-j\left(\frac{2\pi}{\Lambda}x\right)}(\kappa_{21D} + \kappa_{12D}^*)\right] \tag{2.24}$$

For the lossless case, $\alpha = 0$. Then, the following relation must hold.

$$\kappa_{21D} = -\kappa_{12D}^* \equiv \kappa_D \tag{2.25}$$

That is, two coupling coefficients are complex conjugates of each other except for the sign change.

Next, we will derive the relation between α, β, ζ and η. From power conservation,

$$\frac{d}{dx}(|A_1|^2 - |A_2|^2) = \frac{1}{2}\left(V\frac{dI^*}{dx} + V^*\frac{dI}{dx}\right) \tag{2.26}$$

The left hand side of eq.(2.26) becomes,

$$\begin{aligned}\frac{d}{dx}(|A_1|^2 - |A_2|^2) &= j(\delta_D^* - \delta_D)(|A_1|^2 - |A_2|^2) - jV^*(\alpha^* A_1 - \beta^* A_2) \\ &\quad +jV(\alpha A_1^* - \beta A_2^*) \\ &= -jV^*\alpha^* A_1 + jV^*\beta^* A_2 + jV\alpha A_1^* - jV\beta A_2^* \qquad (2.27)\end{aligned}$$

We use the assumption that δ_D is a real value for the above derivation. This assumption is true only for the lossless case.

The right hand side of eq.(2.26) becomes,

$$\frac{1}{2}\left(V\frac{dI^*}{dx} + V^*\frac{dI}{dx}\right) = \frac{1}{2}(-j\zeta^* V A_1^* - j\eta^* V A_2^* + j\zeta V^* A_1 + j\eta V^* A_2) \qquad (2.28)$$

Therefore, from eq.(2.26),

$$(2\alpha + \zeta^*)A_1^* V - \{(2\alpha + \zeta^*)A_1^* V\}^* - (2\beta - \eta^*)A_2^* V + \{(2\beta - \eta^*)A_2^* V\}^* = 0 \qquad (2.29)$$

Eq.(2.29) must hold for arbitrary A_1, A_2 and V. This results in,

$$\zeta^* = -2\alpha \qquad (2.30)$$

$$\eta^* = 2\beta \qquad (2.31)$$

Also for the lossless case, the complex conjugates of A_1 and A_2 correspond to time-reversals and this gives us the following relation between α and β.

$$\alpha = -\beta^* \qquad (2.32)$$

In summary, we can use the following COM equations for a low loss approximation,

$$\frac{dA_1(x)}{dx} = -j\delta_D A_1(x) + j\kappa_D A_2(x) + j\alpha V \tag{2.33}$$

$$\frac{dA_2(x)}{dx} = j\delta_D A_2(x) - j\kappa_D^* A_1(x) - j\alpha^* V \tag{2.34}$$

$$\frac{dI(x)}{dx} = -j2\alpha^* A_1(x) - j2\alpha A_2(x) + j\omega C V \tag{2.35}$$

where

$$\delta_D = k_R + \Delta k - j\alpha_L - \frac{k_g}{2} \tag{2.36}$$

The above equations, introduced by D. P. Chen and H. A. Haus [34], implicitly contain an unknown parameter Δk. It is preferable for this unknown parameter to be expressed explicitly. We can do this by expressing the COM equations in terms of the new variables $A^+(x)$ and $A^-(x)$

$$a_1(x) = A^+(x)e^{-jk_R x} \tag{2.37}$$

$$a_2(x) = A^-(x)e^{jk_R x} \tag{2.38}$$

$A^+(x)$ and $A^-(x)$ are slowly varying complex amplitudes from waves without any surface perturbations.

The resultant COM equations for the low loss approximation are [33]

$$\frac{dA^+(x)}{dx} = -j\kappa_{11} A^+(x) - j\kappa_{12} e^{j2\delta x} A^-(x) + j\zeta e^{j\delta x} V \tag{2.39}$$

$$\frac{dA^-(x)}{dx} = j\kappa_{12}^* e^{-j2\delta x} A^+(x) + j\kappa_{11} A^-(x) - j\zeta^* e^{-j\delta x} V \tag{2.40}$$

$$\frac{dI(x)}{dx} = -j2\zeta^* e^{-j\delta x} A^+(x) - j2\zeta e^{j\delta x} A^-(x) + j\omega C V \tag{2.41}$$

where

$$\delta = k_R - j\alpha_L - \frac{k_g}{2} = \frac{2\pi}{\lambda_0}\left(\frac{\lambda_0}{\lambda} - 1\right) - j\alpha_L = \frac{2\pi}{\lambda_0}\left(\frac{f}{f_0} - 1\right) - j\alpha_L \tag{2.42}$$

The last transformation of (2.42) ignores the minor velocity dispersion which may be present over the finite frequency bandwidth of the interaction.

In the above transformation, we use the following variable transformations.

$$\begin{aligned} \Delta k &\longrightarrow \kappa_{11} \\ \kappa_D &\longrightarrow -\kappa_{12} \\ \alpha &\longrightarrow \zeta \end{aligned}$$

δ is called the detuning parameter. κ_{11} and κ_{12} are the self coupling coefficient and the mutual coupling coefficient, respectively. ζ is the transduction coefficient.

2.4 Dispersion Analysis using COM Theory

2.4.1 Dispersion Relation

For the shorted gratings case ($V = 0$), (2.33) and (2.34) form a homogeneous system of linear first-order equations.

$$\begin{bmatrix} \frac{dA_1(x)}{dx} \\ \frac{dA_2(x)}{dx} \end{bmatrix} = \begin{bmatrix} -j\delta_D & j\kappa_D \\ -j\kappa_D^* & j\delta_D \end{bmatrix} \begin{bmatrix} A_1(x) \\ A_2(x) \end{bmatrix} \tag{2.43}$$

Using

$$\mathbf{X}(x) = \begin{bmatrix} A_1(x) \\ A_2(x) \end{bmatrix} \tag{2.44}$$

$$\mathbf{A}(x) = \begin{bmatrix} -j\delta_D & j\kappa_D \\ -j\kappa_D^* & j\delta_D \end{bmatrix} \tag{2.45}$$

(2.43) can be written as

$$\dot{\mathbf{X}} = \mathbf{A}\mathbf{X} \tag{2.46}$$

Now, we assume that the solution has the following form

$$\mathbf{X} = \xi e^{j\Delta x} \tag{2.47}$$

where ξ is the 2-by-1 coefficient vector and Δ is a number and a function of frequency. Substituting (2.47) into (2.46), we get the following equation

$$\mathbf{A}\xi = j\Delta\xi \tag{2.48}$$

In order for the above equation to hold, $det(\mathbf{A} - j\Delta\mathbf{I}) = 0$, where $\mathbf{I}$ is 2-by-2 identity matrix. We obtain the following two acceptable values for Δ.

$$\begin{aligned} \Delta(f) &= \pm\sqrt{\delta_D^2 - |\kappa_D|^2} \\ &= \pm\sqrt{(\delta + \kappa_{11})^2 - |\kappa_{12}|^2} \end{aligned} \tag{2.49}$$

These wavenumbers describe the dispersion properties for shorted gratings. The dispersion diagram for the lossless case is shown in fig. 2.2. We see that for $|\delta+\kappa_{11}| < |\kappa_{12}|$, Δ is pure imaginary and the amplitude of the waves along the grating will decrease exponentially. The frequency region where the above inequality holds is called the stopband. Inside the stopband, the waves satisfy the Bragg's condition and the multiple reflections form a standing wave. The center of the stopband, f_c, is given as

$$f_c = f_0 \left(1 - \frac{\lambda_0}{2\pi}\kappa_{11}\right) \tag{2.50}$$

f_c is modified from f_0 due to the existence of the gratings and the difference is proportional to κ_{11}. The stopband width is related to $|\kappa_{12}|$, as will be explained next.

2.4.2 Derivation of Coupling Coefficients

At the stopband edge for shorted gratings, $\Delta = 0$. Then, from eq.(2.49),

$$|\kappa_{12}|^2 - (\delta + \kappa_{11})^2 = 0$$

$$|\kappa_{12}|^2 - \left\{\frac{2\pi}{\lambda_0}\left(\frac{f}{f_0} - 1\right) + \kappa_{11}\right\}^2 = 0$$

$$\frac{f}{f_0} = \left(1 - \frac{\lambda_0}{2\pi}\kappa_{11}\right) \pm \frac{\lambda_0}{2\pi}|\kappa_{12}| \tag{2.51}$$

Eq.(2.51) holds for the upper stopband edge (f_{us}) and the lower stopband edge (f_{ls}), that is,

$$\frac{f_{us}}{f_0} = \left(1 - \frac{\lambda_0}{2\pi}\kappa_{11}\right) + \frac{\lambda_0}{2\pi}|\kappa_{12}| \tag{2.52}$$

$$\frac{f_{ls}}{f_0} = \left(1 - \frac{\lambda_0}{2\pi}\kappa_{11}\right) - \frac{\lambda_0}{2\pi}|\kappa_{12}| \tag{2.53}$$

Subtracting both sides of (2.52) and (2.53),

$$|\kappa_{12}\lambda_0| = \pi\frac{f_{us} - f_{ls}}{f_0} \tag{2.54}$$

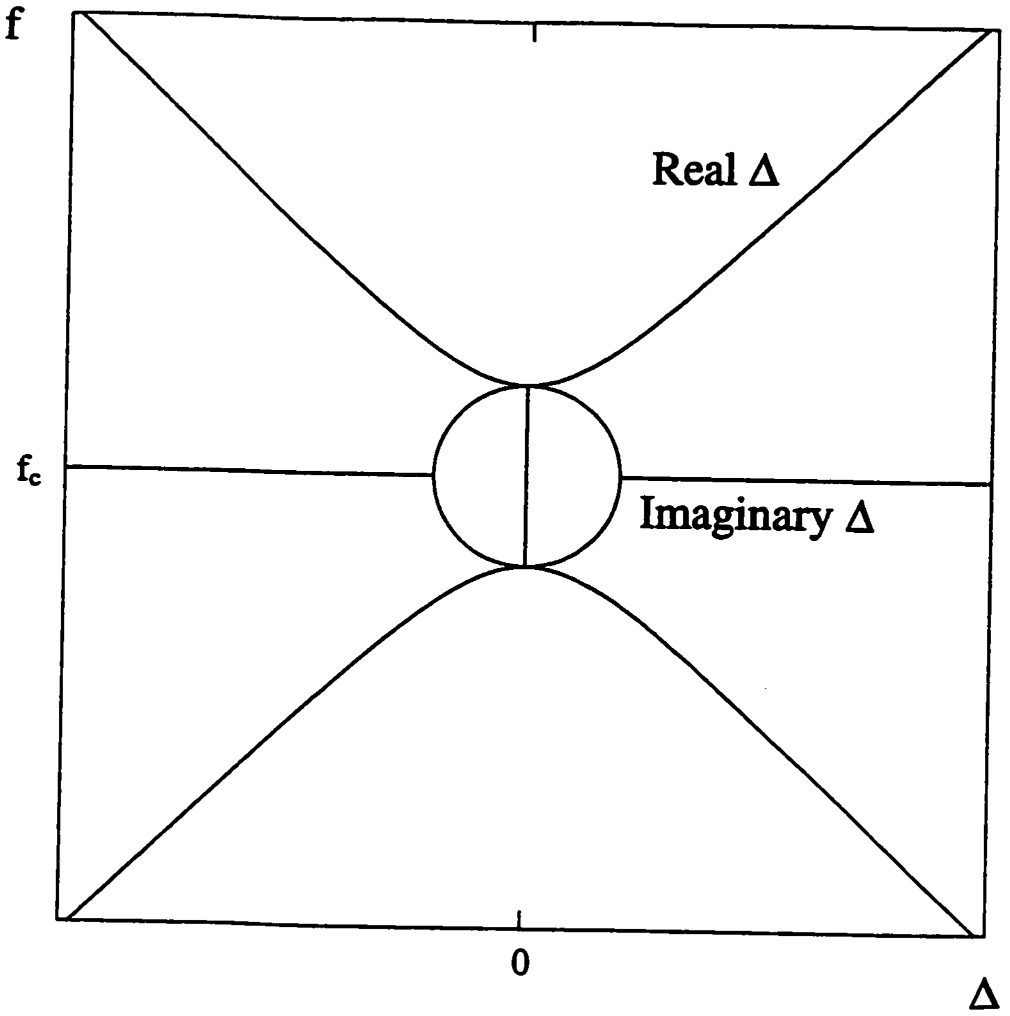

Figure 2.2: The dispersion diagram for shorted gratings without the propagation loss.

Substitution of (2.54) into (2.52) yields,

$$\kappa_{11}\lambda_0 = 2\pi\left(1 - \frac{f_{us} + f_{ls}}{2f_0}\right) \tag{2.55}$$

In summary, the magnitude of the mutual coupling coefficient and the self coupling coefficient can be derived from the information of the stopband frequencies for shorted gratings [33].

Next, we will get the information about the phase of the mutual coupling coefficient κ_{12}. Before doing so, we first introduce the notation of the standing wave patterns [35].

At the stopband edge for shorted gratings, $a_1 \propto e^{-j\frac{k_g}{2}x}$ and $a_2 \propto e^{j\frac{k_g}{2}x}$. Therefore, from eqs.(2.37) and (2.38),

$$\begin{aligned} A^+(x) &= A_{0+}e^{j\left(k_R-\frac{k_g}{2}\right)x} && (2.56)\\ A^-(x) &= A_{0-}e^{-j\left(k_R-\frac{k_g}{2}\right)x} && (2.57)\end{aligned}$$

where we assume that the loss is negligible.

We substitute these equations into (2.39) and (2.40) with $V = 0$,

$$\begin{pmatrix} \left(k_R - \frac{k_g}{2} + \kappa_{11}\right)e^{j\left(k_R-\frac{k_g}{2}\right)x} & \kappa_{12}e^{j2\delta x}e^{-j\left(k_R-\frac{k_g}{2}\right)x} \\ \kappa_{12}^{*}e^{-j2\delta x}e^{j\left(k_R-\frac{k_g}{2}\right)x} & \left(k_R - \frac{k_g}{2} + \kappa_{11}\right)e^{-j\left(k_R-\frac{k_g}{2}\right)x} \end{pmatrix} \begin{pmatrix} A_{0+} \\ A_{0-} \end{pmatrix} = \begin{pmatrix} 0 \\ 0 \end{pmatrix} \tag{2.58}$$

In order to satisfy the above vector equation, the following relation must hold

$$k_R - \frac{k_g}{2} + \kappa_{11} = \pm|\kappa_{12}| \tag{2.59}$$

where the + sign applies to the upper edge and the − sign to the lower edge of the stopband.

Therefore,

$$A_{0-} = \mp \frac{|\kappa_{12}|}{\kappa_{12}} A_{0+} \tag{2.60}$$

where the − sign applies to the upper edge and the + sign to the lower edge.

The above relations show that, at the stopband edge, the standing wave function, Ψ, corresponding to the surface electric potential, is given by,

$$\begin{aligned} \Psi &= a_1(x) + a_2(x) \\ &= A_{0+}\left(e^{-j\frac{k_g}{2}x} \mp \frac{|\kappa_{12}|}{\kappa_{12}} e^{j\frac{k_g}{2}x}\right) \end{aligned} \tag{2.61}$$

where the − sign applies to the upper edge and the + sign to the lower edge.

If we define,

$$\kappa_{12} = |\kappa_{12}| e^{j2\phi} \tag{2.62}$$

then,

$$\begin{aligned} \Psi &= A_{0+}e^{-j\phi}\left\{e^{-j\left(\frac{k_g}{2}x-\phi\right)} \mp e^{j\left(\frac{k_g}{2}x-\phi\right)}\right\} \\ &= \begin{cases} A_{0+}e^{-j\phi}2\cos\left(\frac{k_g}{2}x - \phi\right) & \text{(for lower edge)} \\ A_{0+}e^{-j\phi}(-2j)\sin\left(\frac{k_g}{2}x - \phi\right) & \text{(for upper edge)} \end{cases} \end{aligned} \tag{2.63}$$

where $x = 0$ corresponds to the center of the grating. From the relation (2.63), we see that the standing waves are 90° phase shifted between the upper edge and the lower edge.

If the potential has a maximum value at the center of the grating for lower edge, $\phi = 0$, then $\kappa_{12} = |\kappa_{12}|$. On the other hand, if it is minimum at the center for lower edge, $\phi = \pi/2$, then $\kappa_{12} = -|\kappa_{12}|$. This means that knowledge of the potential distribution at stopband edges for shorted gratings enables us to determine the phase of the mutual coupling coefficient.

2.4.3 Derivation of Transduction Coefficient

Next, we consider the open grating case, where

$$\frac{dI}{dx} = 0$$

From eq.(2.41),

$$V = \frac{2}{\omega C}\left\{\zeta^* e^{-j\delta x} A^+(x) + \zeta e^{j\delta x} A^-(x)\right\} \tag{2.64}$$

Assuming the form (2.47) and substituting (2.64) into (2.39) and (2.40), we finally get

$$\begin{pmatrix} \lambda - k_R + \frac{k_g}{2} - \kappa_{11} + \frac{2}{\omega C}|\zeta|^2 & \left(\frac{2}{\omega C}\zeta^2 - \kappa_{12}\right) e^{j2\delta x} \\ -\left(\frac{2}{\omega C}(\zeta^*)^2 - \kappa_{12}^*\right) e^{-j2\delta x} & \lambda + k_R - \frac{k_g}{2} + \kappa_{11} - \frac{2}{\omega C}|\zeta|^2 \end{pmatrix} \begin{pmatrix} A_1 \\ A_2 \end{pmatrix} = \begin{pmatrix} 0 \\ 0 \end{pmatrix} \tag{2.65}$$

In order for (2.65) to have non trivial solutions,

$$\begin{aligned} \lambda^2 \;=\; & \left(\delta + \kappa_{11} - \frac{2}{\omega C}|\zeta|^2\right)^2 - |\kappa_{12}|^2 - \left(\frac{2}{\omega C}|\zeta|^2\right)^2 \\ & + \frac{2}{\omega C}((\zeta^*)^2\kappa_{12} + \zeta^2\kappa_{12}^*) \end{aligned} \tag{2.66}$$

Using the expressions,

$$\begin{aligned}\kappa_{12} &= |\kappa_{12}|e^{j2\phi}\\ \zeta &= |\zeta|e^{j\psi}\end{aligned}$$

$$\begin{aligned}\lambda^2 &= -|\kappa_{12}|^2 + 2|\kappa_{12}|\frac{2|\zeta|^2}{\omega C}\cos\{2(\phi-\psi)\} - \left(\frac{2}{\omega C}|\zeta|^2\right)^2\\ &\quad + \left(\delta + \kappa_{11} - \frac{2}{\omega C}|\zeta|^2\right)^2 \qquad (2.67)\end{aligned}$$

At the stopband edge ($\lambda = 0$),

$$\cos\{2(\phi-\psi)\} = \frac{\omega C}{4|\kappa_{12}||\zeta|^2}\left\{|\kappa_{12}|^2 - (\delta+\kappa_{11})^2 + \frac{4|\zeta|^2}{\omega C}(\delta+\kappa_{11})\right\} \qquad (2.68)$$

Eq.(2.68) holds for the upper and the lower stopband edges, which leads to two equations for the upper edge (f_{uo}) and the lower edge (f_{lo}). From these two equations, the left hand side of eq.(2.68) is eliminated by assuming that $\phi - \psi$ is identical at both $f = f_{uo}$ and $f = f_{lo}$. After some manipulations, we get the following equation for the transduction coefficient, ζ and the phase difference, $|\phi - \psi|$

$$\frac{|\zeta\lambda_0|^2}{\omega_0 C_P} = \frac{\pi}{2}\frac{1}{f_0^2}\{(f_{uo}^2 + f_{lo}^2 + f_{uo}f_{lo} + f_{us}f_{ls}) - (f_{us}+f_{ls})(f_{uo}+f_{lo})\} \qquad (2.69)$$

$$\begin{aligned}|\phi-\psi| &= \frac{1}{2}\cos^{-1}\left[\frac{1}{(f_{us}-f_{ls})}\right.\\ &\left\{\frac{f_{uo}(2f_{lo}-f_{us}-f_{ls})(f_{uo}f_{us}+f_{uo}f_{ls}-f_{lo}^2-f_{us}f_{ls})}{f_{uo}(f_{uo}f_{us}+f_{uo}f_{ls}-f_{uo}^2-f_{us}f_{ls}) - f_{lo}(f_{lo}f_{us}+f_{lo}f_{ls}-f_{lo}^2-f_{us}f_{ls})}\right.\\ &\left.\left.-\frac{f_{lo}(2f_{uo}-f_{us}-f_{ls})(f_{lo}f_{us}+f_{lo}f_{ls}-f_{lo}^2-f_{us}f_{ls})}{f_{uo}(f_{uo}f_{us}+f_{uo}f_{ls}-f_{uo}^2-f_{us}f_{ls}) - f_{lo}(f_{lo}f_{us}+f_{lo}f_{ls}-f_{lo}^2-f_{us}f_{ls})}\right\}\right]\end{aligned}$$

(2.70)

where C_P is the static capacitance of one electrode pair.

As is clear from the above derivations, the transduction coefficient can be obtained from the dispersion diagram for open gratings [33]. The capacitance in the denominator of the left hand side of (2.69) can also be computed, as shown later in Chap.3 (p. 46).

From eq.(2.70), we can easily find the following relations

$$|\phi - \psi| = 0 \quad \text{when} \quad f_{lo} = f_{us} \text{ or } f_{uo} = f_{us} \tag{2.71}$$

$$|\phi - \psi| = \frac{\pi}{2} \quad \text{when} \quad f_{lo} = f_{ls} \text{ or} f_{uo} = f_{ls} \tag{2.72}$$

2.5 Admittance Curve using the COM Equations

If we apply an external voltage, the wave generation due to this voltage can be described by the particular solution of inhomogeneous differential equations, that is, the COM equations [39]. Here, we start from the most general COM equations (2.20)-(2.22).

Eqs.(2.20) and (2.21) form the following matrix equation

$$\dot{\mathbf{X}} = \mathbf{A}\mathbf{X} + \mathbf{f} \tag{2.73}$$

where

$$\mathbf{A} = \begin{bmatrix} -j\delta_D & j\kappa_{21D} \\ j\kappa_{12D} & j\delta_D \end{bmatrix} \tag{2.74}$$

$$\mathbf{f} = j \begin{bmatrix} \alpha \\ \beta \end{bmatrix} V \tag{2.75}$$

From the principle of the superposition, the solution of (2.73) can be given by the sum of the solutions of the following two differential equations.

$$\begin{aligned}\dot{\mathbf{X}}_1 &= \mathbf{A}\mathbf{X}_1 + \mathbf{f}_1 &\quad (2.76)\\ \dot{\mathbf{X}}_2 &= \mathbf{A}\mathbf{X}_2 + \mathbf{f}_2 &\quad (2.77)\end{aligned}$$

where

$$\begin{aligned}\mathbf{f}_1 &= \begin{bmatrix}1\\0\end{bmatrix} j\alpha V &\quad (2.78)\\ \mathbf{f}_2 &= \begin{bmatrix}0\\1\end{bmatrix} j\beta V &\quad (2.79)\end{aligned}$$

Now, we assume $\mathbf{X}_1 = \xi_1$. Then,

$$\mathbf{A}\xi_1 + \begin{bmatrix}1\\0\end{bmatrix} j\alpha V = 0 \quad (2.80)$$

Therefore,

$$\mathbf{X}_1 = \frac{\alpha V}{\delta_D^2 + \kappa_{21D}\cdot\kappa_{12D}}\begin{bmatrix}\delta\\-\kappa_{12D}\end{bmatrix} \quad (2.81)$$

Similarly, we assume $\mathbf{X}_2 = \xi_2$. Then, from (2.79),

$$\mathbf{X}_2 = \xi_2 = \frac{-\beta V}{\delta_D^2 + \kappa_{21D}\cdot\kappa_{12D}}\begin{bmatrix}\kappa_{21D}\\ \delta_D\end{bmatrix} \quad (2.82)$$

Therefore, the particular solution is given as

$$\begin{bmatrix}A_1\\A_2\end{bmatrix} = \frac{1}{\delta_D^2 + \kappa_{21D}\cdot\kappa_{12D}}\begin{bmatrix}(\alpha\delta_D - \beta\kappa_{21D})\\(-\alpha\kappa_{12D} - \beta\delta_D)\end{bmatrix} V \quad (2.83)$$

Substituting (2.83) into (2.22), we can get the expression for the current density, $j(x)$,

$$j(x) = \frac{dI}{dx}$$

$$= j\frac{(\zeta\alpha - \eta\beta)\delta_D - (\zeta\beta\kappa_{21D} + \eta\alpha\kappa_{12D})}{\delta_D^2 + \kappa_{21D} \cdot \kappa_{12D}}V + j\omega CV \tag{2.84}$$

The admittance for one period (λ_0) can be expressed by

$$Y(f) = j\lambda_0\frac{(\zeta\alpha - \eta\beta)\delta_D - (\zeta\beta\kappa_{21D} + \eta\alpha\kappa_{12D})}{\delta_D^2 + \kappa_{21D} \cdot \kappa_{12D}} + j\omega C_P \tag{2.85}$$

where $C_P = 2CP$ is the static capacitance of one electrode pair.

2.6 COM Parameter Derivation Using Admittance Curve

In the following derivation, we assume that the loss is very small and that relations (2.25), (2.30), (2.31) and (2.32) hold.

The current density (2.84) becomes,

$$j(x) = -4j\frac{\delta_D|\alpha|^2 + Re\{\kappa_D^*\alpha^2\}}{\delta_D^2 - |\kappa_D|^2}V + j\omega CV \tag{2.86}$$

Now, we use the further simplification that κ_D and α are real. Then,

$$j(x) = -j\frac{4\alpha^2}{\delta_D - \kappa_D}V + j\omega CV \tag{2.87}$$

The admittance for one period is, therefore,

$$Y(f) = -j\lambda_0\frac{4\alpha^2}{\delta_D - \kappa_D} + j\omega C_P \tag{2.88}$$

Using the another set of COM parameters,

$$Y(f) = -j\lambda_0\frac{4\zeta^2}{\delta + \kappa_{11} + \kappa_{12}} + j\omega C_P \tag{2.89}$$

where the detuning parameter is defined in (2.42)

$$\delta = \frac{2\pi}{\lambda_0}\left(\frac{f}{f_0} - 1\right) - j\alpha_L \tag{2.90}$$

$$\begin{aligned} Y(f) &= Y_r(f) + jY_i(f) \\ &= \frac{\lambda_0 4\zeta^2 \alpha_L}{\left\{\frac{2\pi}{\lambda_0}\left(\frac{f}{f_0} - 1\right) + \kappa_{11} + \kappa_{12}\right\}^2 + \alpha_L^2} \\ &\quad + j\left[\omega C_P - \frac{\lambda_0 4\alpha^2 \left\{\frac{2\pi}{\lambda_0}\left(\frac{f}{f_0} - 1\right) + \kappa_{11} + \kappa_{12}\right\}}{\left\{\frac{2\pi}{\lambda_0}\left(\frac{f}{f_0} - 1\right) + \kappa_{11} + \kappa_{12}\right\}^2 + \alpha_L^2}\right] \end{aligned} \tag{2.91}$$

where

$$Y_r(f) = \frac{\lambda_0 4\zeta^2 \alpha_L}{\left\{\frac{2\pi}{\lambda_0}\left(\frac{f}{f_0} - 1\right) + \kappa_{11} + \kappa_{12}\right\}^2 + \alpha_L^2} \tag{2.92}$$

and

$$Y_i(f) = \omega C_P - \frac{\lambda_0 4\zeta^2 \left\{\frac{2\pi}{\lambda_0}\left(\frac{f}{f_0} - 1\right) + \kappa_{11} + \kappa_{12}\right\}}{\left\{\frac{2\pi}{\lambda_0}\left(\frac{f}{f_0} - 1\right) + \kappa_{11} + \kappa_{12}\right\}^2 + \alpha_L^2} \tag{2.93}$$

The determination of the frequency (the resonant frequency) where the real part (2.92) reaches a maximum is straightforward:

$$f_r = f_0\left(1 - \frac{\kappa_{11}\lambda_0 + \kappa_{12}\lambda_0}{2\pi}\right) \tag{2.94}$$

The height of the resonant peak is

$$Y_{rm} = Y_r(f_r) = \frac{4(\zeta\lambda_0)^2}{(\alpha_L\lambda_0)} \tag{2.95}$$

and the full width of the peak at half maximum $Y_r = Y_{rm}/2$:

$$\Delta f = \frac{f_0}{\pi}(\alpha_L\lambda_0) \tag{2.96}$$

From the imaginary part of the admittance,

$$\frac{\partial Y_i}{\partial f} = \frac{4\zeta^2\lambda_0\left[\left\{\frac{2\pi}{\lambda_0}\left(\frac{f}{f_0}-1\right)+\kappa_{11}+\kappa_{12}\right\}^2-\alpha_L^2\right]}{\left[\left\{\frac{2\pi}{\lambda_0}\left(\frac{f}{f_0}-1\right)+\kappa_{11}+\kappa_{12}\right\}^2-\alpha_L^2\right]^2}\frac{2\pi}{\lambda_0 f_0} \tag{2.97}$$

Therefore, the peak frequencies for the imaginary part are

$$\begin{aligned} f_{ip-} &= f_0\left[1+\frac{\lambda_0}{2\pi}\{\alpha_L-(\kappa_{11}+\kappa_{12})\}\right] & (2.98)\\ f_{ip+} &= f_0\left[1-\frac{\lambda_0}{2\pi}\{\alpha_L+(\kappa_{11}+\kappa_{12})\}\right] & (2.99)\end{aligned}$$

The frequency difference between these two peaks, Δf_{ip}, is

$$\Delta f_{ip} = \frac{f_0}{\pi}(\alpha_L\lambda_0) \tag{2.100}$$

From eqs.(2.93, (2.98) and (2.99), the magnitude difference, ΔY_{im}, is

$$\Delta Y_{im} = \frac{4(\lambda\alpha)^2}{(\lambda\alpha_L)} \tag{2.101}$$

From (2.100) and (2.101), the transduction parameter can be given by

$$(\lambda\alpha)^2 = \frac{\pi}{4}\frac{\Delta Y_{im}\Delta f_{ip}}{f_0} \tag{2.102}$$

With the help of the quality factor $Q \equiv f_r/\Delta f$ of the resonant peak, the real and the imaginary parts of the admittance may be expressed in the form:

$$\begin{aligned} Y_r(f) &= \frac{Y_{rm}}{4Q^2\left(\frac{f}{f_r}-1\right)^2+1} & (2.103)\\ Y_i(f) &= -Y_{rm}\frac{2Q\left(\frac{f}{f_r}-1\right)}{4Q^2\left(\frac{f}{f_r}-1\right)^2+1}+2\pi f C_P & (2.104)\end{aligned}$$

At the anti-resonant frequency, f_{ar}, the imaginary part of the admittance becomes zero. Then,

$$Y_{rm}\frac{2Q\left(\frac{f_{ar}}{f_r}-1\right)}{4Q^2\left(\frac{f_{ar}}{f_r}-1\right)^2+1}=2\pi f_{ar}C_P \tag{2.105}$$

If

$$Q\left(\frac{f_{ar}}{f_r}-1\right)\gg 1, \tag{2.106}$$

the unity in the denominator may be ignored. Therefore,

$$\begin{aligned} Y_{rm}\frac{1}{2Q\left(\frac{f_{ar}}{f_r}-1\right)} &\simeq 2\pi f_{ar}C_P \\ Y_{rm}\frac{\Delta f}{2(f_{ar}-f_r)} &\simeq 2\pi f_{ar}C_P \\ \frac{f_{ar}-f_r}{f_0} &\simeq \frac{(\zeta\lambda_0)^2}{\pi^2 f_{ar}C_P} \end{aligned} \tag{2.107}$$

From the above derivation, we see that if the admittance curves are obtained, we can estimate the transduction coefficient and the propagation loss under a low loss approximation. Unfortunately, only the sum of κ_{11} and κ_{12} can be estimated.

2.7 Conclusion

In this chapter, the COM theory has been reviewed. There are several unknown parameters which must be derived experimentally or theoretically. These parameters are the self coupling coefficient, the mutual coupling coefficient, the transduction coefficient and the static capacitance of one electrode pair. We show that these parameters, except for the static capacitance, can be derived from the dispersion properties for the wave propagation under shorted or open gratings in a low loss approximation. The remaining unknown parameter, the static capacitance, will be computed by the space harmonic method for the generation problem, which will be explained later in Sec. 3.4 (p. 108).

On the other hand, the COM equations can also be solved for the admittance curves for SAW generation by an external applied voltage. Alternatively, from the admittance curve as a function of the frequency of the applied voltage, we can get some of the COM parameters and the propagation loss under a low loss approximation.

Chapter 3

Space Harmonic Method

3.1 Introduction

The Space Harmonic Method (SHM) is an analysis method that uses spatial harmonics as a set of orthogonal basis functions for describing the waves inside an infinite periodic structure.

The method was originally used to analyse SAW propagation in 1990 by Xue and Shui [23]. At that time, however, mechanical effects due to the existence of electrodes were neglected to simplify the problem. In the early 1990's, several authors improved the model accuracy by including a first-order approximation for stress distributions to account for thin metal electrodes [24][25].

In 1998, Sato and Abe extended this method for arbitrary electrode thickness and applied it to an Al/$Li_2B_4O_7$ structure [16]. In their analysis, they used the

Galerkin method to take boundary conditions into account, by satisfying them not at every boundary point but on the entire boundary region where the error integral is minimized. In this way, the mechanical effects due to the stress were easily included.

One of the most significant advantages of this method is that it can include both mechanical and electrical effects due to the existence of the electrode without any limitations on the electrode thickness or its shape. All types of waves can be included by the proper selection of the partial waves. This method is also easy to apply to multi-layered structures.

In this chapter, the space harmonic analysis of acoustic waves under infinite grating structures on ZnO/Diamond multi-layered substrates is presented. The procedure of the SHM for multi-layered substrates is discussed. Both the wave propagation under shorted or open gratings and the wave excitation problems are discussed by using the modified SHM.

The physical behavior of the multi-layered substrates will be examined, by calculating the displacement and the energy distributions. The COM parameters will be evaluated theoretically using the derivations discussed in Chapter 2.

3.2 Space Harmonic Method

3.2.1 Floquet's Theorem

Consider a physical quantity, $U(x_1)$ under an infinite periodic structure along the x_1 direction. If the period of the structure is P, the physical conditions at $x_1 = x$ and at $x_1 = x + P$ must be exactly the same except for a relative phase shift, which leads to the following relation

$$U(x+P) = e^{-jk_0P}U(x) \tag{3.1}$$

where k_0 is the wave number of the spatial variation in the x_1 direction. Note that the above relation does not mean the period of $U(x_1)$ is P. For example, the period becomes $2P$ when k_0 is idential with the first Bragg wavenumber ($k_0 = \pi/P$).

When eq.(3.1) holds, $U(x_1)$ can be expressed as the superposition of space harmonics

$$U(x_1) = \sum_{n=-\infty}^{\infty} A_n e^{-jk_nx_1} \tag{3.2}$$

where A_n is the amplitude and k_n is the wave number of the n-th space harmonic, where

$$k_n = k_0 + \frac{2\pi}{P}n \tag{3.3}$$

This is called Floquet's theorem. This expansion can be applied to any physical quantity under an infinite periodic structure.

3.2.2 Space Harmonic Solutions

Inside the dielectric medium, the governing equations are Newton's equation of motion and Maxwell's equations under the quasi-static approximation [4]

$$\rho \frac{\partial^2 \mathbf{U}}{\partial t^2} = \nabla \cdot \mathbf{T} = \nabla \cdot (\mathbf{c} \cdot \mathbf{S} - \mathbf{e} \cdot \mathbf{E}) \tag{3.4}$$

$$\nabla \cdot \mathbf{D} = 0 \tag{3.5}$$

where $\mathbf{U}$ is the displacement vector, $\mathbf{T}$ and $\mathbf{S}$ are the stress and the strain vectors, respectively, $\mathbf{D}$ and $\mathbf{E}$ are the electrical displacement and the electrical field vectors, $\mathbf{c}$ and $\mathbf{e}$ are the elastic and the piezoelectric tensors, and ρ is the mass density. For a metal layer, only Newton's eq.(3.4) is necessary, while Maxwell's eq.(3.5) alone is needed for free space.

In general, there will be 8 partial wave solutions inside dielectric media and 6 solutions inside metal, because there will be no electromagnetic waves inside the metal. The waves can be either surface constrained, upward propagating or downward propagating waves depending on the wavenumber component in the direction parallel to the surface. These partial waves will be linearly combined to meet boundary conditions. However, if the lowest layer is assumed to be semi-infinite, only surface waves and those propagating downward are employed in the solution for the lowest layer, because there are no upward reflecting waves from the bottom. As a result, only 4 out of the 8 partial waves will be used in the lowest dielectric layer of the problem [5] [36].

Figure 3.1 shows the periodic Al grating structure on a ZnO/Diamond substrate that will be considered here, of the type that is currently commercially available. The technique described below can be adapted in a straightforward way to other structures considered in [7] by the proper formulation of the boundary condition integrals.

The periodic gratings have period P in the x_1 direction of propagation. The Al grating structure is assumed to be long in the x_2 direction, and no variation is assumed in the x_2 direction. The interface between ZnO and diamond layers is along the $x_3 = 0$ plane, with the diamond material in the negative x_3 region. The width and the thickness of the metal electrodes are represented by M and H_A, respectively. The thickness of the ZnO layer is denoted by H_Z.

In practice, a finite polycrystalline diamond thin film is grown on a silicon substrate by chemical vapor deposition (CVD) [6]. In the following calculations, however, the diamond thickness is assumed to be sufficient to ignore any contributions from the underlying Si substrate. This assumption will be valid if the acoustic energy density at the diamond/silicon interface is sufficiently low. This will require the diamond thickness to be greater than a few wavelengths of the SAW [7]. This will be shown to be the case later on the discussion of the energy distributions.

For free space, the following governing equation gives us one complex conjugate pair of solutions for the electromagnetic waves

$$\nabla \cdot \mathbf{D} = -\varepsilon_0 \nabla^2 \Phi^f = 0 \tag{3.6}$$

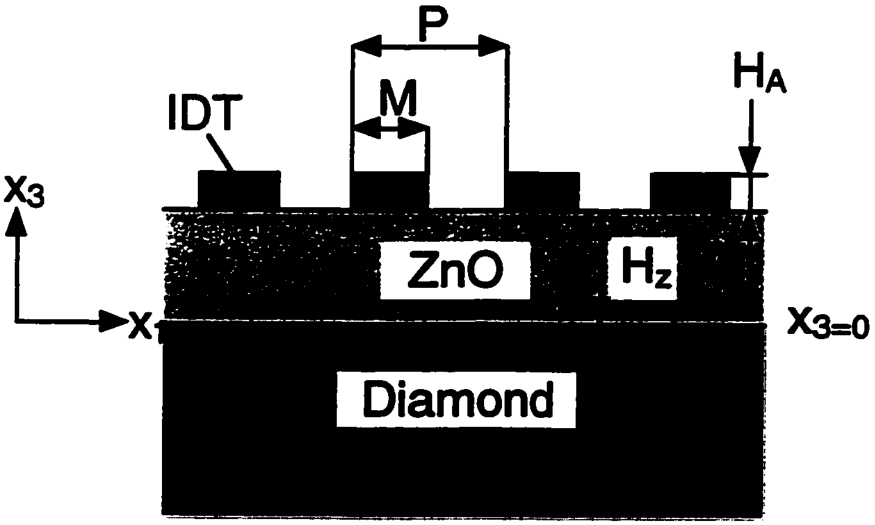

Figure 3.1: A periodic Al grating structure on a ZnO/Diamond substrate.

where ε_0 is a dielectric constant of the vacuum and Φ^f is the electric potential in free space. Only one partial wave out of these two candidates is selected for the potential by imposing the boundary condition

$$\lim_{x_3\to+\infty} \Phi^f = 0 \tag{3.7}$$

The number of partial waves inside each layer is, therefore, 4 for diamond, 8 for ZnO, 6 for Al and 1 for free space.

Taking Floquet's theorem into account, the resultant expressions for particle displacements U_i $(i = 1, 2, 3)$ and electrostatic potential U_4 in each region are expressed by using space harmonics

$$\text{diamond: } U_i^d = \sum_{m=-\infty}^{\infty}\sum_{n=1}^{4} A^{(m,n)}\beta_i^{(m,n)} e^{j\frac{\pi}{P}\left[\gamma\alpha^{(m,n)}x_3+(\gamma+2m)x_1-f(2P)t\right]} \quad (i = 1, 2, 3, 4) \tag{3.8}$$

$$\text{ZnO: } U_i^z = \sum_{m=-\infty}^{\infty}\sum_{n=5}^{12} A^{(m,n)}\beta_i^{(m,n)} e^{j\frac{\pi}{P}\left[\gamma\alpha^{(m,n)}x_3+(\gamma+2m)x_1-f(2P)t\right]} \quad (i = 1, 2, 3, 4) \tag{3.9}$$

$$\text{Al electrode: } U_k^m = \sum_{m=-\infty}^{\infty}\sum_{n=13}^{18} A^{(m,n)}\beta_k^{(m,n)} e^{j\frac{\pi}{P}\left[\gamma\alpha^{(m,n)}x_3+(\gamma+2m)x_1-f(2P)t\right]} \quad (k = 1, 2, 3) \tag{3.10}$$

$$\text{free space: } U_4^f = \sum_{m=-\infty}^{\infty} A^{(m,19)}\beta_4^{(m,19)} e^{j\frac{\pi}{P}\left[\gamma\alpha^{(m,19)}x_3+(\gamma+2m)x_1-f(2P)t\right]} \tag{3.11}$$

where m denotes the m-th space harmonic and n is the index of the partial waves inside the layers. $A^{(m,n)}$, $\beta_k^{(m,n)}$ and $\alpha^{(m,n)}$ are the weighting factors, the relative amplitudes for the partial wave vectors and the decay factors in the x_3 direction, respectively. γ is the wavenumber normalized to the first Bragg wavenumber and f is the frequency.

The decaying factor $\alpha^{(m,n)}$ can be obtained for each m and n by substituting eqs.(3.8)-(3.11) into the governing equations (3.4) and/or (3.5) depending on the layer considered and by using the orthogonal relation of the each space harmonic. The orthogonal relation is given as

$$\begin{aligned} & \frac{1}{P}\int_0^P \exp(-jk_m x_1)\exp(jk_n x_1)dx_1 \\ = & \frac{1}{P}\int_0^P \exp\left\{j\frac{\pi}{P}(n-m)x_1\right\}dx_1 \\ = & \begin{cases} 0 & n \neq m \\ 1 & n = m \end{cases} \end{aligned} \tag{3.12}$$

For the dielectric substrate, this procedure leads to the following so called Christoffel equations

$$\begin{pmatrix} R_{11}(m,n) & R_{12}(m,n) & R_{13}(m,n) & R_{14}(m,n) \\ R_{21}(m,n) & R_{22}(m,n) & R_{23}(m,n) & R_{24}(m,n) \\ R_{31}(m,n) & R_{32}(m,n) & R_{33}(m,n) & R_{34}(m,n) \\ R_{41}(m,n) & R_{42}(m,n) & R_{43}(m,n) & R_{44}(m,n) \end{pmatrix} \begin{pmatrix} \beta_1^{(m,n)} \\ \beta_2^{(m,n)} \\ \beta_3^{(m,n)} \\ \beta_4^{(m,n)} \end{pmatrix} = 0 \tag{3.13}$$

where the coefficient matrix is symmetric and each component is given as follows:

$$\begin{aligned} R_{11} &= c_{11}(\gamma+2m)^2 + 2c_{15}(\gamma+2m)(\gamma\alpha^{(m,n)}) + c_{55}(\gamma\alpha^{(m,n)})^2 - \rho(f\cdot 2P)^2 \\ R_{21} &= c_{16}(\gamma+2m)^2 + (c_{14}+c_{56})(\gamma+2m)(\gamma\alpha^{(m,n)}) + c_{45}(\gamma\alpha^{(m,n)})^2 \\ R_{22} &= c_{66}(\gamma+2m)^2 + 2c_{46}(\gamma+2m)(\gamma\alpha^{(m,n)}) + c_{44}(\gamma\alpha^{(m,n)})^2 - \rho(f\cdot 2P)^2 \end{aligned}$$

$$
\begin{aligned}
R_{31} &= c_{15}(\gamma+2m)^2 + (c_{13}+c_{55})(\gamma+2m)(\gamma\alpha^{(m,n)}) + c_{35}(\gamma\alpha^{(m,n)})^2 \\
R_{32} &= c_{56}(\gamma+2m)^2 + (c_{36}+c_{45})(\gamma+2m)(\gamma\alpha^{(m,n)}) + c_{34}(\gamma\alpha^{(m,n)})^2 \\
R_{33} &= c_{55}(\gamma+2m)^2 + 2c_{35}(\gamma+2m)(\gamma\alpha^{(m,n)}) + c_{33}(\gamma\alpha^{(m,n)})^2 - \rho(f\cdot 2P)^2 \\
R_{41} &= e_{11}(\gamma+2m)^2 + (e_{15}+e_{31})(\gamma+2m)(\gamma\alpha^{(m,n)}) + e_{35}(\gamma\alpha^{(m,n)})^2 \\
R_{42} &= e_{16}(\gamma+2m)^2 + (e_{14}+e_{36})(\gamma+2m)(\gamma\alpha^{(m,n)}) + e_{34}(\gamma\alpha^{(m,n)})^2 \\
R_{43} &= e_{15}(\gamma+2m)^2 + (e_{13}+e_{35})(\gamma+2m)(\gamma\alpha^{(m,n)}) + e_{33}(\gamma\alpha^{(m,n)})^2 \\
R_{44} &= -(\varepsilon_{11}(\gamma+2m)^2 + 2\varepsilon_{13}(\gamma+2m)(\gamma\alpha^{(m,n)}) + \varepsilon_{33}(\gamma\alpha^{(m,n)})^2)
\end{aligned}
$$

In order for the solutions to be non trivial, the determinant of the above coefficient matrix must be zero. This gives us an 8th order polynomial in terms of the decaying factor, $\alpha^{(m,n)}$. For the ZnO layer, all 8 roots, corresponding to all 8 partial waves, are selected. For the diamond layer, on the other hand, a root selection is made by means of physical arguments to choose acceptable 4 solutions from the 8 candidates.

These 4 partial wave solutions are either surface or downward waves as stated before, because there is no wave source at the bottom of the diamond layer. The solutions with the negative imaginary parts are selected for the surface constrained waves. For the downward partial waves, the waves with energy flow in the negative x_3 direction are selected. To judge the energy flow direction, the fact that the energy flow direction is always normal to the slowness surface [4] is employed. Because the diamond has slowness curves which are concave and symmetric in terms of the k_{x_1}

axis shown in fig. 3.2, this condition is equivalent to the roots k_{x_3} with the negative real value.

For the Al grating, the Christoffel equation becomes,

$$\begin{pmatrix} R_{11}(m,n) & R_{12}(m,n) & R_{13}(m,n) \\ R_{21}(m,n) & R_{22}(m,n) & R_{23}(m,n) \\ R_{31}(m,n) & R_{32}(m,n) & R_{33}(m,n) \end{pmatrix} \begin{pmatrix} \beta_1^{(m,n)} \\ \beta_2^{(m,n)} \\ \beta_3^{(m,n)} \end{pmatrix} = 0 \qquad (3.14)$$

The expressions for the components, R_{ij} $(i,j=1,2,3)$, are the same as shown above. All six decaying factors, $\alpha^{(m,n)}$, are selected for the metal grating.

For free space, eq.(3.6) gives two candidates for the decaying factor, as stated before. The solution with a positive imaginary part, which satisfies eq.(3.7), is selected for $\alpha^{(m,19)}$.

Once the decaying factors are determined, the relative magnitudes of the partial wave vector $\beta_k^{(m,n)}$ can be obtained for each $\alpha^{(m,n)}$ by eqs.(3.13)-(3.14). The weighting factors $A^{(m,n)}$ are determined from mechanical and electrical boundary conditions which will be explained next.

3.2.3 Boundary Condition Integral

The boundary conditions are satisfied with the Galerkin method in the average sense[16]. Fig. 3.3 shows the mechanical and electrical boundary conditions. For mechanical boundary conditions, a metal layer of zero thickness is assumed between grating electrodes for simplicity of the computation.

At the boundary between Al, ZnO and diamond, the displacements and the

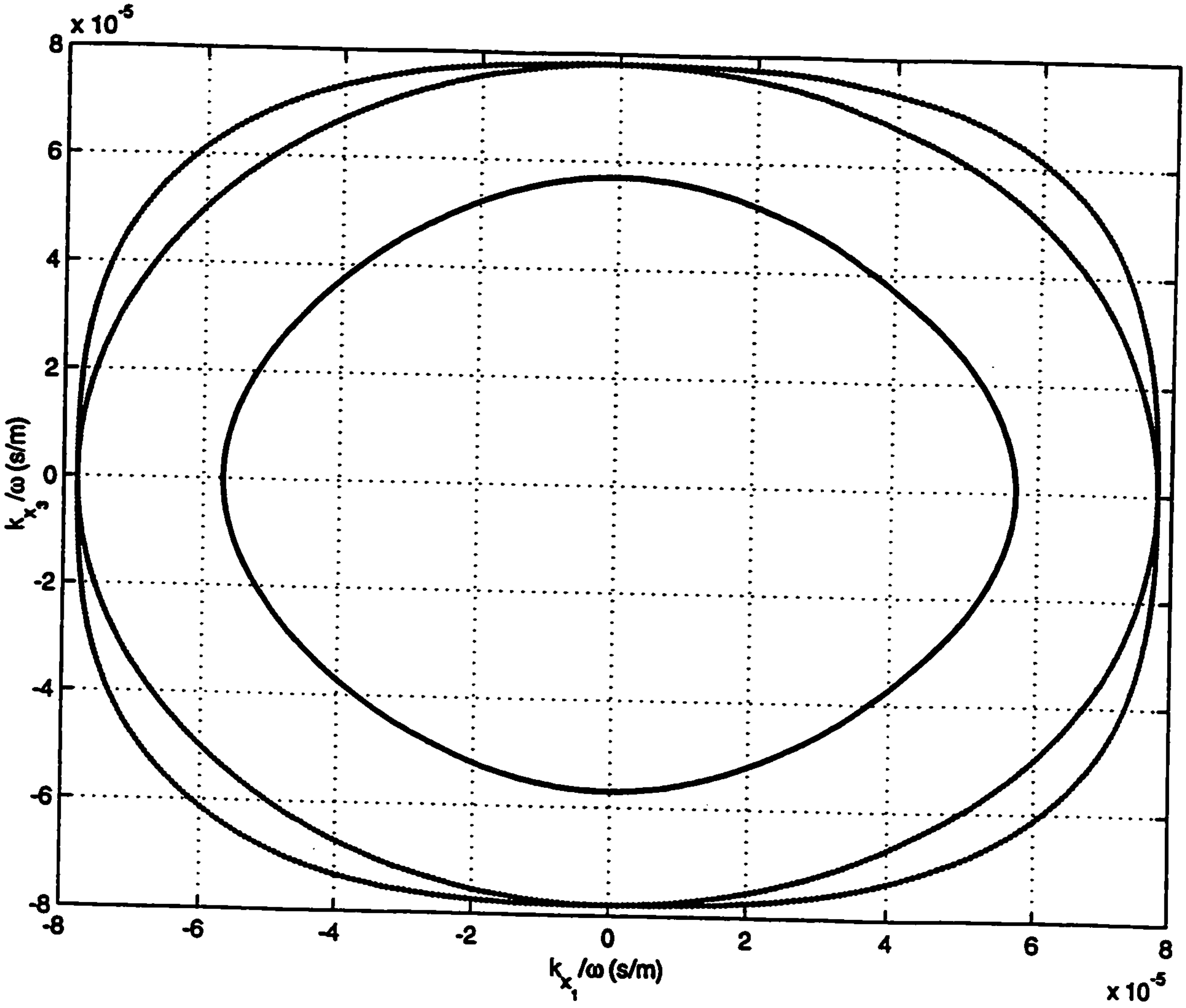

Figure 3.2: Slowness curves for the diamond. Right-handed Euler angle is <0°, 0°, 0° >.

normal stress components must be continuous, while normal stress components are required to be 0 at the interface between Al and free space. For electrical boundary conditions, the potentials and the normal components of the electrical charge displacement will be continuous at each interface. The potential is spatially constant on the metal electrode. The boundary conditions between adjacent periods are automatically satisfied by the use of space harmonics.

For the structure shown in fig. 3.3, the mechanical boundary conditions are expressed as

$$\text{diamond} \;:\; P_i^d = P_i^z \text{ (on } \Gamma_2^{d[M]} \text{) }, (i = 1,2,3), \tag{3.15}$$

$$\text{ZnO} \;:\; U_i^z = U_i^d \text{ (on } \Gamma_1^{z[M]} \text{) }, (i = 1,2,3), \tag{3.16}$$

$$P_i^z = P_i^m \text{ (on } \Gamma_2^{z[M]} \text{) }, (i = 1,2,3), \tag{3.17}$$

$$\text{metal IDT} \;:\; U_i^m = U_i^z \text{ (on } \Gamma_1^{m[M]} \text{) }, (i = 1,2,3), \tag{3.18}$$

$$P_i^m = 0 \text{ (on } \Gamma_2^{m[M]} \text{) }, (i = 1,2,3), \tag{3.19}$$

The electrical boundary conditions are

$$\text{diamond} \;:\; P_4^d = P_4^z \text{ (on } \Gamma_2^{d[E]} \text{) }, \tag{3.20}$$

$$\text{ZnO} \;:\; U_4^z = U_4^d \text{ (on } \Gamma_1^{z[E]} \text{) }, \tag{3.21}$$

$$U_4^z = V_0 e^{-j2\pi ft} \text{ (on } \Gamma_{2b}^{z[E]} \text{) }, \tag{3.22}$$

$$P_4^z = P_4^f \text{ (on } \Gamma_{2a}^{z[E]} \text{)} \tag{3.23}$$

$$\text{free space} \;:\; U_4^f = U_4^z \text{ (on } \Gamma_{1a}^{f[E]} \text{)} \tag{3.24}$$

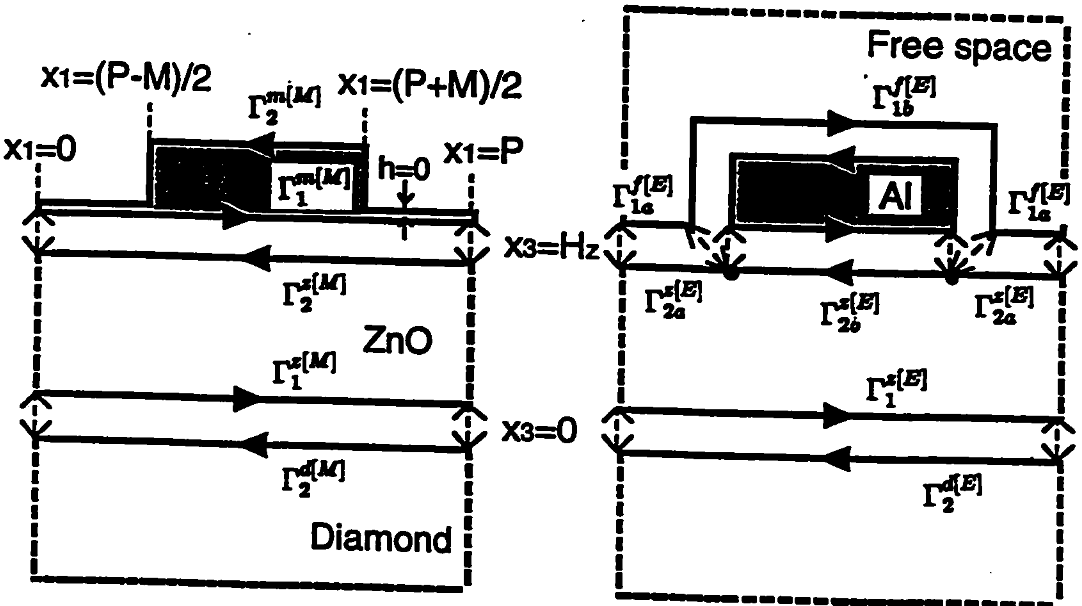

(a)Mechanical B. C. (b)Electrical B. C.

Figure 3.3: The mechanical and the electrical boundary conditions. In both figures, the joint boundary between adjacent layers has been separated to clarify the direction of integration. Boundary conditions for boundaries represented with a dashed line are automatically satisfied by the formulation.

$$U_4^f = V_0 e^{-j2\pi ft} \text{ (on } \Gamma_{1b}^{f[E]} \text{)} , \tag{3.25}$$

where V_0 is the maximum amplitude of the electric potential on the metal gratings. $U_i(i = 1,2,3,4)$ are defined in (3.8)-(3.11). $P_i(i = 1,2,3)$ are the normal stress components and P_4 is the normal components of the electrical charge displacement. For each layer, these have the following forms

$$\begin{aligned} P_i^d &= T_{ij}^d \cdot n_j \\ &= \sum_{m=-\infty}^{\infty} \sum_{n=1}^{3} A^{(m,n)} \left(j\frac{\pi}{P} \right) e^{j\frac{\pi}{P}\left[\gamma\alpha^{(m,n)}x_3 + (\gamma+2m)x_1 - f(2P)t\right]} \\ &\quad \left[\sum_{r=1}^{3} \beta_r^{(m,n)} \{ (\gamma + 2m)(c_{i1r1}^d n_1 + c_{i3r1}^d n_3) \right. \\ &\quad \left. + \gamma\alpha^{(m,n)} (c_{i1r3}^d n_1 + c_{i3r3}^d n_3) \} \right], \qquad (i = 1,2,3) \end{aligned} \tag{3.26}$$

$$\begin{aligned} P_4^d &= D_j^d \cdot n_j \\ &= -\sum_{m=-\infty}^{\infty} A^{(m,4)} \left(j\frac{\pi}{P} \right) \beta_4^{(m,4)} e^{j\frac{\pi}{P}\left[\gamma\alpha^{(m,4)}x_3 + (\gamma+2m)x_1 - f(2P)t\right]} \\ &\quad \left[\{ (\gamma + 2m)(\varepsilon_{11}^d n_1 + \varepsilon_{31}^d n_3) + \gamma\alpha^{(m,4)} (\varepsilon_{31}^d n_1 + \varepsilon_{33}^d n_3) \} \right], \end{aligned} \tag{3.27}$$

$$\begin{aligned} P_i^z &= T_{ij}^z \cdot n_j \\ &= \sum_{m=-\infty}^{\infty} \sum_{n=5}^{12} A^{(m,n)} \left(j\frac{\pi}{P} \right) e^{j\frac{\pi}{P}\left[\gamma\alpha^{(m,n)}x_3 + (\gamma+2m)x_1 - f(2P)t\right]} \\ &\quad \left[\sum_{r=1}^{3} \beta_r^{(m,n)} \{ (\gamma + 2m)(c_{i1r1}^z n_1 + c_{i3r1}^z n_3) \right. \\ &\quad + \gamma\alpha^{(m,n)} (c_{i1r3}^z n_1 + c_{i3r3}^z n_3) \} \\ &\quad + \beta_4^{(m,n)} \{ (\gamma + 2m)(e_{1i1}^z n_1 + e_{1i3}^z n_3) \\ &\quad \left. + \gamma\alpha^{(m,n)} (e_{3i1}^z n_1 + e_{3i3}^z n_3) \} \right], \qquad (i = 1,2,3) \end{aligned} \tag{3.28}$$

$$\begin{aligned} P_4^z &= D_j^z \cdot n_j \\ &= \sum_{m=-\infty}^{\infty} \sum_{n=5}^{12} A^{(m,n)} \left(j\frac{\pi}{P}\right) e^{j\frac{\pi}{P}\left[\gamma\alpha^{(m,n)}x_3+(\gamma+2m)x_1-f(2P)t\right]} \\ &\quad \left[\sum_{r=1}^{3} \beta_r^{(m,n)}\{(\gamma+2m)(e_{1r1}^z n_1 + e_{3r1}^z n_3) \right. \\ &\quad +\gamma\alpha^{(m,n)}(e_{1r3}^z n_1 + e_{3r3}^z n_3)\} \\ &\quad -\beta_4^{(m,n)}\{(\gamma+2m)(\varepsilon_{11}^z n_1 + \varepsilon_{31}^z n_3) \\ &\quad \left. +\gamma\alpha^{(m,n)}(\varepsilon_{13}^z n_1 + \varepsilon_{33}^z n_3)\}\right], \end{aligned} \tag{3.29}$$

$$\begin{aligned} P_i^m &= T_{ij}^m \cdot n_j \\ &= \sum_{m=-\infty}^{\infty} \sum_{n=13}^{18} A^{(m,n)} \left(j\frac{\pi}{P}\right) e^{j\frac{\pi}{P}\left[\gamma\alpha^{(m,n)}x_3+(\gamma+2m)x_1-f(2P)t\right]} \\ &\quad \left[\sum_{r=1}^{3} \beta_r^{(m,n)}\{(\gamma+2m)(c_{i1r1}^m n_1 + c_{i3r1}^m n_3) \right. \\ &\quad \left. +\gamma\alpha^{(m,n)}(c_{i1r3}^m n_1 + c_{i3r3}^m n_3)\}\right], \qquad (i=1,2,3) \end{aligned} \tag{3.30}$$

$$\begin{aligned} P_4^f &= D_j^f \cdot n_j \\ &= -\sum_{m=-\infty}^{\infty} A^{(m,19)} \left(j\frac{\pi}{P}\right) e^{j\frac{\pi}{P}\left[\gamma\alpha^{(m,19)}x_3+(\gamma+2m)x_1-f(2P)t\right]} \\ &\quad \beta_4^{(m,19)}\varepsilon_0\{(\gamma+2m)n_1 + \gamma\alpha^{(m,19)}n_3)\}, \end{aligned} \tag{3.31}$$

where $\mathbf{n} = (n_1, n_2, n_3)$ is the unit vector normal to the boundary, whose direction is outward from each region considered.

For each layer, the boundary conditions (3.15)-(3.25) are satisfied not at every boundary point but for the entire boundary in the average sense. This procedure yields the following boundary condition integrals for each layer

$$\begin{aligned}
\text{diamond} \quad : \quad & \int_{\Gamma_2^{d[M]}} Re[(P_i^{z*} - P_i^{d*})\delta U_i^d] d\Gamma \\
& + \int_{\Gamma_2^{d[E]}} Re[(P_4^{z*} - P_4^{d*})\delta U_4^d] d\Gamma = 0 \qquad (3.32) \\
\text{ZnO} \quad : \quad & \int_{\Gamma_1^{z[M]}} Re[(U_i^z - U_i^d)\delta P_i^{z*}] d\Gamma + \int_{\Gamma_2^{z[M]}} Re[(P_i^{m*} - P_i^{z*})\delta U_i^z d\Gamma \\
& + \int_{\Gamma_1^{z[E]}} Re[(U_4^z - U_4^d)\delta P_4^{z*}] d\Gamma \\
& + \int_{\Gamma_{2b}^{z[E]}} Re[(U_4^z - V_0 e^{-j2\pi f t})\delta P_4^{z*}] d\Gamma \\
& + \int_{\Gamma_{2a}^{z[E]}} Re[(P_4^{f*} - P_4^{z*})\delta U_4^z] d\Gamma = 0 \qquad (3.33) \\
\text{metal IDT} \quad : \quad & \int_{\Gamma_1^{m[M]}} Re[(U_i^m - U_i^z)\delta P_i^{m*}] d\Gamma \\
& + \int_{\Gamma_2^{m[M]}} Re[(-P_i^{m*})\delta U_i^m] d\Gamma = 0 \qquad (3.34) \\
\text{free space} \quad : \quad & \int_{\Gamma_{1a}^{f[E]}} Re[(U_4^f - U_4^z)\delta P_4^{f*}] d\Gamma \\
& + \int_{\Gamma_{1b}^{f[E]}} Re[(U_4^f - V_0 e^{-j2\pi f t})\delta P_4^{f*}] d\Gamma = 0 \qquad (3.35)
\end{aligned}$$

where the asterisk (*) denotes the complex conjugate. δU_i and δP_i represent the virtual increments of U_i and P_i, respectively.

We then get the following equations from eqs.(3.32)-(3.35)

$$\sum_{m'=-\infty}^{\infty} \sum_{n'=1}^{4} \left[F_R^{(m',n')} \cdot Re\left(\delta A^{(m',n')}\right) + F_I^{(m',n')} \cdot Im\left(\delta A^{(m',n')}\right)\right] = 0 \qquad (3.36)$$

$$\sum_{m'=-\infty}^{\infty} \sum_{n'=5}^{12} \left[F_R^{(m',n')} \cdot Re\left(\delta A^{(m',n')}\right) + F_I^{(m',n')} \cdot Im\left(\delta A^{(m',n')}\right)\right] = 0 \qquad (3.37)$$

$$\sum_{m'=-\infty}^{\infty} \sum_{n'=13}^{18} \left[F_R^{(m',n')} \cdot Re\left(\delta A^{(m',n')}\right) + F_I^{(m',n')} \cdot Im\left(\delta A^{(m',n')}\right)\right] = 0 \qquad (3.38)$$

$$\sum_{m'=-\infty}^{\infty} \left[F_R^{(m',19)} \cdot Re\left(\delta A^{(m',19)}\right) + F_I^{(m',19)} \cdot Im\left(\delta A^{(m',19)}\right)\right] = 0 \qquad (3.39)$$

where $F_R^{(m',n')}$ and $F_I^{(m',n')}$ are linear functions of $A^{(m,n)}$ and V_0. Eqs.(3.36)-(3.39) must hold for any $\delta A^{(m',n')}$. This leads to the following set of equations in terms of the real and imaginary parts of the weighting factors $A^{(m,n)}$ and the voltage amplitude, V_0, on the electrodes

$$F_R^{(m',n',)}(V_0, A^{(-\infty,1)}, \ldots, A^{(m,n)}, \ldots, A^{(\infty,19)}) = 0 \tag{3.40}$$

$$F_I^{(m',n',)}(V_0, A^{(-\infty,1)}, \ldots, A^{(m,n)}, \ldots, A^{(\infty,19)}) = 0 \tag{3.41}$$

where $m' = -\infty$ to ∞ and $n = 1$ to 19.

Two more equations are necessary for the determination of the unknown parameters. These two equations are obtained by considering the electric state of the electrodes. For shorted gratings, V_0 is set to zero,

$$V_0 = 0 \tag{3.42}$$

and for open gratings, the total charge on the each electrode must be zero

$$Q^m = \oint_{electrode} P_4 \cdot d\Gamma = 0 \tag{3.43}$$

The direction of the integration of (3.43) must always be along the positive x_1 and x_3 directions. These conditions (3.42) and (3.43) each give us two additional equations.

Eqs.(3.40), (3.41), and (3.42) or (3.43) form a complete set of linear equations in terms of the unknowns, V_0 and $A^{(m,n)}$, which leads to the following matrix equation for these unknowns

$$\mathbf{C} \cdot \mathbf{Y} = \mathbf{0} \tag{3.44}$$

where each components of **C** matrix can be calculated from the boundary condition integrals and the vector, **Y**, consists of the real and the imaginary parts of V_0 and $A^{(m,n)}$, that is,

$$\begin{aligned}\mathbf{Y} &= [Re(V_0), Im(V_0), Re(A^{(-\infty,1)}), Im(A^{(-\infty,1)}), \ldots, \\ &\qquad Re(A^{(m,n)}), Im(A^{(m,n)}), \ldots, \\ &\qquad\qquad Re(A^{(\infty,19)}), Im(A^{(\infty,19)})]^T, \end{aligned} \tag{3.45}$$

In reality, we have to truncate the number of space harmonics to the specific value. In this case, the vector, **Y** can be expressed as

$$\begin{aligned}\mathbf{Y} &= [Re(V_0), Im(V_0), Re(A^{(-M_0,1)}), Im(A^{(-M_0,1)}), \ldots, \\ &\qquad Re(A^{(m,n)}), Im(A^{(m,n)}), \ldots, \\ &\qquad\qquad Re(A^{(M_0-1,19)}), Im(A^{(M_0-1,19)})]^T, \end{aligned} \tag{3.46}$$

3.2.4 The Procedure for Simulation

The solution for the dispersion properties of a SAW propagating under a periodic grating structure is obtained by evaluating the normalized wavenumber γ and the frequency f that satisfy the condition $det(\mathbf{C}) = 0$, where the matrix **C** is given in eq.(3.44). In the actual procedure, the normalized frequency, $f \cdot (2P)$, is set first. For the initial guess of γ, $\alpha^{(m,n)}$ and $\beta_i^{(m,n)}$ are calculated for each space harmonic and for each partial wave inside every layer. The boundary condition integrals are calculated to lead to a set of equations in terms of the real and the imaginary parts of the weighting factors and the potential amplitude. The coefficient matrix, **C**, is set up and its determinant is evaluated. For this specific frequency, a two dimensional optimization in terms of the real and imaginary parts of γ, is performed until $det(\mathbf{C})$ is zero within a specified tolerance.

In the calculations, we truncate the number of space harmonics m to some specific value $2M_0$. In this case, the space harmonics range from $m = -M_0$ to $m = M_0 - 1$. The size of the resultant matrix **C** is $(76M_0 + 2) \times (76M_0 + 2)$. The following calculations use $2M_0 = 8$. The stopband frequencies converge in the similar manner as described in [16] when M_0 increases. The stopband determination error, attributed to the use of the truncation $M_0 = 4$, is estimated to be less than 0.05% of the center frequency of the stopband in our calculation, which will cause no significant error for the calculation of COM parameters.

Fig. 3.4 shows the flowchart of a computer program for the computation of SAW dispersion properties under a periodic metal strip grating.

3.2.5 Energy Distribution

In the Al/ZnO/Diamond structure, the acoustic waves are excited by the piezoelectric property of ZnO. For a ZnO layer of finite thickness on a diamond substrate, the SAW velocity of the combined system is higher than that of semi-infinite ZnO, and the propagation characteristics are governed by the physical properties of both materials. It is therefore important to know where the acoustic energy is concentrated.

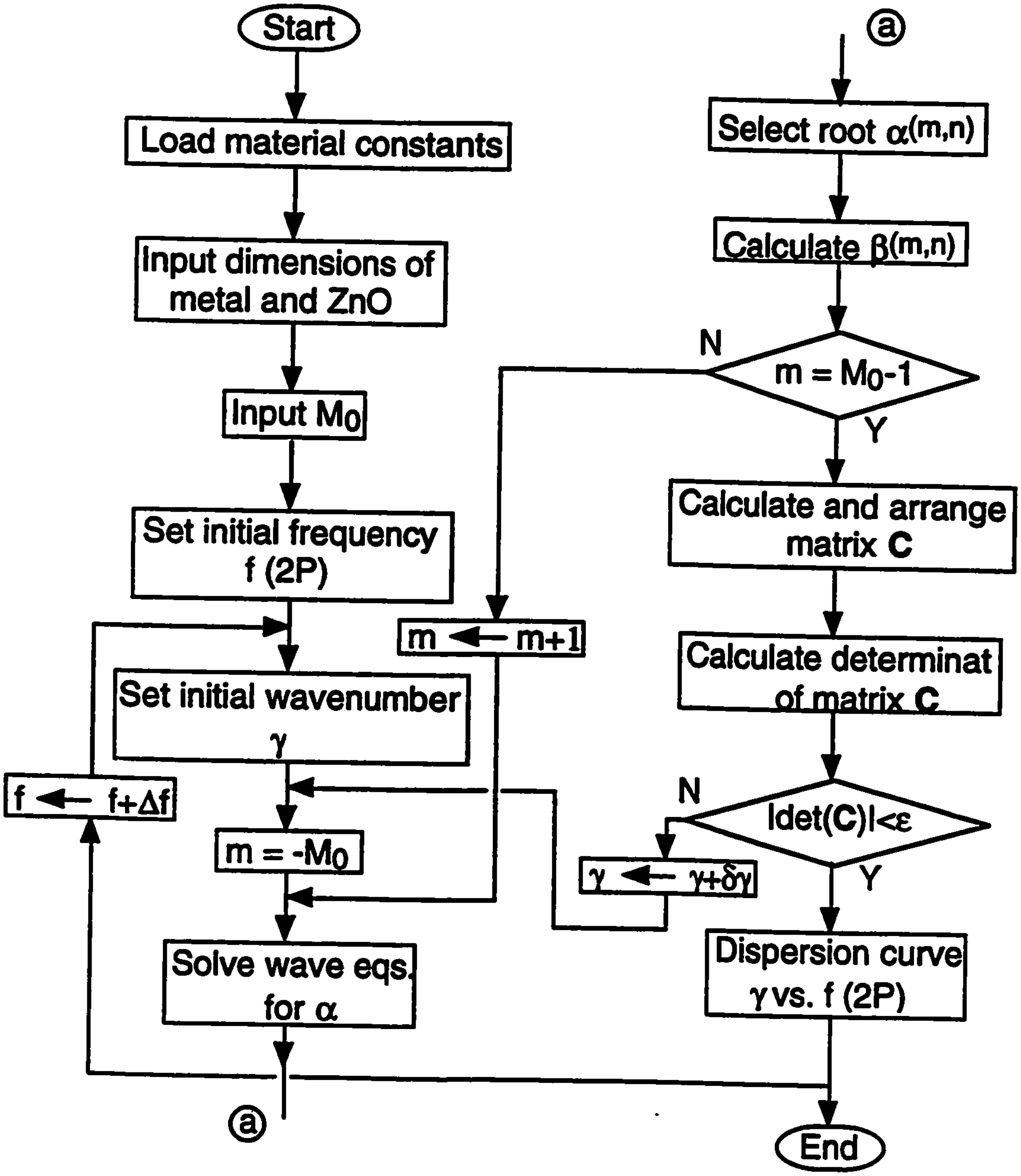

Figure 3.4: Block diagram of our calculation procedure.

Inside dielectric media, the wave energy can be divided into two mechanical energies and two electromagnetic energies. Mechanical energies consist of kinetic energy and strain energy. Electromagnetic energies are divided into electric stored energy and the magnetic stored energy. The time average of these energy densities (J/m^3) will be expressed in the complex expressions [4]

$$\text{Kinetic energy density} \;:\; E_K = \frac{1}{4}\mathbf{v}\cdot\mathbf{p}^* \tag{3.47}$$

$$\text{Strain energy density} \;:\; E_S = \frac{1}{4}\mathbf{S}\cdot\mathbf{T}^* = \frac{1}{4}\mathbf{S}\cdot(\mathbf{c}\cdot\mathbf{S}-\mathbf{e}\cdot\mathbf{E})^* \tag{3.48}$$

$$\text{Electrical stored energy density} \;:\; E_E = \frac{1}{4}\mathbf{E}\cdot\mathbf{D}^* = \frac{1}{4}\mathbf{E}\cdot(\epsilon\cdot\mathbf{E}+\mathbf{e}\cdot\mathbf{S})^* \tag{3.49}$$

$$\text{Magnetic stored energy density} \;:\; E_M = \frac{1}{4}\mathbf{H}\cdot\mathbf{B}^* \tag{3.50}$$

where $\mathbf{p}$ is the momentum, ϵ is the dielectric tensor and $\mathbf{H}$ and $\mathbf{B}$ are the magnetic field and the magnetic flux density, respectively. $*$ denotes the complex conjugate. The magnetic stored energy (3.50) can be neglected in the quasi-static approximation [4].

These energy densities can be expressed using the space harmonic description as

$$\begin{aligned} E_K \;=\; & \frac{1}{4}\rho\frac{\pi^2}{P^2}(f\cdot 2P)^2\sum_m\sum_n\sum_{m'}\sum_{n'}A^{(m,n)}A^{(m',n')*} \\ & \{\beta_1^{(m,n)}\beta_1^{(m',n')*}+\beta_2^{(m,n)}\beta_2^{(m',n')*}+\beta_3^{(m,n)}\beta_3^{(m',n')*}\} \\ & \exp\left[j\frac{\pi}{P}\left[\{\gamma\alpha^{(m,n)}-\gamma^*\alpha^{(m',n')*}\}x_3+\{(\gamma-\gamma^*)+2(m-m')\}x_1\right]\right] \end{aligned}$$

(3.51)

$$
\begin{aligned}
E_S \;=\; & \frac{1}{4}\frac{\pi^2}{P^2}\sum_m\sum_n\sum_{m'}\sum_{n'} A^{(m,n)}A^{(m',n')*} \\
& \exp\left[j\frac{\pi}{P}\left[\{\gamma\alpha^{(m,n)}-\gamma^*\alpha^{(m',n')*}\}x_3+\{(\gamma-\gamma^*)+2(m-m')\}x_1\right]\right] \\
& \left\{\sum_{i=1}^{3}\beta_i^{(m,n)}\beta_i^{(m',n')*}\{(\gamma+2m)(\gamma^*+2m')c_{i1i1}+|\gamma|^2\alpha^{(m,n)}\alpha^{(m',n')*}c_{i3i3}\}\right. \\
& +c_{13}\gamma^*(\gamma+2m)\alpha^{(m',n')*}\beta_1^{(m,n)}\beta_3^{(m',n')*} \\
& +c_{55}\gamma^*(\gamma+2m)\alpha^{(m',n')*}\beta_3^{(m,n)}\beta_1^{(m',n')*} \\
& +c_{31}\gamma(\gamma^*+2m')\alpha^{(m,n)}\beta_3^{(m,n)}\beta_1^{(m',n')*} \\
& +c_{55}\gamma(\gamma^*+2m')\alpha^{(m,n)}\beta_1^{(m,n)}\beta_3^{(m',n')*} \\
& +e_{31}(\gamma+2m)\gamma^*\alpha^{(m',n')*}\beta_1^{(m,n)}\beta_4^{(m',n')*} \\
& +e_{33}|\gamma|^2\alpha^{(m,n)}\alpha^{(m',n')*}\beta_3^{(m,n)}\beta_4^{(m',n')*} \\
& +e_{15}\gamma(\gamma^*+2m')\alpha^{(m,n)}\beta_1^{(m,n)}\beta_4^{(m',n')*} \\
& \left.+e_{15}(\gamma+2m)(\gamma^*+2m')\beta_3^{(m,n)}\beta_4^{(m',n')*}\right\}
\end{aligned}
\tag{3.52}
$$

$$
\begin{aligned}
E_E \;=\; & \frac{1}{4}\frac{\pi^2}{P^2}\sum_m\sum_n\sum_{m'}\sum_{n'} A^{(m,n)}A^{(m',n')*} \\
& \exp\left[j\frac{\pi}{P}\left[\{\gamma\alpha^{(m,n)}-\gamma^*\alpha^{(m',n')*}\}x_3+\{(\gamma-\gamma^*)+2(m-m')\}x_1\right]\right] \\
& \Big\{\epsilon_{11}(\gamma+2m)(\gamma^*+2m')\beta_4^{(m,n)}\beta_4^{(m',n')*} \\
& +\epsilon_{33}|\gamma|^2\alpha^{(m,n)}\alpha^{(m',n')*}\beta_4^{(m,n)}\beta_4^{(m',n')*} \\
& -e_{31}\gamma(\gamma^*+2m')\alpha^{(m,n)}\beta_4^{(m,n)}\beta_1^{(m',n')*} \\
& -e_{33}|\gamma|^2\alpha^{(m,n)}\alpha^{(m',n')*}\beta_4^{(m,n)}\beta_3^{(m',n')*}
\end{aligned}
$$

$$
\begin{aligned}
&-e_{15}(\gamma+2m)\gamma^{*}\alpha^{(m',n')*}\beta_4^{(m,n)}\beta_1^{(m',n')*}\\
&-e_{15}(\gamma+2m)(\gamma^{*}+2m')\beta_4^{(m,n)}\beta_3^{(m',n')*}\Big\}
\end{aligned}
\tag{3.53}
$$

As is clear from (3.51)-(3.53), the amount of energy density will depend on the amplitude of the partial wave $A^{(m,n)}$ and on the period of the grating P, which allows us only to estimate the relative energy in terms of some reference value.

3.3 Results and Discussion

The material constants used in the analysis are taken from [41]. The diamond layer is assumed to be a single crystal, because the unpredictable nature of polycrystalline diamond makes the crystalline approximation necessary. The ZnO thin film is *c*-axis oriented, which is a necessary condition for ZnO to exhibit piezoelectricity. The right-handed Euler angles are set at <0°, 0°, 0° > for all materials. This Euler angle is a valid assumption for Al and ZnO, because Al is isotropic and ZnO has a 6*mm* crystalline structure which is uniaxial along the *c*-axis in its electrical and elastic properties [4].

In the ZnO/Diamond substrate, there will exist a number of higher-order modes called Sezawa waves, whose velocity as a function of normalized ZnO thickness, kH_{ZnO}, where k is a wavenumber of the SAW wave and H_{ZnO} is the ZnO thickness, is shown in fig. 3.5. In fig. 3.5, the SAW velocities are calculated for ZnO/Diamond substrates with no surface electrodes by using the similar calculation method shown in [42] [43]. We can see that there are a series of higher SAW modes with higher velocities. In this figure, we show up to the second order Sezawa mode.

In the following calculations, three ZnO thickness are considered $H_Z = P/\pi$, $H_Z = 1.5P/\pi$ and $H_Z = 1.75P/\pi$, and the Al thickness ranges from $H_A = 0$ to $H_A = 0.05P$. We selected these thicknesses for their high acoustic velocity and their relatively high electro-mechanical coupling coefficient k^2 for the second Sezawa mode. k^2 is calculated to be 1.07% for the second mode when $H_Z = P/\pi$ [40]. This ZnO thickness corresponds to $kH_{ZnO} = 1.0$ in fig. 3.5. The second mode is concentrated on for $H_Z = P/\pi$ and $H_Z = 1.5P/\pi$, and the first Sezawa mode is considered for $H_Z = 1.75P/\pi$. The width of the Al grating is $M = 0.5P$ for all the calculations. The number of the space harmonics is set to $2M_0 = 8$.

3.3.1 Dispersion Diagram

Fig. 3.6 shows the calculated dispersion properties of the second Sezawa mode for both shorted and open gratings around the first Bragg wavenumber, where $H_Z = P/\pi$ and the thickness of Al is 0, $H_A = 0$. In this case, there will be only an electrical effect due to the existence of the gratings. In this figure, the horizontal axis corresponds to either the real or imaginary part of the normalized wavenumber γ. The vertical axis corresponds to the normalized frequency $(f \cdot 2P)$, which has a dimension of velocity. The left hand part is for shorted gratings and the right hand side for open gratings. There is a clear stopband on the dispersion curve, which is discussed in Sec. 2.4

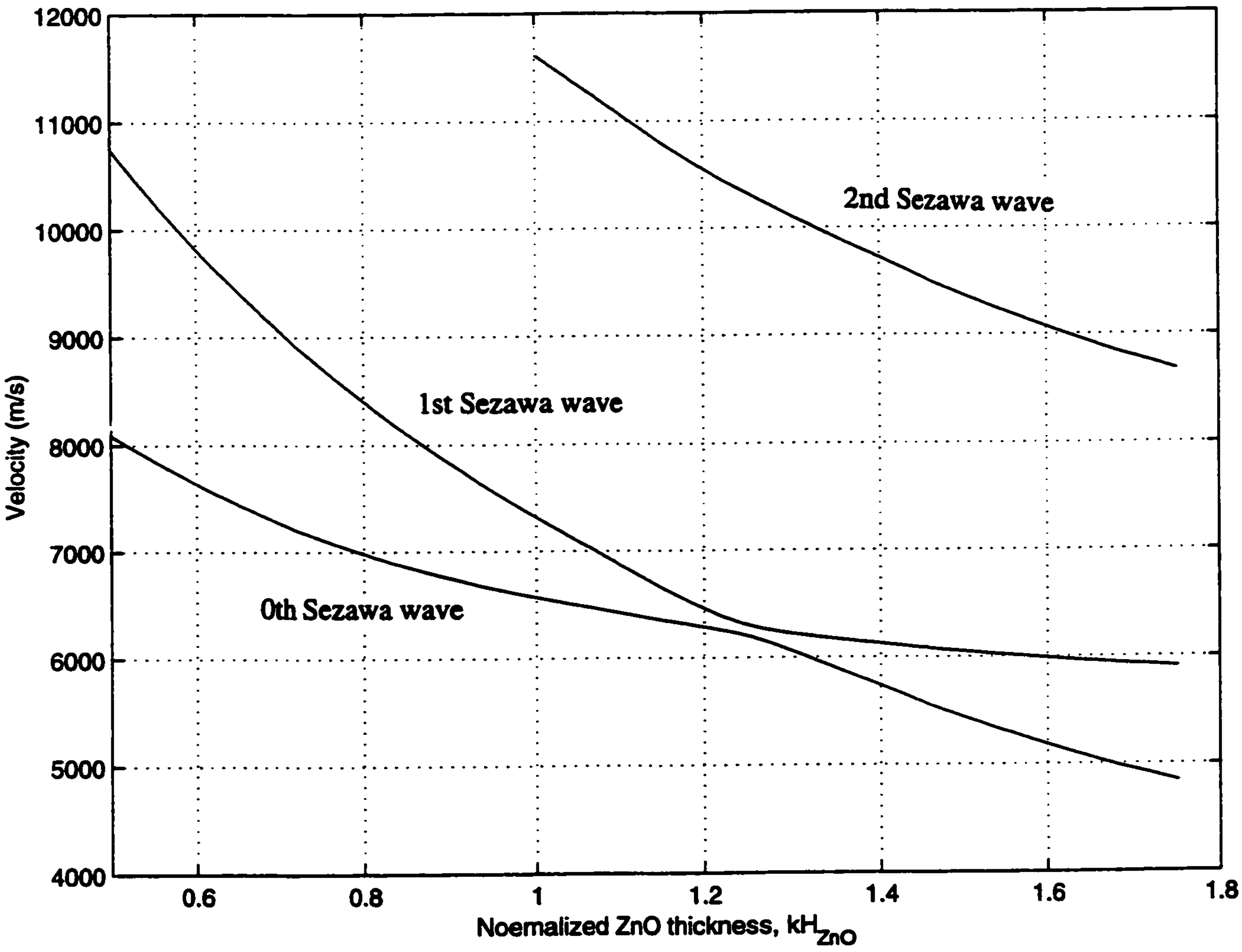

Figure 3.5: SAW velocity of the ZnO/Diamond substrate as a function of the ZnO thickness.

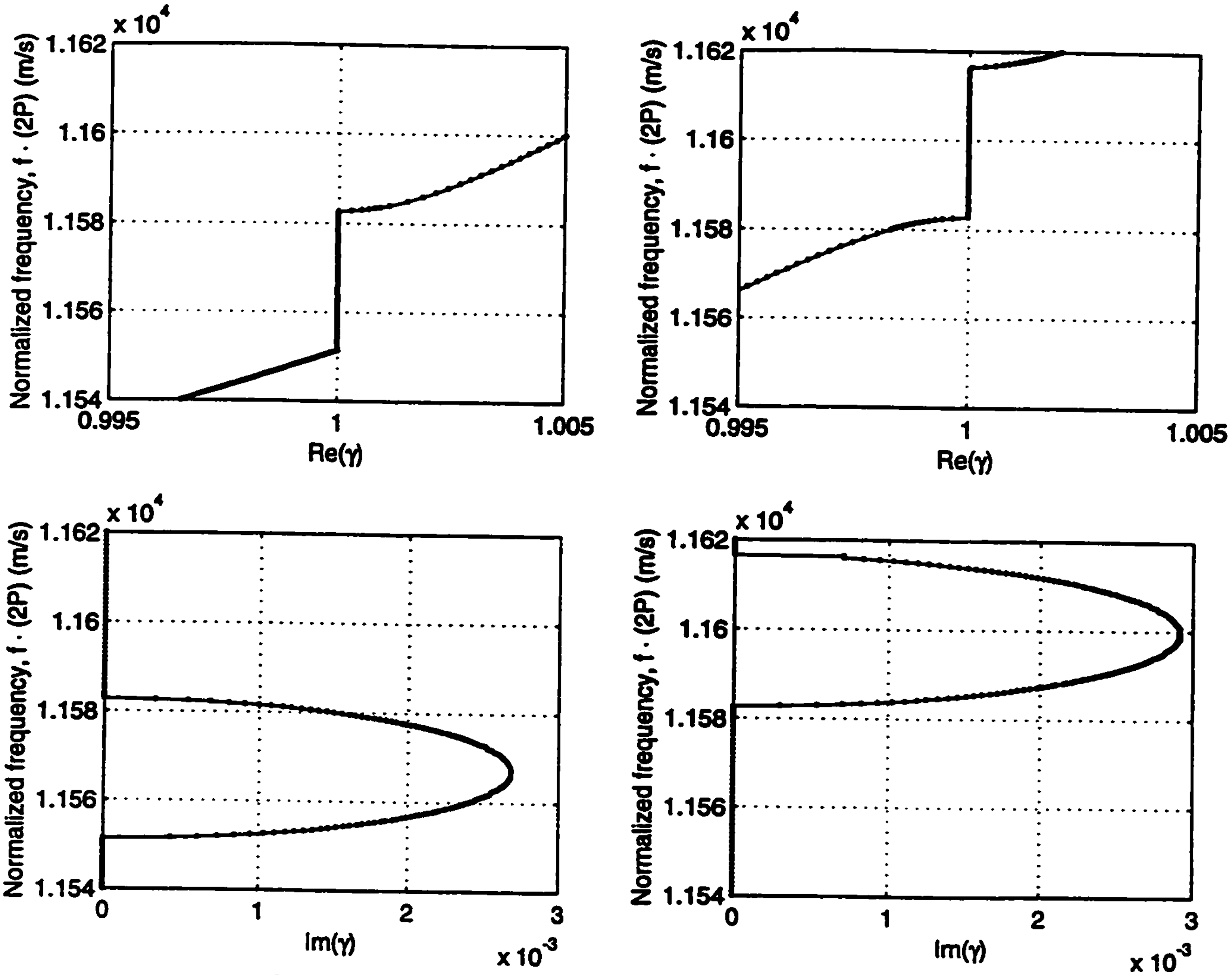

(a) shorted gratings

(b) open gratings

Figure 3.6: Dispersion curves of the second Sezawa wave under a infinite periodic grating structure, where $H_Z = P/\pi$ and $H_A = 0$. Upper figures are for real part of normalized wave number and lower figures are for imaginary part of normalized wave number. (a)Shorted gratings (b)Open gratings.

(p. 31). The normalized stopband widths are $\Delta(f \cdot 2P) = 31.4$ (m/s) for shorted gratings, and $\Delta(f \cdot 2P) = 34.0$ (m/s) for open gratings. The center frequencies of the stopbands are $f \cdot 2P = 11,567$ (m/s) for shorted and $f \cdot 2P = 11,600$ (m/s) for open gratings. Both are slower than that for the free ZnO/Diamond substrates with the same ZnO thickness, $f \cdot 2P = 11,611$ (m/s) shown in fig. 3.5, which indicates that the electrical effects reduce the SAW velocity both for open and shorted grating cases.

In fig. 3.7, the dispersion diagrams of the second Sezawa mode for $H_Z = P/\pi$ and $H_A = 0.03P$ are shown. In this case, the normalized stopband widths are $\Delta(f \cdot 2P) = 128$ (m/s) for shorted gratings, and $\Delta(f \cdot 2P) = 190$ (m/s) for open gratings. The stopband center frequencies are $(f \cdot 2P) = 11,440$ (m/s) for shorted gratings and $(f \cdot 2P) = 11,472$ (m/s) for open gratings. There are large velocity reductions due to the existence of the Al gratings with finite thickness, which is largely attributed to the mass loading effect.

The dispersion diagrams of the second mode for $H_Z = 1.5P/\pi$ and $H_A = 0.03P$ are shown in fig. 3.8. The normalized center frequencies for the stopbands are about 2,100 (m/s) smaller than those for $H_Z = P/\pi$ and the same Al thickness due to the thicker ZnO layer. The normalized stopband widths are larger for open gratings than for shorted gratings under both ZnO thickness conditions. Within the stopband for $H_Z = P/\pi$, the figure shows a small discontinuity for open gratings, which is attributed to numerical rounding errors.

For $H_A = 0.03$, both of the lower stopband frequencies, f_{ls} and f_{lo}, are

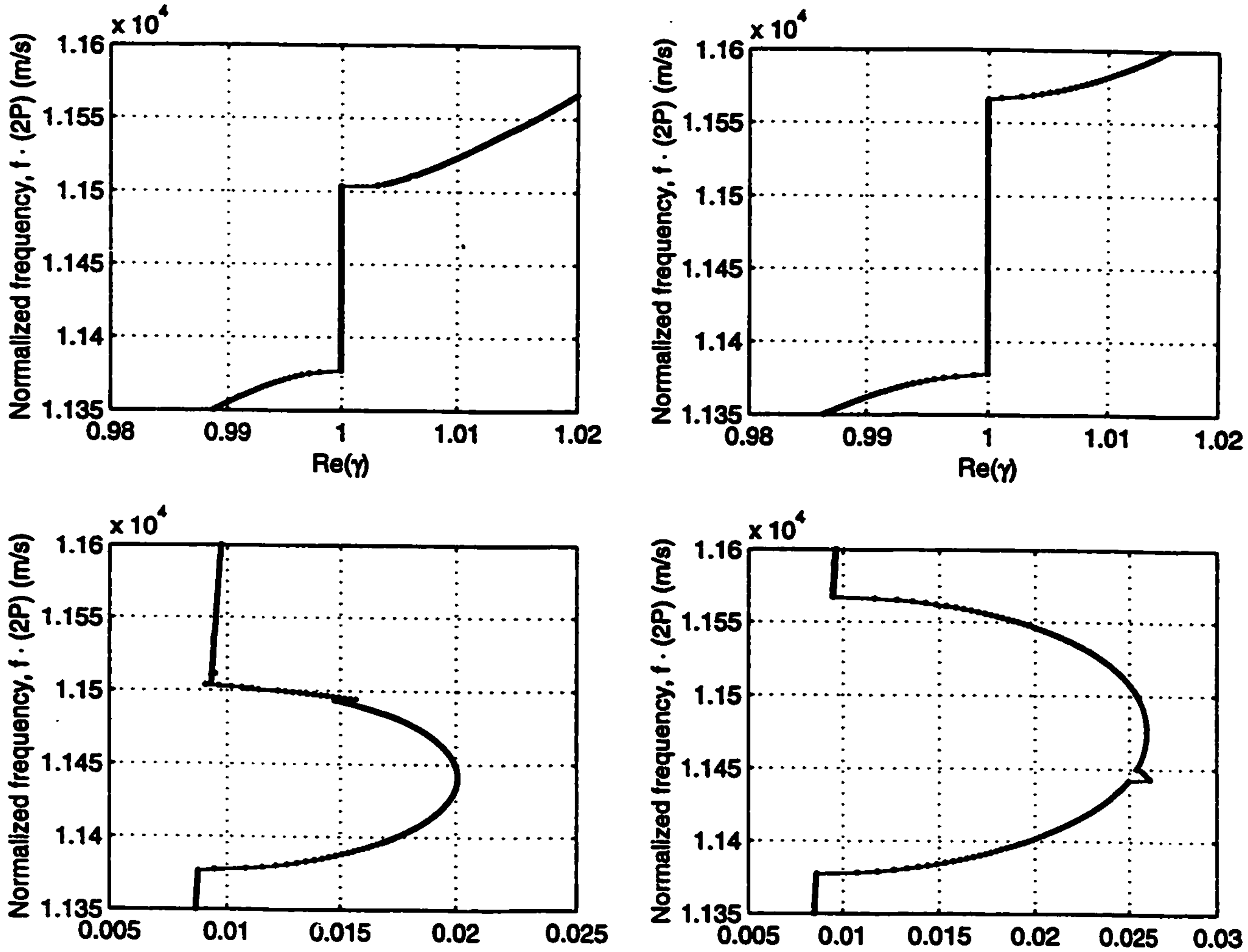

(a) shorted gratings (b) open gratings

Figure 3.7: Dispersion curves of the second Sezawa wave under an infinite periodic grating structure, where $H_Z = P/\pi$ and $H_A = 0.03P$. Upper figures are for real part of normalized wave number and lower figures are for imaginary part of normalized wave number. (a)Shorted gratings (b)Open gratings.

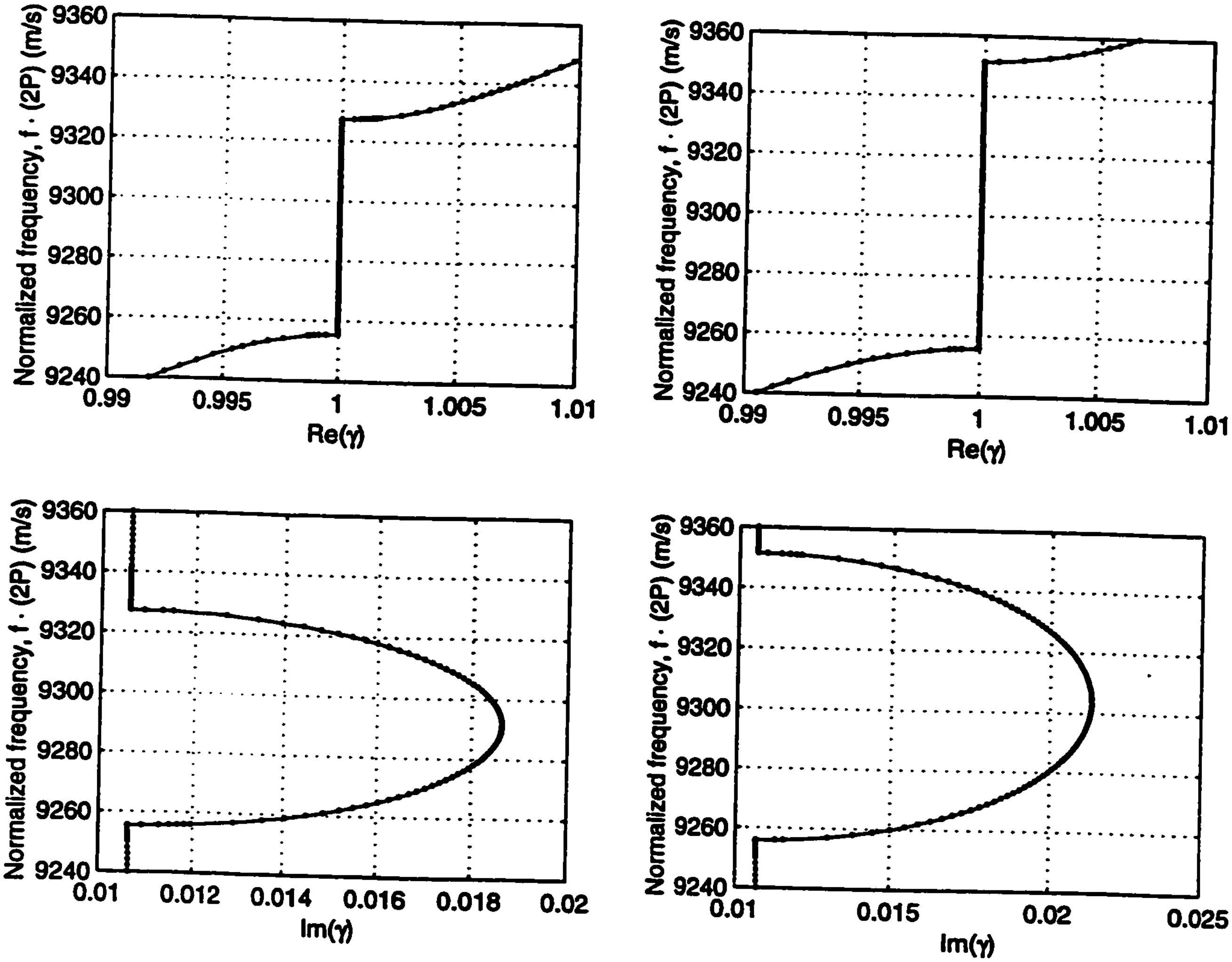

(a) shorted gratings

(b) open gratings

Figure 3.8: Dispersion curves of the second Sezawa wave under an infinite periodic grating structure, where $H_Z = 1.5P/\pi$ and $H_A = 0.03P$. Upper figures are for real part of normalized wave number and lower figures are for imaginary part of normalized wave number. (a)Shorted gratings (b)Open gratings.

identical for both ZnO thickness conditions, while the upper stopband frequency for shorted gratings, f_{us} and the lower stopband frequency for open gratings, f_{lo} are identical for $H_A = 0$. This indicates that there is a qualitative change in SAW propagation properties between these two Al thickness conditions. This situation becomes much clearer in fig. 3.9. This figure shows the stopband widths as a function of Al thickness for $H_Z = P/\pi$. For open gratings, the stopband width increases linearly as a function of Al grating thickness. The stopband width becomes 0 around $H_A = 0.006P$ for shorted gratings. The reason of this qualitative change will be clarified later in this chapter.

The dispersion diagrams are also calculated for the first mode when $H_Z = 1.75P/\pi$. Fig. 3.10 shows the dispersion properties of the first Sezawa mode when $H_Z = 1.75P/\pi$ and $H_A = 0.03P/\pi$. From fig. 3.5, SAW phase velocity without any surface electrodes is $5,905.9$ (m/s) for this condition. The stopband widths are $\Delta(f \cdot 2P) = 25.8$ (m/s) for the shorted gratings, and $\Delta(f \cdot 2P) = 35.9$ (m/s) for open gratings. The stopband centers are $f \cdot 2P = 5862.5$ (m/s) and $f \cdot 2P = 5873.9$ (m/s), respectively. As opposed to the second mode cases described above, none of the four stopband frequencies coincide.

Inside the stopband, the normalized wave number has a large imaginary part, which corresponds to propagation loss. This wave attenuation comes from the fact that there are multiple reflections inside the stopband and the wave is trapped.

For the leaky type wave, there can be some propagation loss outside the

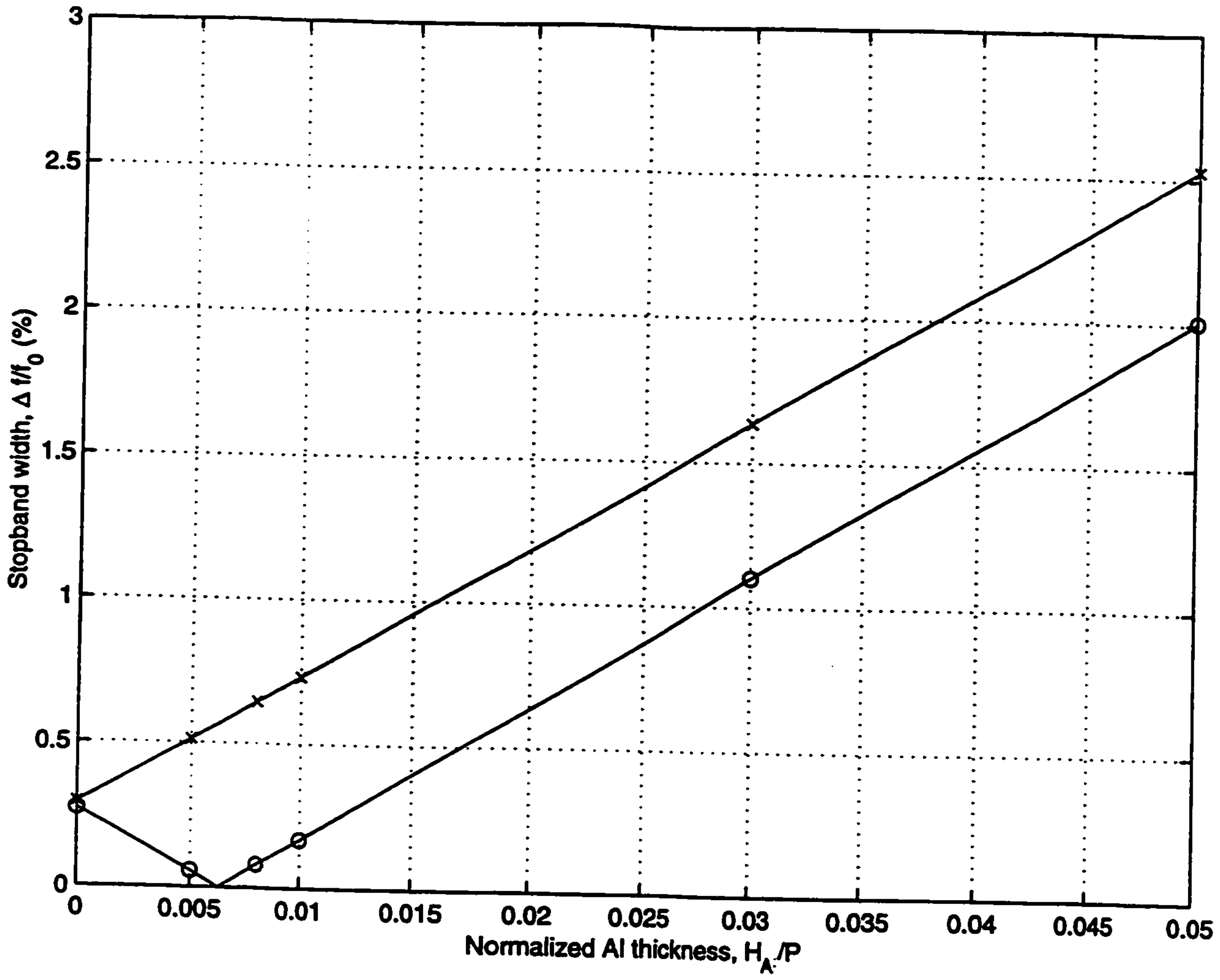

Figure 3.9: The stopband widths of the second Sezawa wave when $H_Z = P/\pi$ as a function of Al grating thickness both shorted ('o') and open ('×') gratings.

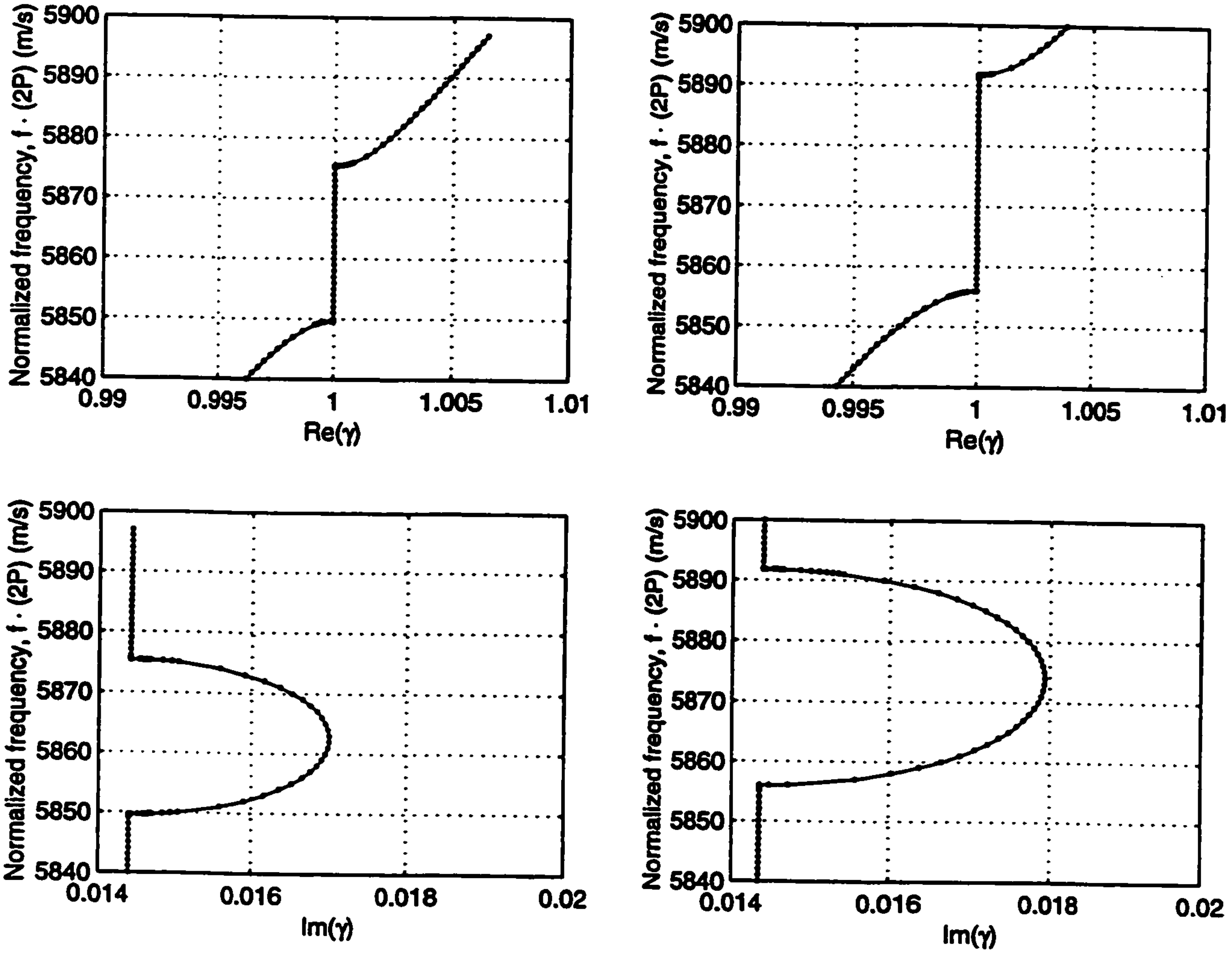

(a) shorted gratings (b) open gratings

Figure 3.10: Dispersion curves of the first Sezawa wave under an infinite periodic grating structure, where $H_Z = 1.75P/\pi$ and $H_A = 0.03P$. Upper figures are for real part of normalized wave number and lower figures are for imaginary part of normalized wave number. (a)Shorted gratings (b)Open gratings.

stopband, because some of the partial waves become of bulk type and are no longer concentrated on the surface. The propagation loss (PL) can be represented by the following expression using the real and imaginary parts of the normalized wavenumber [38].

$$PL(dB/\lambda) = 2\pi \times 20log_{10}(e) \times \frac{Im(\gamma)}{Re(\gamma)} \approx 54.6 \times \frac{Im(\gamma)}{Re(\gamma)} \tag{3.54}$$

In our case shown above, we calculated the dispersion diagram for the second order Sezawa wave around the first Bragg wavenumber, when $H_Z = P/\pi$. For this condition, all the partial waves inside the diamond are concentrated on the surface, and there is no energy leakage into the bulk. Therefore, propagation must be lossless as opposed to the case of leaky SAW. Our calculated results, however, show a small finite imaginary wavenumber for finite grating thickness, which will increase as the grating thickness increases. This can be interpreted as a computational error due to the truncation of the number of space harmonics. In order to reduce this error, we have to include higher space harmonics, which will be used for better estimations for the waves at the grating edge.

3.3.2 Displacement Distribution

The displacement distributions of the second mode inside the ZnO and diamond layers, with an arbitrary time $t = 0$ used in expressions (3.8)-(3.11) for the lower stopband edge for shorted gratings, are shown in fig. 3.11 for $H_Z = P/\pi$ and $H_A = 0.03P$. A positive x_3 corresponds to ZnO and a negative x_3 to diamond, and $x_1 = 0.5P$

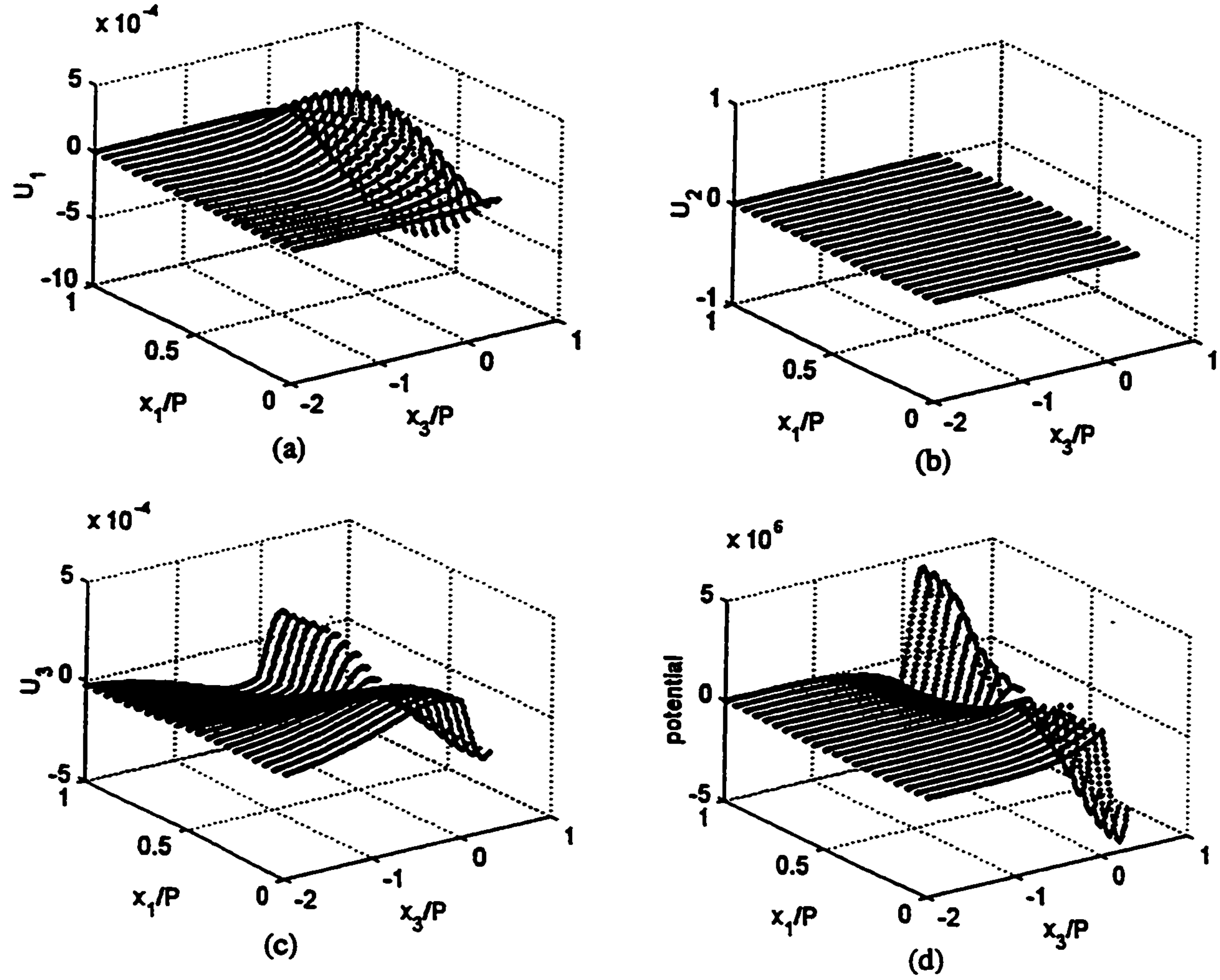

Figure 3.11: Displacement distribution of the second Sezawa mode inside Al/ZnO/Diamond structure at $t = 0$ for shorted gratings at the lower stopband edge for $H_Z = P/\pi$ and $H_A = 0.03P$. (a)Displacement distribution in the x_1 direction. (b)Displacement distribution in the x_2 direction. (c)Displacement distribution in the x_3 direction. (d)Potential distribution. Vertical axes represent arbitrary units.

is the center of the grating electrode. Fig. 3.12 shows the same results from the x_1 direction. The amplitude of the displacement clearly depends on the wave amplitude $A^{(m,n)}$, whose absolute value can not be determined for shorted and open grating conditions. Therefore, the vertical axes of these figures represent arbitrary units.

These figures show that the wave amplitudes are larger in the ZnO region than in the diamond for U_1 and the electrical potential U_4, and they attenuate rapidly in the diamond region. In the case of U_3, however, the wave amplitude is larger inside diamond and has a large penetration depth inside the diamond layer. These distributions show the typical higher order nature of Sezawa waves.

A single crystalline diamond is assumed for the calculation. Therefore, there is no coupling component between the x_2 and the remaining directions in material constants of the material considered. As a result of this assumption, there is no U_2 component in either material. For polycrystalline diamond, there may be a U_2 component if the grain size is not small enough for the isotropic approximation to be valid.

The displacement distributions for the first Sezawa mode, with $H_Z = 1.75P/\pi$ and $H_A = 0.03P$, are shown in fig. 3.13 for shorted gratings at the lower stopband edge. Fig. 3.14 shows the same results from the x_1 direction. There is no null in the U_1 component inside the ZnO layer, which is the biggest difference between the first and the second Sezawa modes.

Figs. 3.15, 3.16 and 3.17 show the standing wave patterns of the second Sezawa

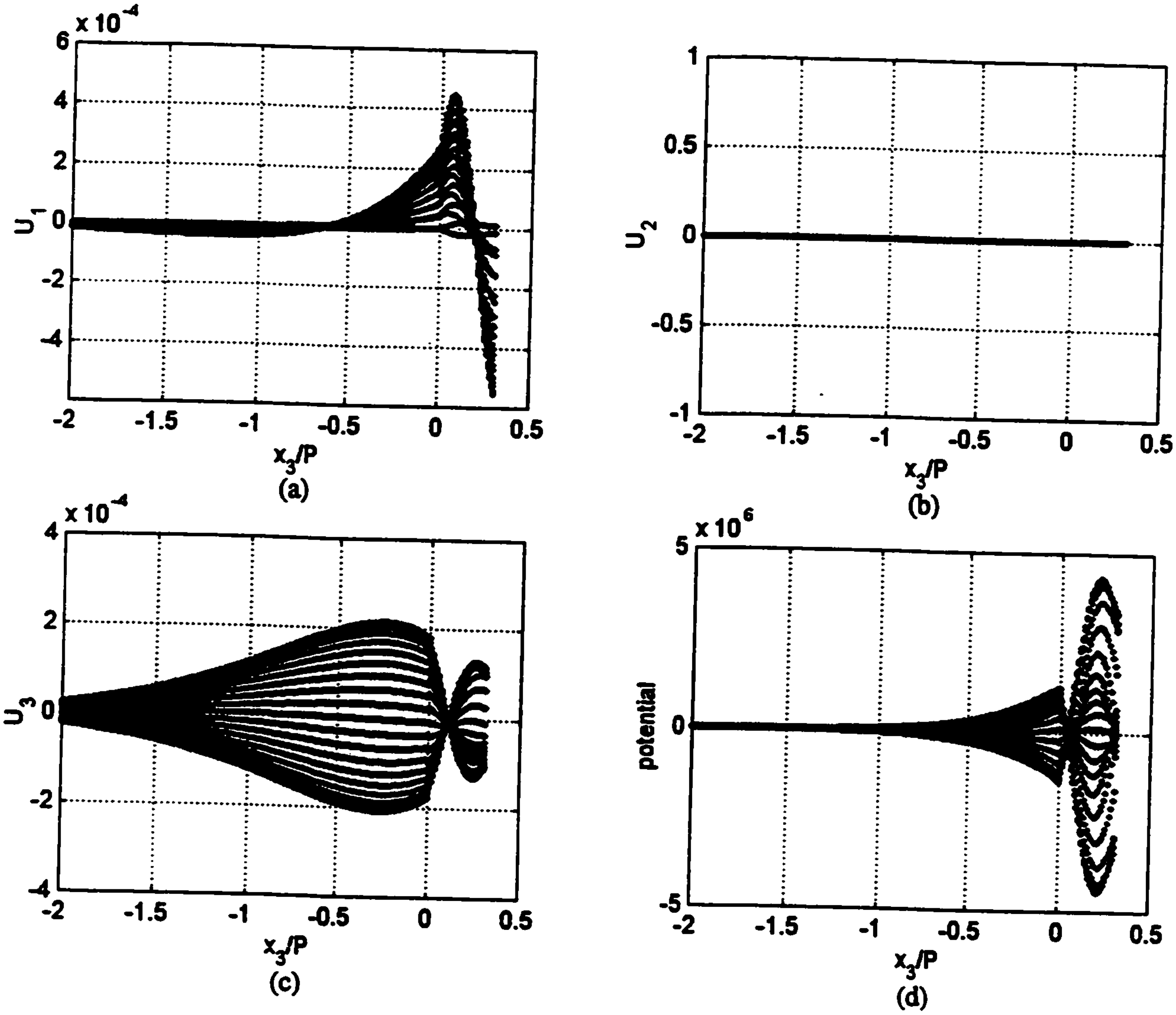

Figure 3.12: Displacement distribution of the second Sezawa mode inside Al/ZnO/Diamond structure at $t = 0$ for shorted gratings at the lower stopband edge for $H_Z = P/\pi$ and $H_A = 0.03P$. (a)Displacement distribution in the x_1 direction. (b)Displacement distribution in the x_2 direction. (c)Displacement distribution in the x_3 direction. (d)Potential distribution. Vertical axes represent arbitrary units.

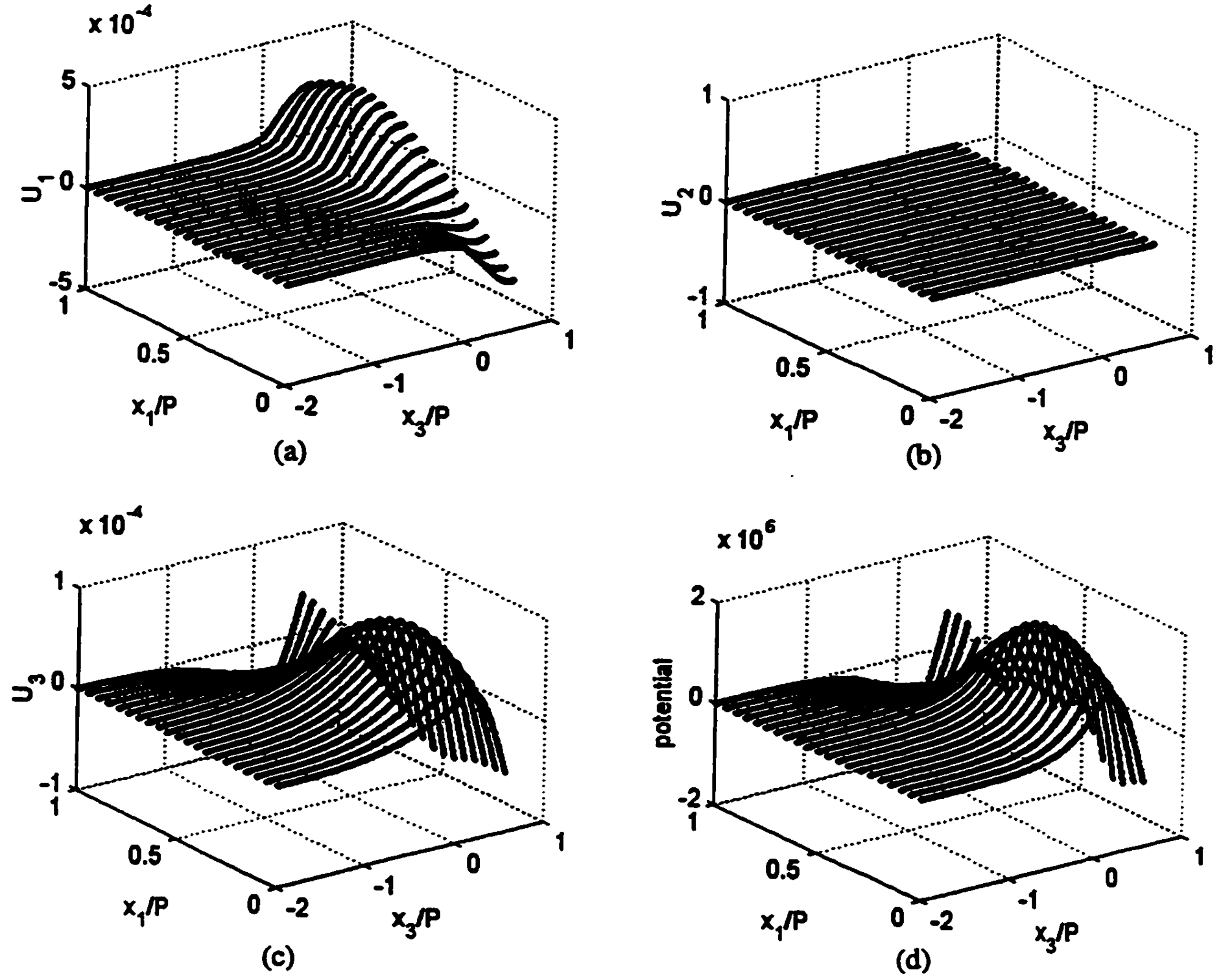

Figure 3.13: Displacement distribution of the first Sezawa mode inside Al/ZnO/Diamond structure at $t = 0$ for shorted gratings at the lower stopband edge for $H_Z = 1.75P/\pi$ and $H_A = 0.03P$. (a)Displacement distribution in the x_1 direction. (b)Displacement distribution in the x_2 direction. (c)Displacement distribution in the x_3 direction. (d)Potential distribution. Vertical axes represent arbitrary units.

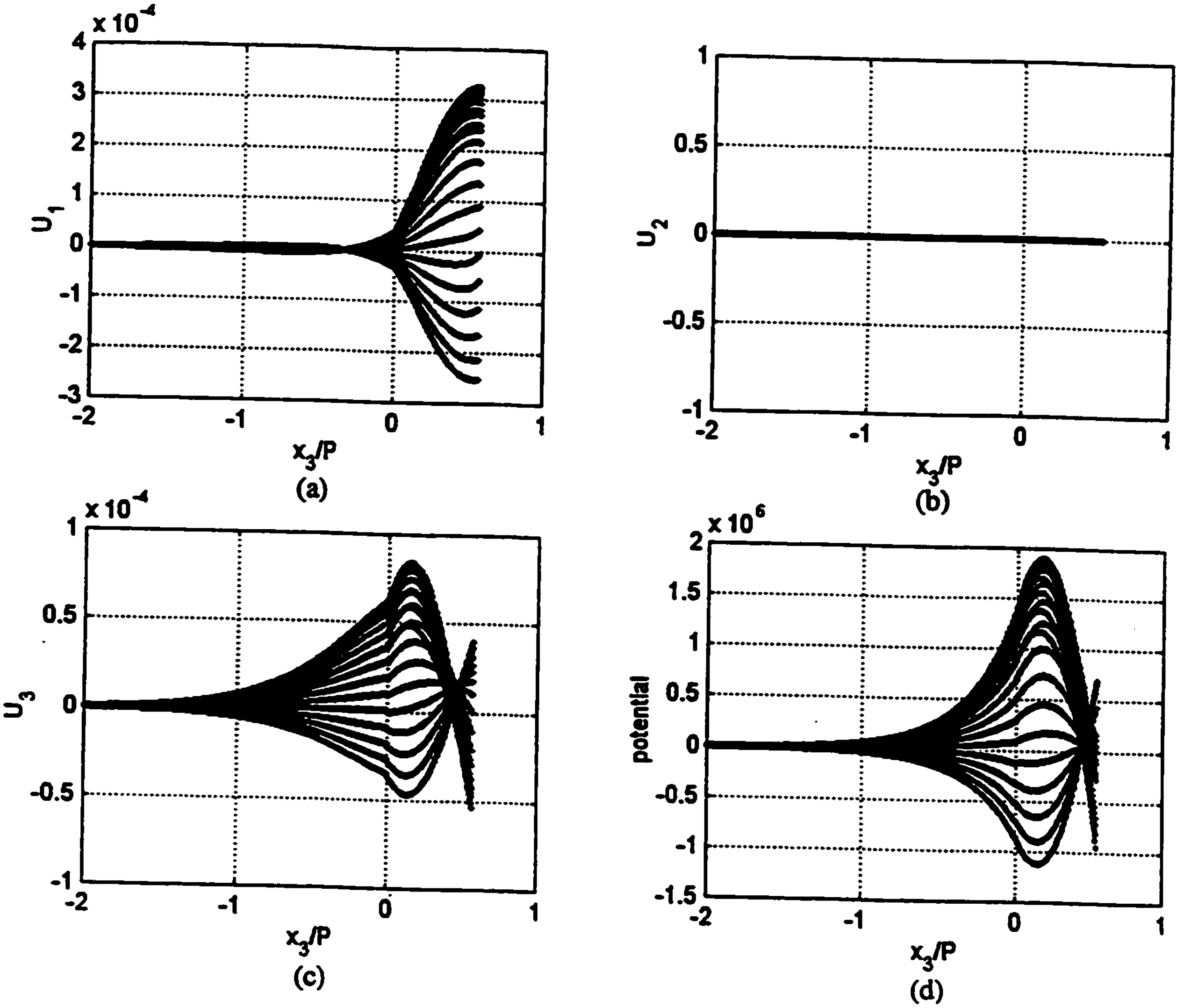

Figure 3.14: Displacement distribution of the first Sezawa mode inside Al/ZnO/Diamond structure at $t = 0$ for shorted gratings at the lower stopband edge for $H_Z = 1.75P/\pi$ and $H_A = 0.03P$. (a)Displacement distribution in the x_1 direction. (b)Displacement distribution in the x_2 direction. (c)Displacement distribution in the x_3 direction. (d)Potential distribution. Vertical axes represent arbitrary units.

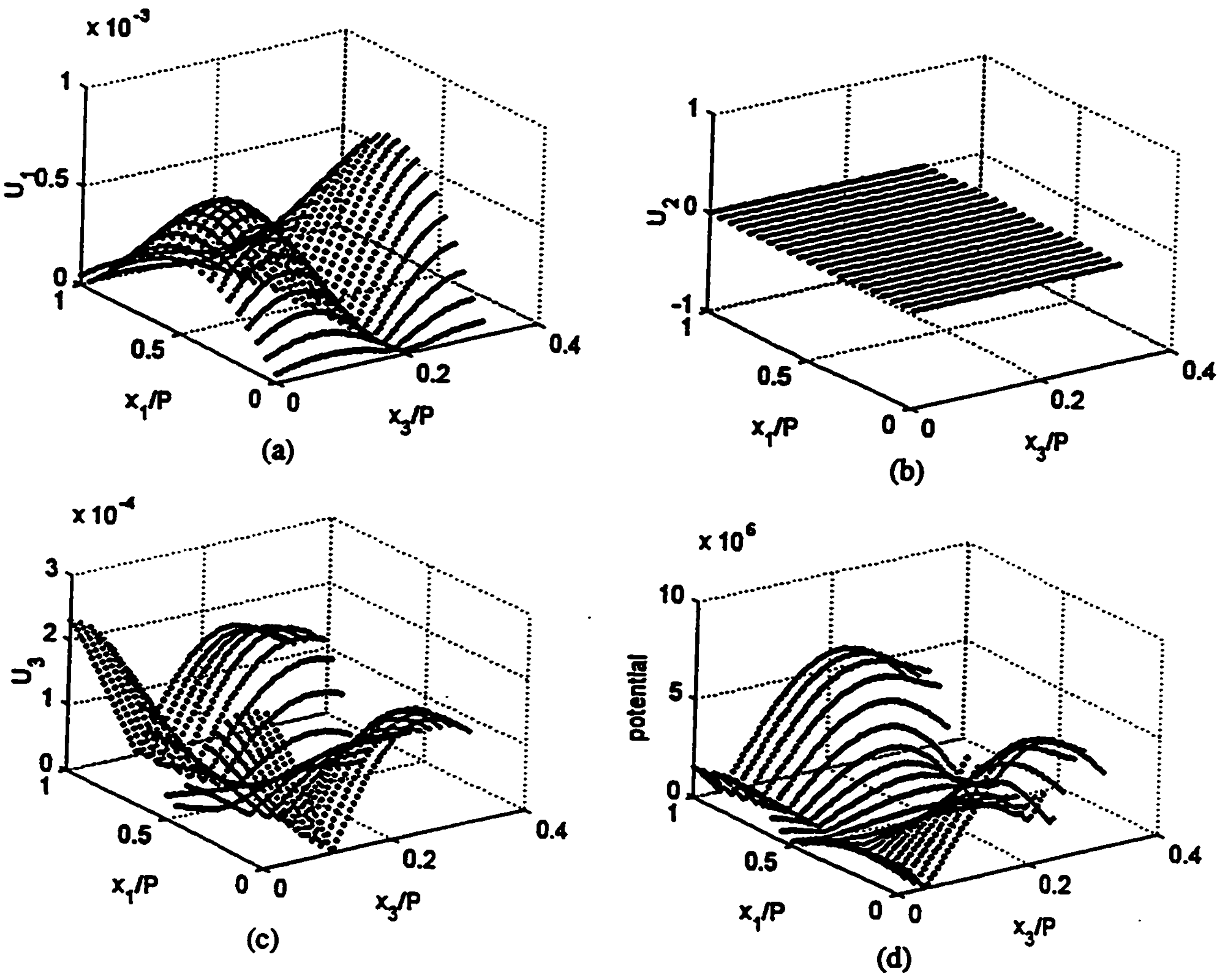

Figure 3.15: Standing wave pattern of the second mode at the lower stopband edge for shorted gratings when $H_Z = P/\pi$ and $H_A = 0.03P$. (a)Displacement standing wave pattern in the x_1 direction. (b)Displacement standing wave pattern in the x_2 direction. (c)Displacement standing wave pattern in the x_3 direction. (d)Potential standing wave pattern. Vertical axes represent arbitrary units.

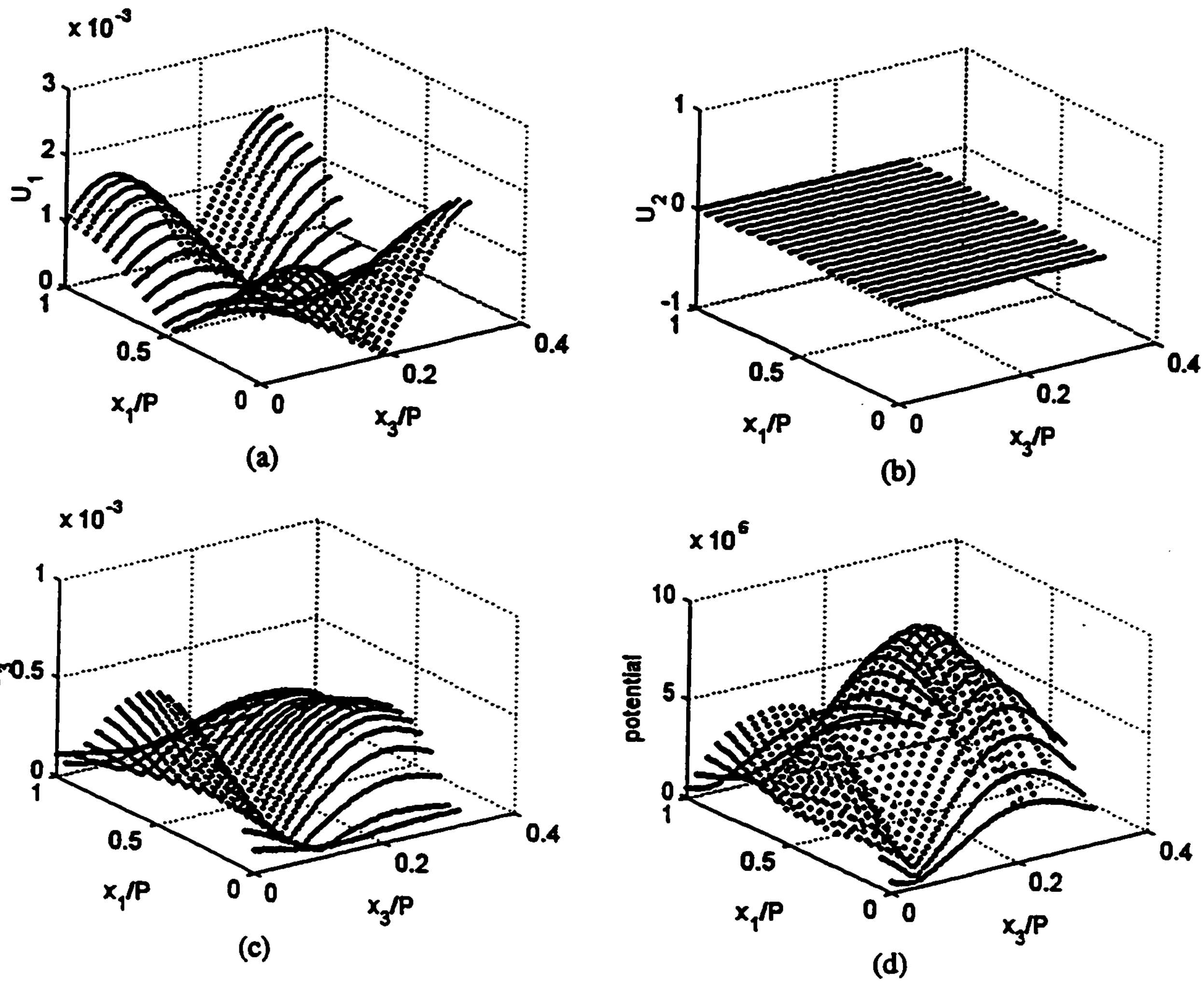

Figure 3.16: Standing wave pattern of the second mode at the upper stopband edge for shorted gratings when $H_Z = P/\pi$ and $H_A = 0.03P$. (a)Displacement standing wave pattern in the x_1 direction. (b)Displacement standing wave pattern in the x_2 direction. (c)Displacement standing wave pattern in the x_3 direction. (d)Potential standing wave pattern. Vertical axes represent arbitrary units.

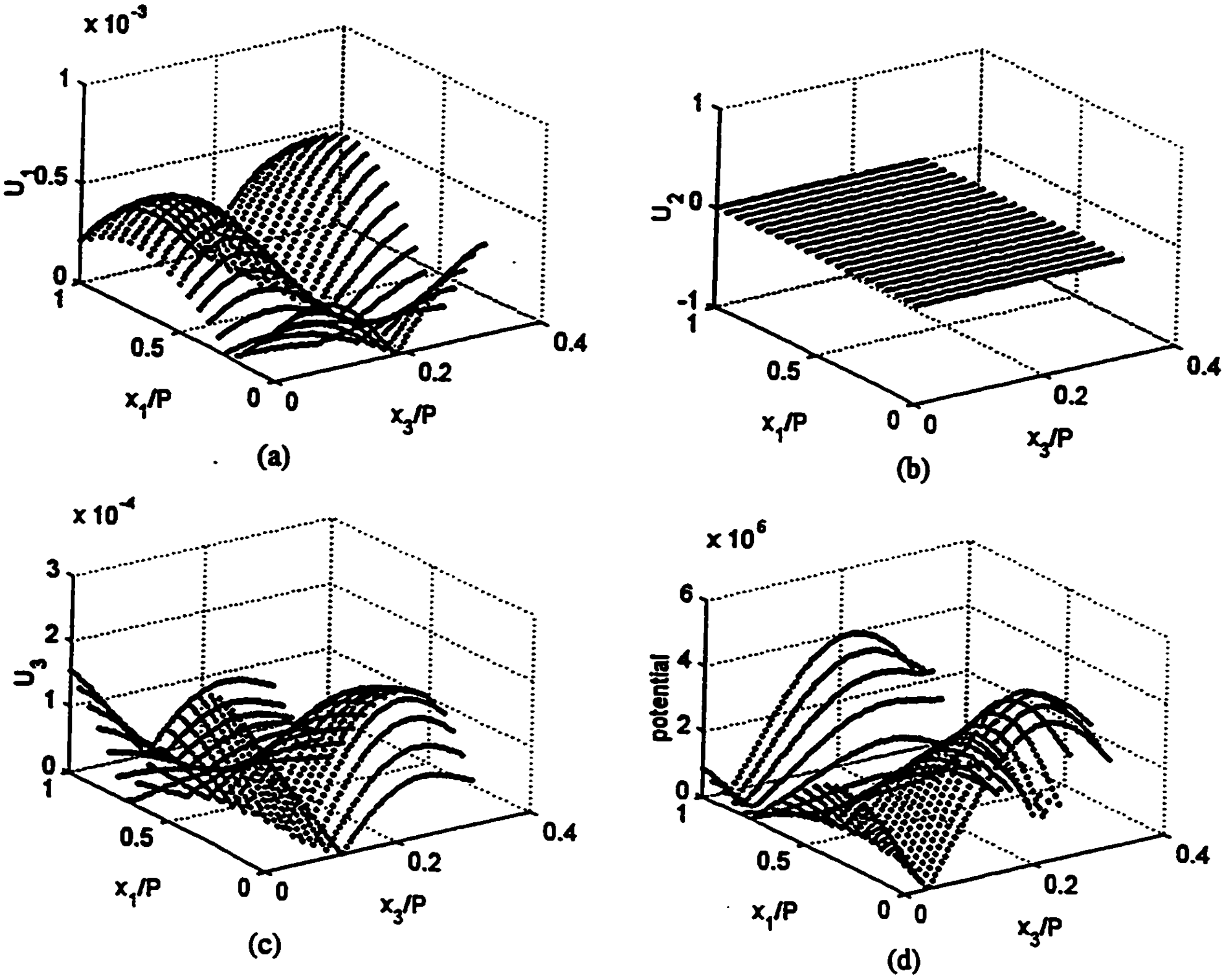

Figure 3.17: Standing wave pattern of the second mode at the stopband center for shorted gratings when $H_Z = P/\pi$ and $H_A = 0.03P$. (a)Displacement standing wave pattern in the x_1 direction. (b)Displacement standing wave pattern in the x_2 direction. (c)Displacement standing wave pattern in the x_3 direction. (d)Potential standing wave pattern. Vertical axes represent arbitrary units.

mode inside the ZnO layer at the lower stopband edge, at the upper stopband edge, and at the stopband center, respectively, for the second Sezawa waves when $H_Z = P/\pi$ and $H_A = 0.03P$. We note that the standing wave patterns for the lower and upper stopband edges are symmetric about the mid-point of the electrodes $x_1 = 0.5P$. However, there is a $\pi/2$ phase shift between them. The distribution for the stopband midpoint is no longer symmetric about the center of the grating period and has either a maximum or a minimum value at the edge of the electrode. This $\pi/2$ phase difference between the lower and upper edges of the stopband are predicted by the COM theory in Sec. 2.4 (p. 31). The similar standing wave patterns can be derived for the second Sezawa waves when $H_Z = 1.5P/\pi$ and $H_A = 0.03P$.

In figs. 3.18, 3.19 and 3.20, the standing wave patterns of the second Sezawa mode inside the ZnO layer are shown when $H_Z = P/\pi$ and $H_A = 0.005P$ for the upper edge, the lower edge and the stopband center, respectively. As opposed to the $H_A = 0.03P$ case, the potential has a maximum at the grating center for the lower stopband edge. The similar patterns are obtained when $H_A = 0$ both for $H_Z = P/\pi$ and $H_Z = 1.5P/\pi$ for the second mode.

The standing wave patterns are also calculated for the first Sezawa waves when $H_Z = 1.75P/\pi$. Fig. 3.21-3.22 show patterns for $H_A = 0$. The potential distribution inside the ZnO layer becomes maximum at the midpoint of the grating for the lower stopband edge and minimum at the upper stop band edge. The locations of the maximum and the minimum points are identical with the second Sezawa cases

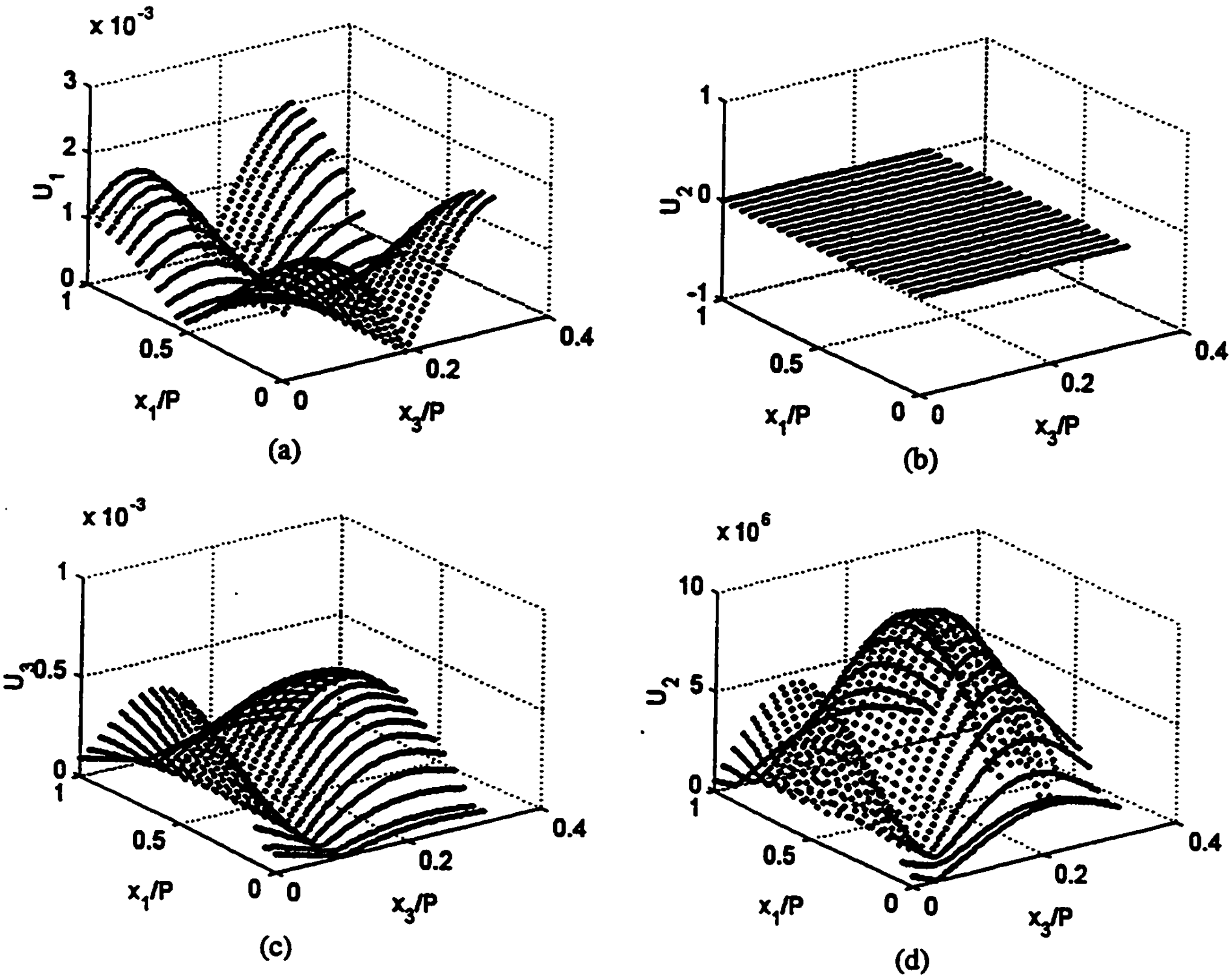

Figure 3.18: Standing wave pattern of the second mode at the lower stopband edge for shorted gratings when $H_Z = P/\pi$ and $H_A = 0.005P$. (a)Displacement standing wave pattern in the x_1 direction. (b)Displacement standing wave pattern in the x_2 direction. (c)Displacement standing wave pattern in the x_3 direction. (d)Potential standing wave pattern. Vertical axes represent arbitrary units.

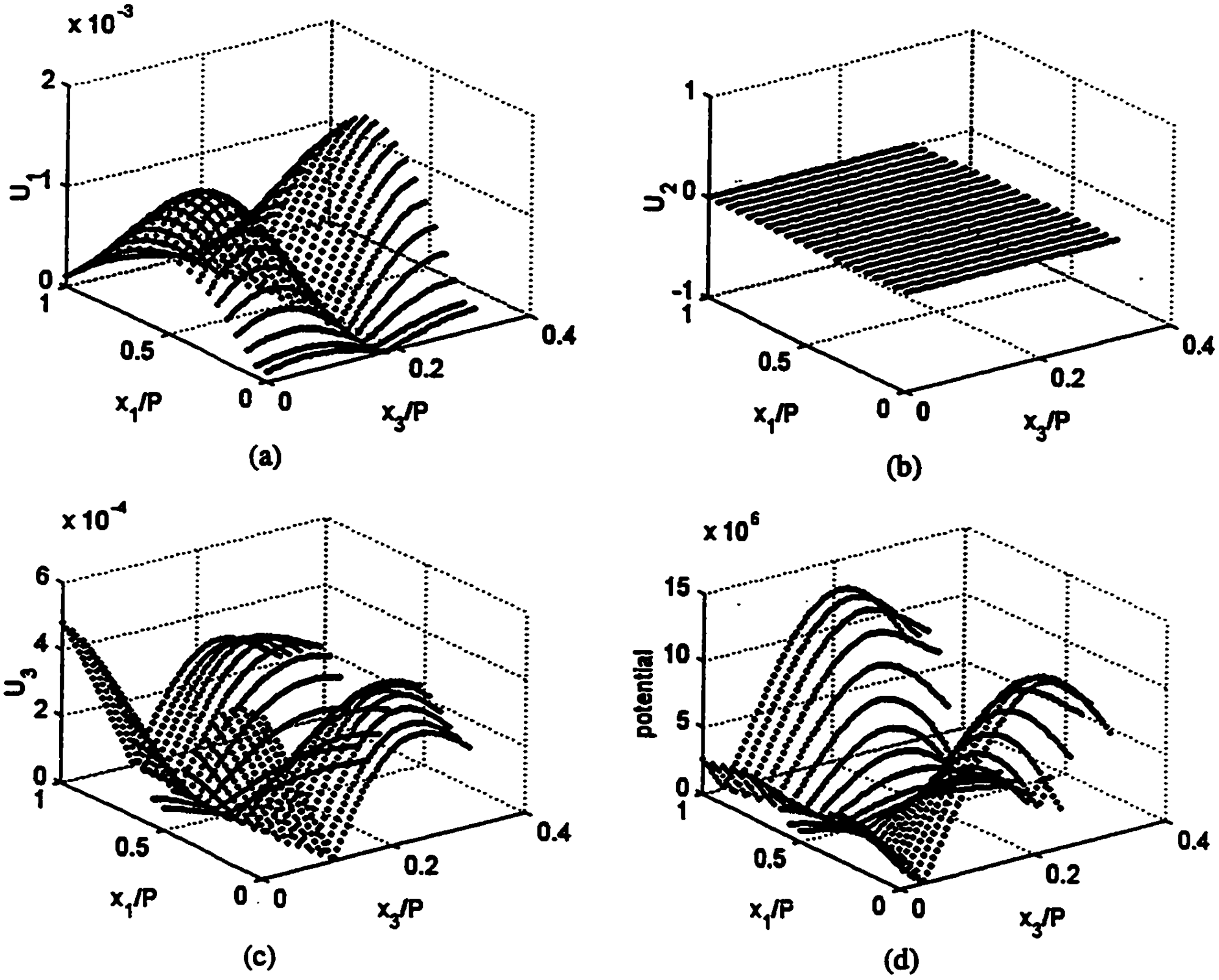

(a) (b) (c) (d)

Figure 3.19: Standing wave pattern of the second mode at the upper stopband edge for shorted gratings when $H_Z = P/\pi$ and $H_A = 0.005P$. (a)Displacement standing wave pattern in the x_1 direction. (b)Displacement standing wave pattern in the x_2 direction. (c)Displacement standing wave pattern in the x_3 direction. (d)Potential standing wave pattern. Vertical axes represent arbitrary units.

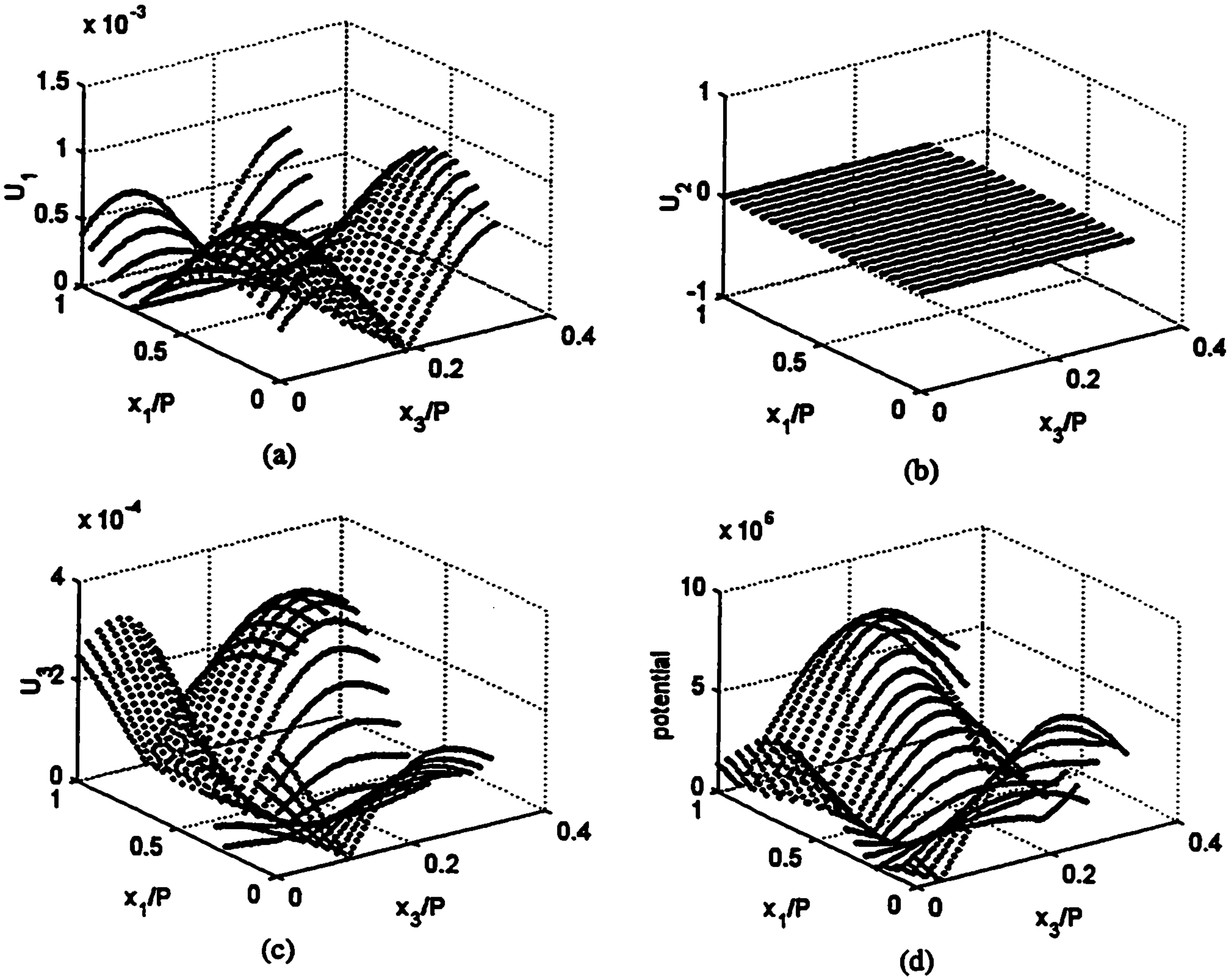

(a)

(b)

(c)

(d)

Figure 3.20: Standing wave pattern of the second mode at the stopband center for shorted gratings when $H_Z = P/\pi$ and $H_A = 0.005P$. (a)Displacement standing wave pattern in the x_1 direction. (b)Displacement standing wave pattern in the x_2 direction. (c)Displacement standing wave pattern in the x_3 direction. (d)Potential standing wave pattern. Vertical axes represent arbitrary units.

when $H_A = 0$.

For $H_A = 0.03P$, the standing wave patterns are totally different from that of the second mode for $H_A = 0.03P$. These patterns are shown in 3.23-3.25. Maximum points are located around $0.25P$, $0.75P$ and $0.5P$ for the lower stopband edge, the upper stopband edge and the stopband center, respectively.

These standing wave patterns will be used to determine the COM parameters later in this chapter.

3.3.3 Energy distribution

The time average of the energy density distributions can also be calculated from eqs. (3.51)-(3.53). Fig. 3.26 shows the time average of the energy distributions inside the ZnO layer, while the distributions for the diamond layer are shown in fig. 3.27, both for the lower stopband edge for $H_Z = P/\pi$. The thickness of Al is set at $H_A = 0.03P$ and the gratings are shorted. Figs. 3.28 and 3.29 show the corresponding energy distributions for the stopband center.

As stated above, the wave energy can be divided into two mechanical types and one electrical type in the quasi-static approximation (3.51)-(3.53). Without piezoelectricity, these three energy densities must be positive because they have quadratic forms. For piezoelectric substrate, however, strain energy density and electric stored energy density exchange part of their energies with each other, which may not always

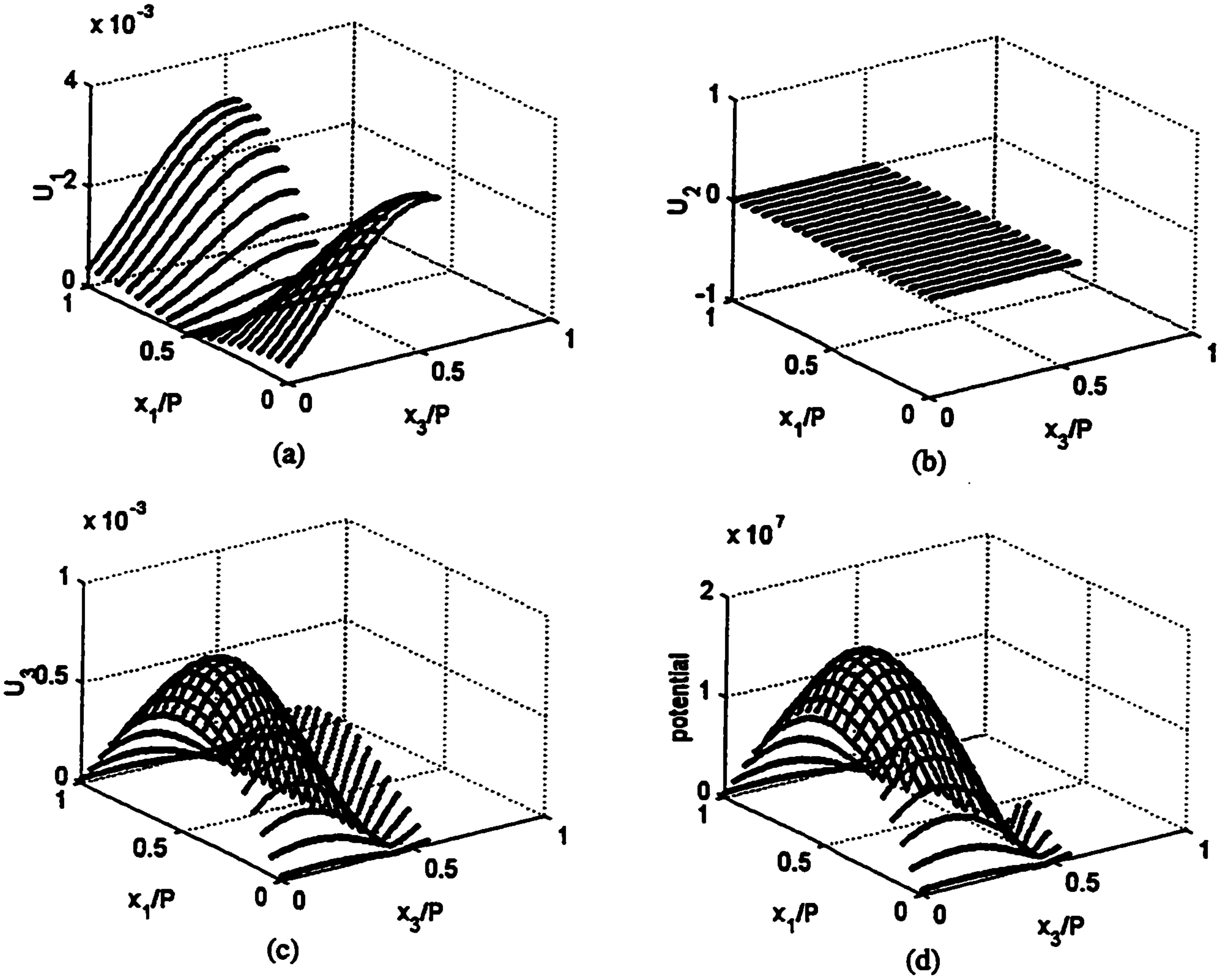

Figure 3.21: Standing wave pattern of the first Sezawa mode at the lower stopband edge for shorted gratings when $H_Z = 1.75P/\pi$ and $H_A = 0$. (a)Displacement standing wave pattern in the x_1 direction. (b)Displacement standing wave pattern in the x_2 direction. (c)Displacement standing wave pattern in the x_3 direction. (d)Potential standing wave pattern. Vertical axes represent arbitrary units.

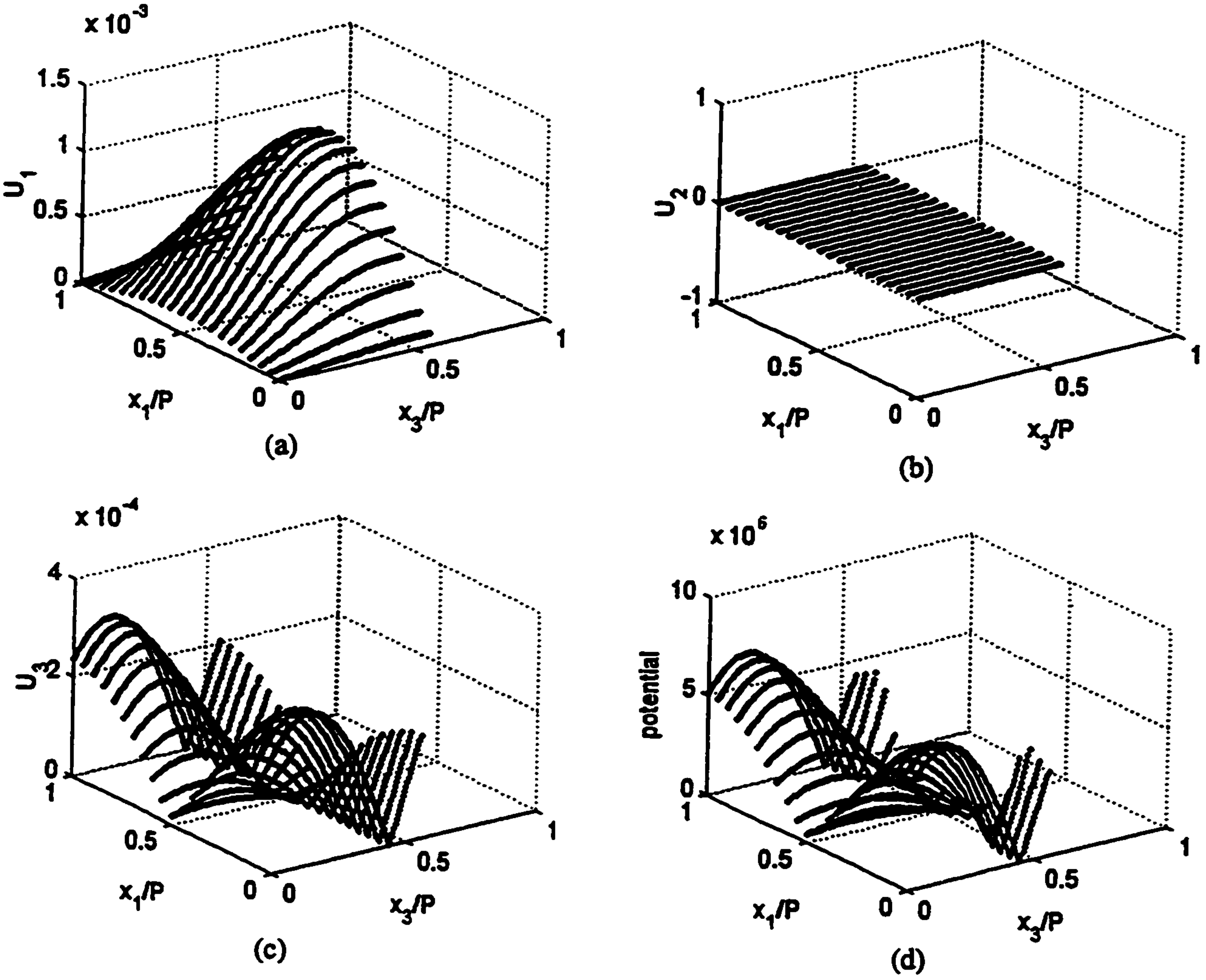

Figure 3.22: Standing wave pattern of the first Sezawa mode at the upper stopband edge for shorted gratings when $H_Z = 1.75P/\pi$ and $H_A = 0$. (a)Displacement standing wave pattern in the x_1 direction. (b)Displacement standing wave pattern in the x_2 direction. (c)Displacement standing wave pattern in the x_3 direction. (d)Potential standing wave pattern. Vertical axes represent arbitrary units.

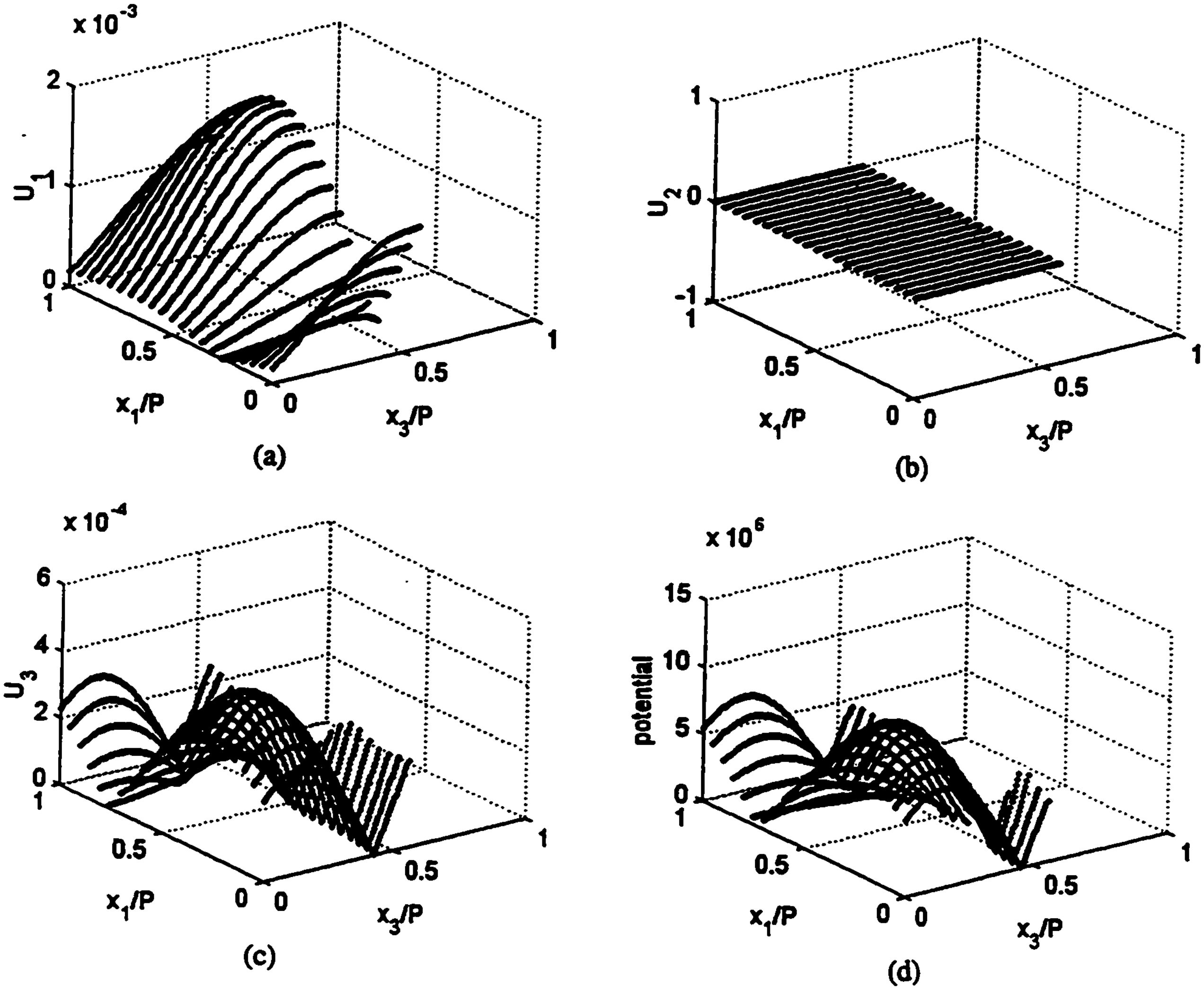

Figure 3.23: Standing wave pattern of the first Sezawa mode at the lower stopband edge for shorted gratings when $H_Z = 1.75P/\pi$ and $H_A = 0.03P$. (a)Displacement standing wave pattern in the x_1 direction. (b)Displacement standing wave pattern in the x_2 direction. (c)Displacement standing wave pattern in the x_3 direction. (d)Potential standing wave pattern. Vertical axes represent arbitrary units.

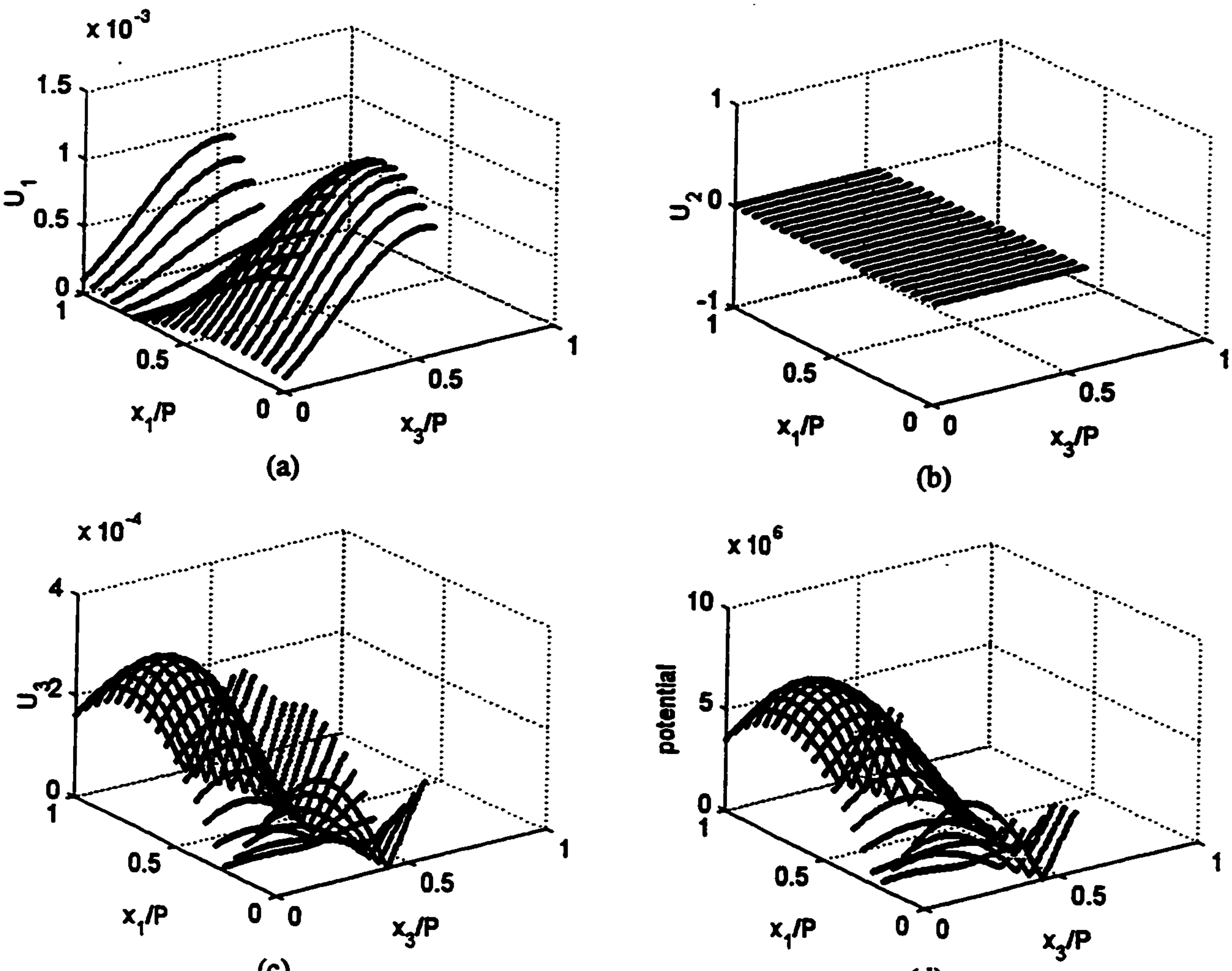

(a) (b) (c) (d)

Figure 3.24: Standing wave pattern of the first Sezawa mode at the upper stopband edge for shorted gratings when $H_Z = 1.75P/\pi$ and $H_A = 0.03P$. (a)Displacement standing wave pattern in the x_1 direction. (b)Displacement standing wave pattern in the x_2 direction. (c)Displacement standing wave pattern in the x_3 direction. (d)Potential standing wave pattern. Vertical axes represent arbitrary units.

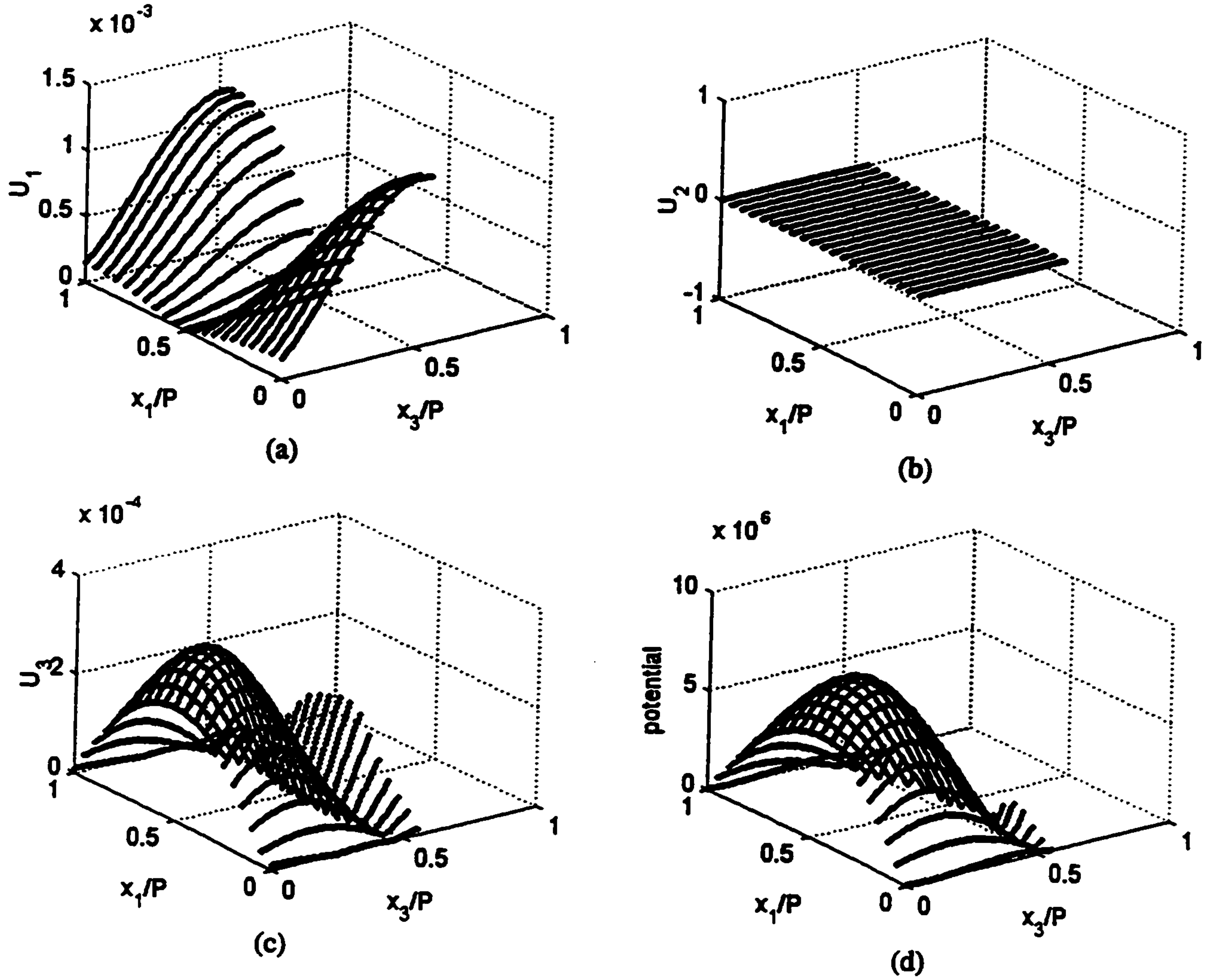

Figure 3.25: Standing wave pattern of the first Sezawa mode at the stopband center for shorted gratings when $H_Z = 1.75P/\pi$ and $H_A = 0.03P$. (a)Displacement standing wave pattern in the x_1 direction. (b)Displacement standing wave pattern in the x_2 direction. (c)Displacement standing wave pattern in the x_3 direction. (d)Potential standing wave pattern. Vertical axes represent arbitrary units.

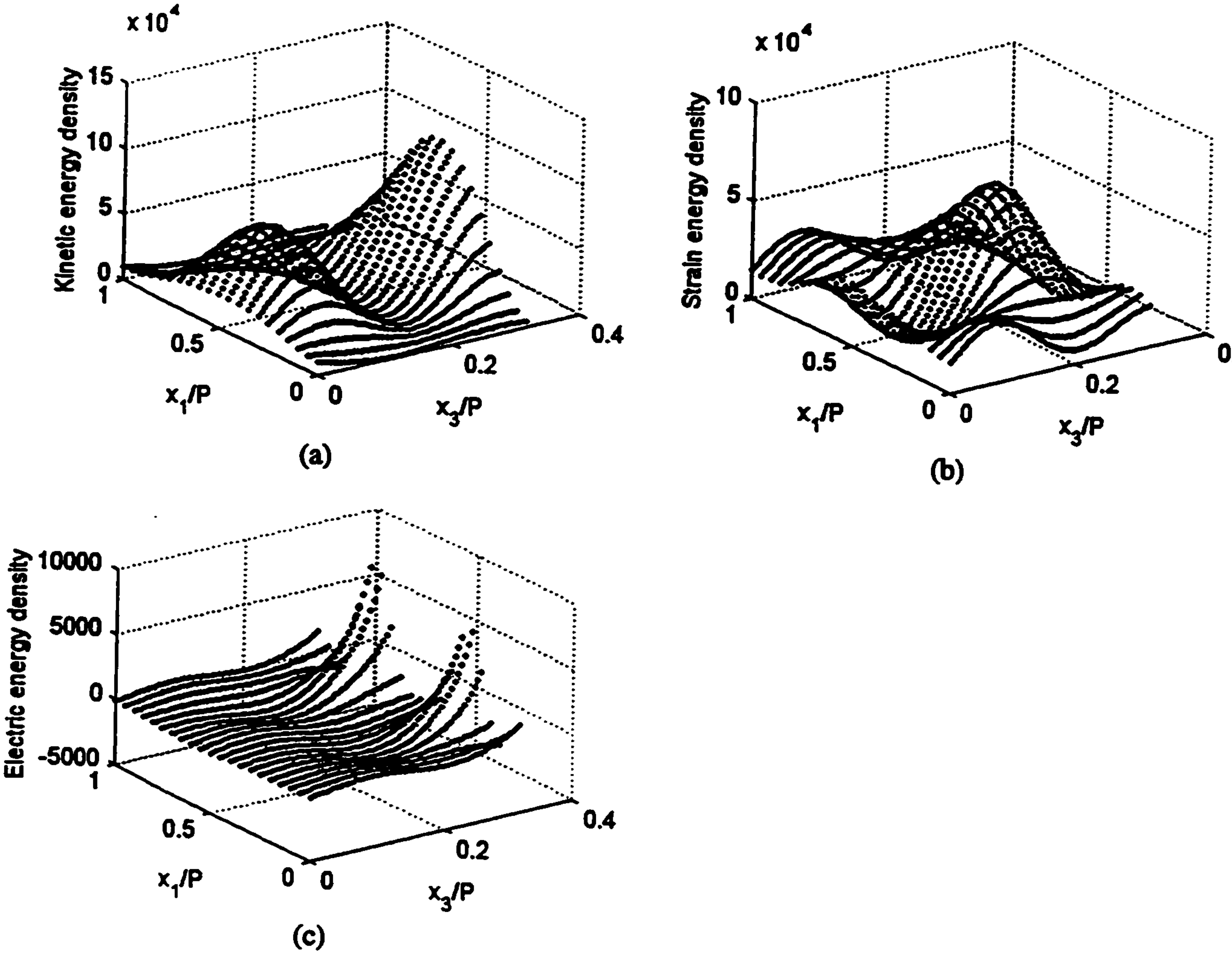

Figure 3.26: Energy density distribution of the second Sezawa mode inside ZnO layer at the lower stopband edge for shorted gratings when $H_Z = P/\pi$ and $H_A = 0.03P$. (a)Kinetic energy distribution. (b)Strain energy distribution. (c)Electric energy distribution. Vertical axes represent arbitrary units.

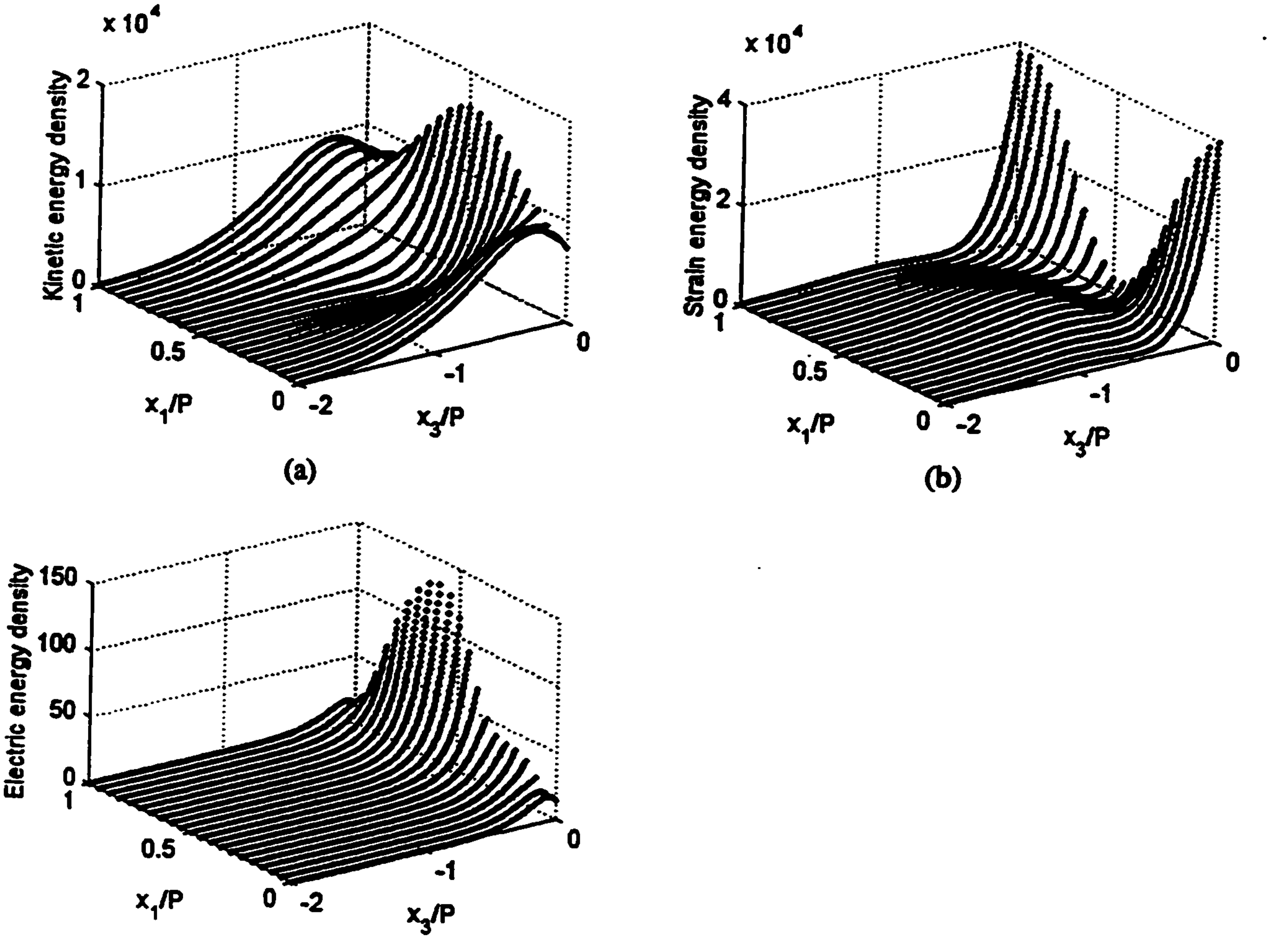

(a)

(b)

(c)

Figure 3.27: Energy density distribution of the second Sezawa mode inside diamond layer at the lower stopband edge for shorted gratings when $H_Z = P/\pi$ and $H_A = 0.03P$. (a)Kinetic energy distribution. (b)Strain energy distribution. (c)Electric energy distribution. Vertical axes represent arbitrary units.

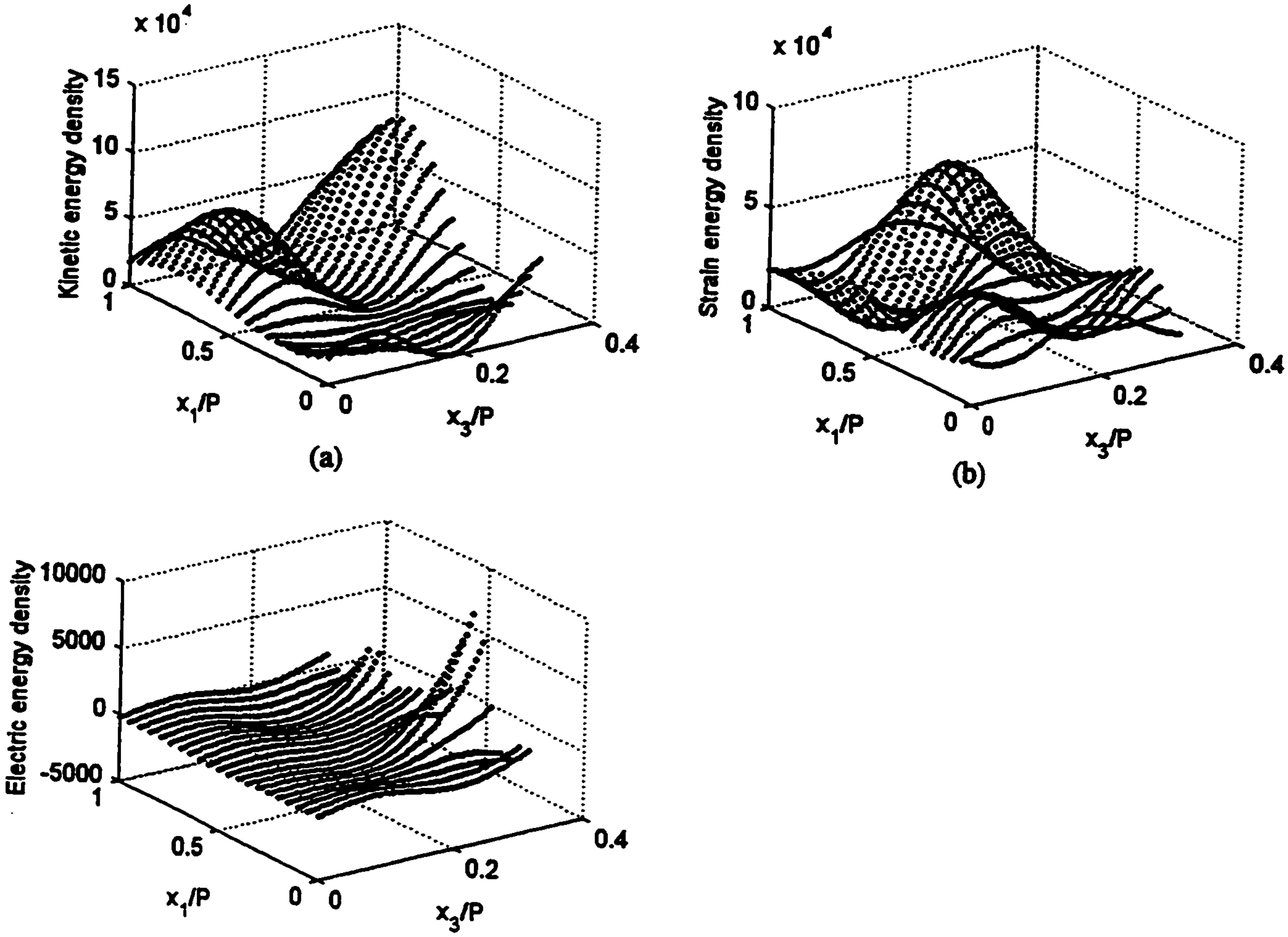

(a) (b) (c)

Figure 3.28: Energy density distribution of the second Sezawa mode inside ZnO layer at the stopband center for shorted gratings when $H_Z = P/\pi$ and $H_A = 0.03P$. (a)Kinetic energy distribution. (b)Strain energy distribution. (c)Electric energy distribution. Vertical axes represent arbitrary units.

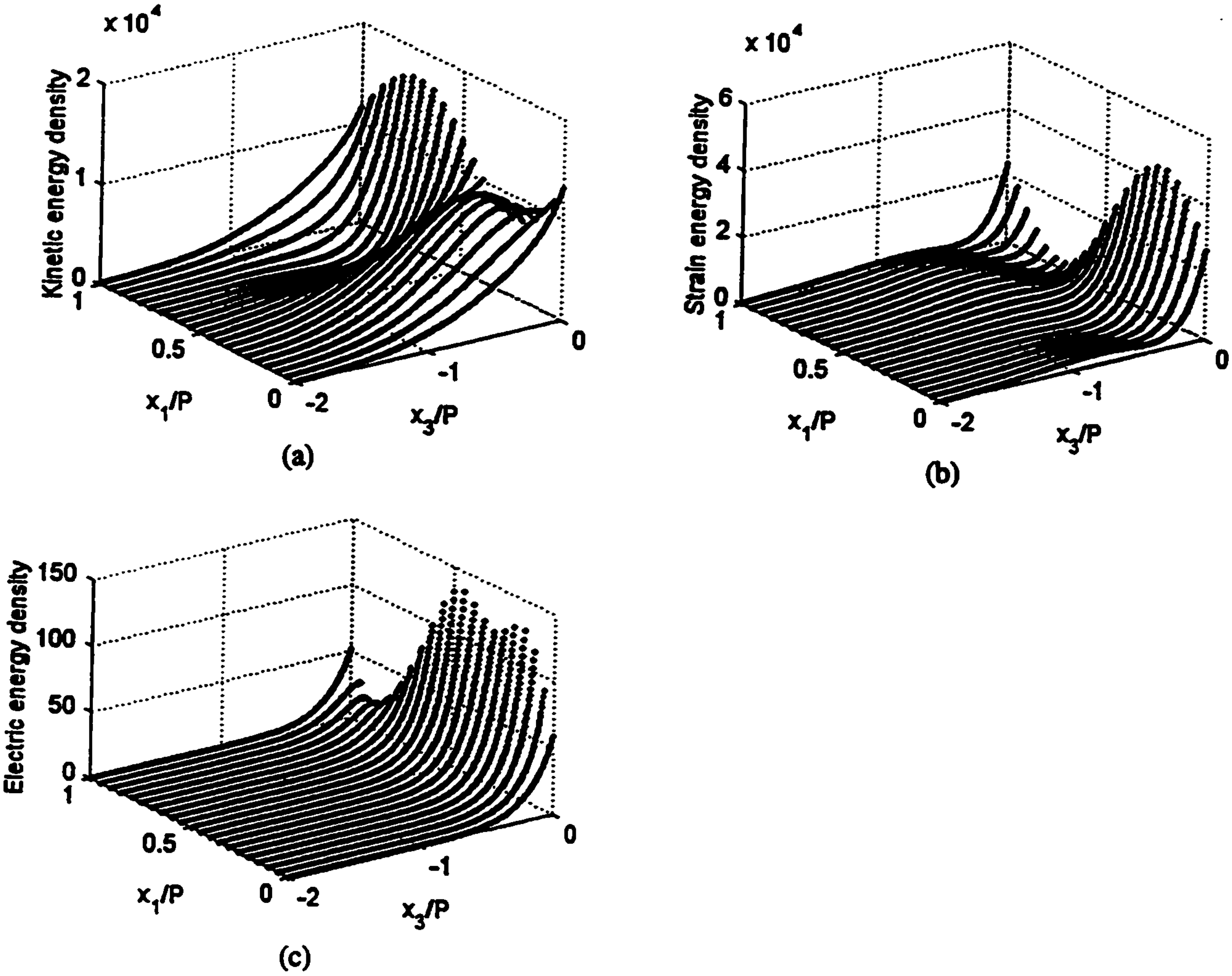

(a)

(b)

(c)

Figure 3.29: Energy density distribution of the second Sezawa mode inside diamond layer at the stopband center for shorted gratings when $H_Z = P/\pi$ and $H_A = 0.03P$. (a)Kinetic energy distribution. (b)Strain energy distribution. (c)Electric energy distribution. Vertical axes represent arbitrary units.

require a positive value of energy density for either type of these two energy densities, depending on the strength of the piezoelectric constant. This does not mean a negative energy density of the total energy density of the waves. This negative value can be seen in the electric energy at some points inside ZnO in figs. 3.26 and 3.28.

The kinetic energies inside ZnO have maximum values at the interface between Al and ZnO for both the lower stopband edge and the stopband center. On the other hand, the strain energies inside ZnO have maximum values inside the layer.

Inside the diamond, all the energies have their maxima at the ZnO/Diamond interface, and attenuate rapidly inside the diamond substrate.

Table 3.1 shows the time average of the total energy inside each layer for $H_Z = P/\pi$ and $H_Z = 1.5P/\pi$, with the total energy inside ZnO set to 100 for each condition. Here, the total energy means the sum of the energy density inside one period. This normalization is necessary because the amount of energy depends on the relative wave amplitude and on the grating period P, which doesn't allow us to calculate the absolute value of the energy. In the case of plain waves inside non-piezoelectric media, the time averages of the kinetic energy and of the strain energy must be the same at each point due to energy conservation inside media. However, in the case of Rayleigh waves propagating under grating structures inside isotropic media, these two energies are no longer identical at each point, because the acoustic Poynting vector has a spatial dependency, and only the integral of these two energies over the entire region can be assumed to be the same. For the generalized Rayleigh waves, this equality will be satisfied including the small amount of piezoelectric energy which is transferred from the strain energy to the electric stored energy. This agreement can be verified from the Table 3.1, which shows that the total kinetic energy and the total strain energy agree to within 1.2%. The difference can be attributed to the piezoelectrically transferred energy from the strain energy to the electric stored energy. It also shows that the total amount of energy inside the diamond is of the same order as that inside the ZnO layer when $H_Z = P/\pi$. At the ZnO/Diamond interface, the kinetic energy inside the diamond is larger than strain energy at the electrode midpoint, while the strain energy is larger at the center of the spacing. The total energy inside diamond when $H_Z = 1.5P/\pi$ is almost 30% of that inside ZnO, due to the increase of the ZnO thickness.

In Table 3.2, the total energies are shown for the first Sezawa mode when $H_Z = 1.75P/\pi$ and $H_A = 0.03P$. The total energy inside diamond is 7% of that inside the ZnO layer, because the thickness of ZnO is very large for this condition. The ratio of the energy inside diamond to that inside ZnO decreases almost linearly as the thickness of ZnO increases regardless of the mode. In spite of the small amount of energy inside diamond, the SAW velocity of around $5,900$ (m/s) is more than the twice of the slow shear wave for semi-infinite ZnO substrate.

Table 3.3 shows the amount of energy that exists within the specified depth in the diamond region at the lower stopband edge for shorted gratings. This table is for the second Sezawa wave when $H_Z = P/\pi$ and $H_A = 0.03P$. In Table 3.4, the

Table 3.1: Energy inside each layer at the lower stopband edge for shorted gratings normalized to the total wave energy inside ZnO. $H_A = 0.03P$.

	layer	kinetic	strain	electrical	total
$H_Z = P/\pi$	ZnO	49.17	50.65	0.18	100
	Diamond	34.66	36.31	0.06	71.02
	Al	4.40	0.51	–	–
	Total	88.23	87.47	–	–
$H_Z = 1.5P/\pi$	ZnO	52.39	47.54	0.07	100
	Diamond	12.34	18.65	0.02	31.01
	Al	2.63	0.39	–	–
	Total	67.36	66.58	–	–

Table 3.2: Energy inside each layer at the lower stopband edge for shorted gratings normalized to the total wave energy inside ZnO. $H_A = 0.03P$.

	layer	kinetic	strain	electrical	total
$H_Z = 1.75P/\pi$	ZnO	51.38	48.80	-0.18	100
	Diamond	1.28	5.66	0.24	7.18
	Al	1.31	0.73	–	–
	Total	53.97	55.15	–	–

energy inside the diamond region for the first mode is shown, with $H_Z = 1.75P/\pi$ and $H_A = 0.03P$. The total energy inside the diamond region is set to 100. We observe that over 99% of the total energy is concentrated within $2P$ (one wavelength) of the ZnO/Diamond interface for the both cases, and that there is essentially no energy below $4P$ (two wavelengths). This result confirms our assumption that the thickness of diamond is sufficient for the semi-infinite approximation.

3.3.4 COM Parameter Derivation

In Sec. 2.4 (p. 31), we have derived the relations between the dispersion diagrams and the COM parameters for the low loss approximation, eqs.(2.54),(2.55) and (2.69). The phase of the mutual coupling constant can be determined from the standing wave pattern at the ZnO surface, as explained in Sec. 2.4. The phase difference between the transduction coefficient and the mutual coupling coefficient is also estimated from (2.70).

Fig. 3.30 shows the computed COM parameters of the second Sezawa wave for $H_Z = P/\pi$ and $H_Z = 1.5P/\pi$, which are derived from the calculated dispersion diagrams by using the relations stated above. For both cases, the self-coupling coefficient κ_{11} and the mutual-coupling coefficient κ_{12} are a linear function of the Al thickness. κ_{11} is larger for $H_Z = P/\pi$. The positive κ_{12} becomes 0 around $H_A = 0.006P$ for $H_Z = P/\pi$ and around $H_A = 0.004P$ for $H_Z = 1.5P/\pi$, and becomes the negative value as the Al thickness increases, which means that the reflection center suddenly

Table 3.3: Energy inside the diamond up to specified depth for the second mode when $H_Z = P/\pi$ and $H_A = 0.03P$.

depth	kinetic	strain	electrical	total
0 to -0.5P	62.1	54.6	98.0	58.4
0 to -P	88.1	78.3	99.9	83.1
0 to -2P	99.5	98.6	100	99.1
0 to -3P	100	100	100	100
0 to -4P	100	100	100	100

Table 3.4: Energy inside the diamond up to specified depth for the first mode when $H_Z = 1.75P/\pi$ and $H_A = 0.03P$.

depth	kinetic	strain	electrical	total
0 to -0.5P	85.9	70.8	95.7	74.4
0 to -P	98.5	95.7	99.8	96.3
0 to -2P	100	100	100	100
0 to -3P	100	100	100	100
0 to -4P	100	100	100	100

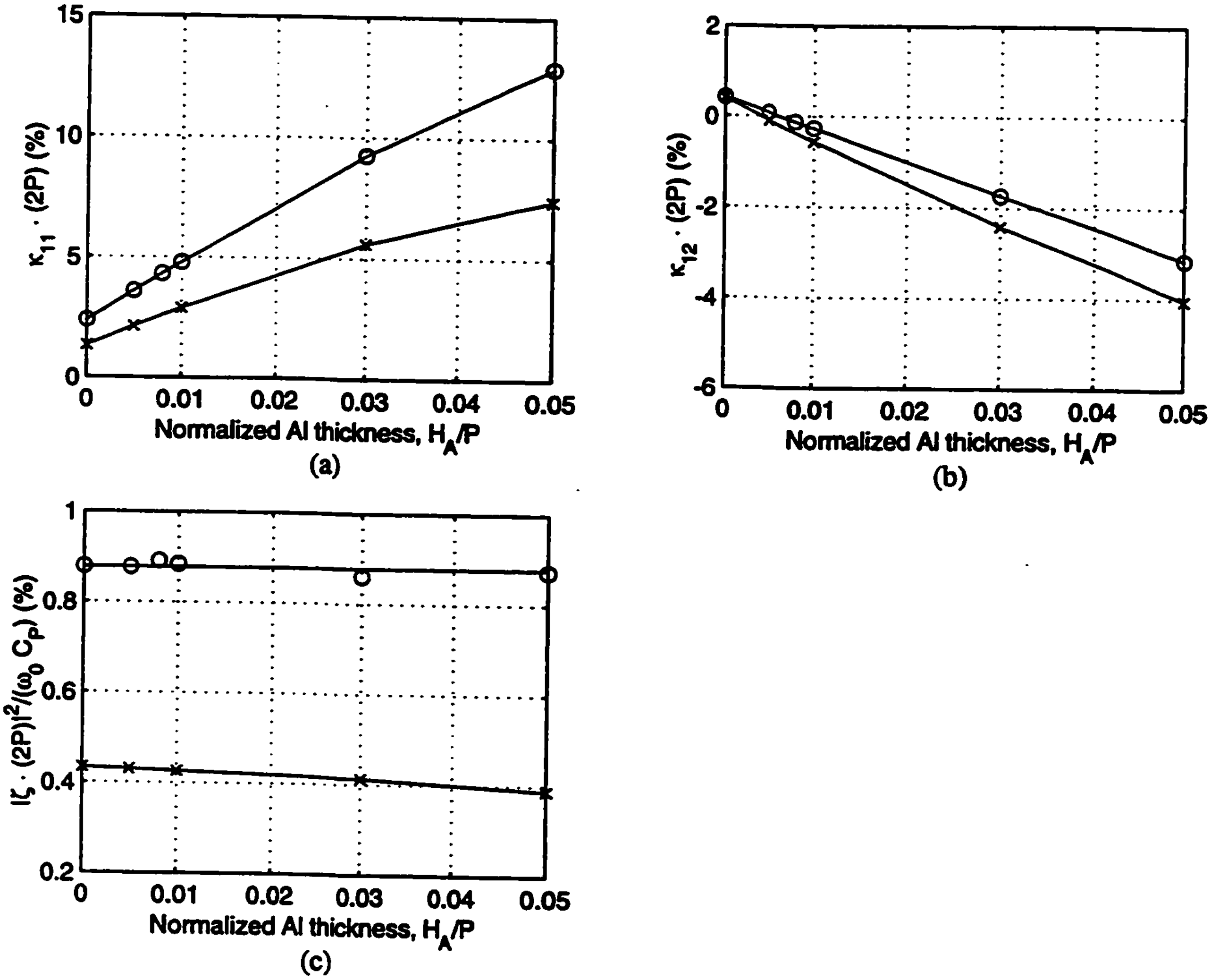

Figure 3.30: The coupling-of-modes (COM) parameters as a function of Al thickness for the second Seazwa mode when $H_Z = P/\pi$ ('o') and $H_Z = 1.5P/\pi$ ('×'). (a)Self coupling coefficient $\kappa_{11} \cdot (2P)$. (b)Mutual coupling coefficient $\kappa_{12} \cdot (2P)$. (c)Transduction coefficient $|\zeta \cdot (2P)|^2/(\omega_0 C_P)$.

change its position by $\lambda/4$. Zero κ_{12} would lead to no reflections for electrode of this thickness. The phase of the transduction ζ is always 0 in spite of the change of the Al thickness. ζ for $H_Z = P/\pi$ is insensitive to Al thickness, while it decreases linearly for $H_Z = 1.5P/\pi$. The magnitude of ζ is as twice for $H_Z = P/\pi$ as that for $H_Z = 1.5P/\pi$, which is consistent with the calculated result for the electro-mechanical coupling coefficient k^2 in [40].

COM parameters are also calculated as a function of the Al grating thickness for the first Sezawa mode when $H_Z = 1.75P/\pi$. For this case, none of the 4 stopband frequencies coincide for the thicker Al thickness, which indicates that the reflection and transduction centers are no longer identical. From the standing wave pattern, we can estimate that the phase of κ_{12} becomes $\pi/4$ when Al exceeds the thickness $H_A = 0.008P$. That is, κ_{12} changes from a positive real value to a positive pure imaginary value as the Al thickness increases. The phase of ζ remains constant, which results in a phase difference between κ_{12} and ζ of $\pi/4$ ($\phi - \psi = \pi/4$). For a structure with anisotropy either in the substrate or the electrode finger structure, this is a necessary and sufficient condition to single phase unidirectionality [38] and can be used for lowloss SAW filters such as single-phase unidirectional transducers (SPUDTs) [44], the floating electrode unidirectional transducers (FEUDTs) [45] [46] and natural SPUDTs (NSPUDTs) [47]. In this case, however, there is no origin of anisotropy in the structure and it is hardly possible to have a unidirectionality. Our calculated results show that the centers of κ_{12} and ζ for the positive x_1 travelling wave are shifted $\lambda/8$ and those of the negative travelling wave are shifted $-\lambda/8$, and eventually becomes bi-directional. This phenomenon is, however, very unusual and may have applications in new SAW filter structures.

In fig. 3.31, COM parameters are shown. The magnitudes of κ_{11} and κ_{12} change linearly with Al grating thickness, as did the values for the second mode. ζ decreases linearly.

3.4 Generation Problem

3.4.1 Space Harmonic Description

In the generation problem, a positive and a negative voltage is applied to the adjacent grating electrodes alternately. The period of this structure is now $\lambda = 2P$, as opposed to the period of the grating P for the eigenvalue problem described in Secs. 3.2 (p. 48) and 3.3 (p. 68). Fig. 3.32 shows the periodic Al grating structure on a ZnO/Diamond substrate, which will be considered in this section.

The displacements and the potential, U_i, must have the same periodicity, including the phase term, as the applied voltage. This requires

$$U_i(x_1 + \lambda) = U_i(x_1) \tag{3.55}$$

or

$$U_i(x_1 + P) = -U_i(x_1) \tag{3.56}$$

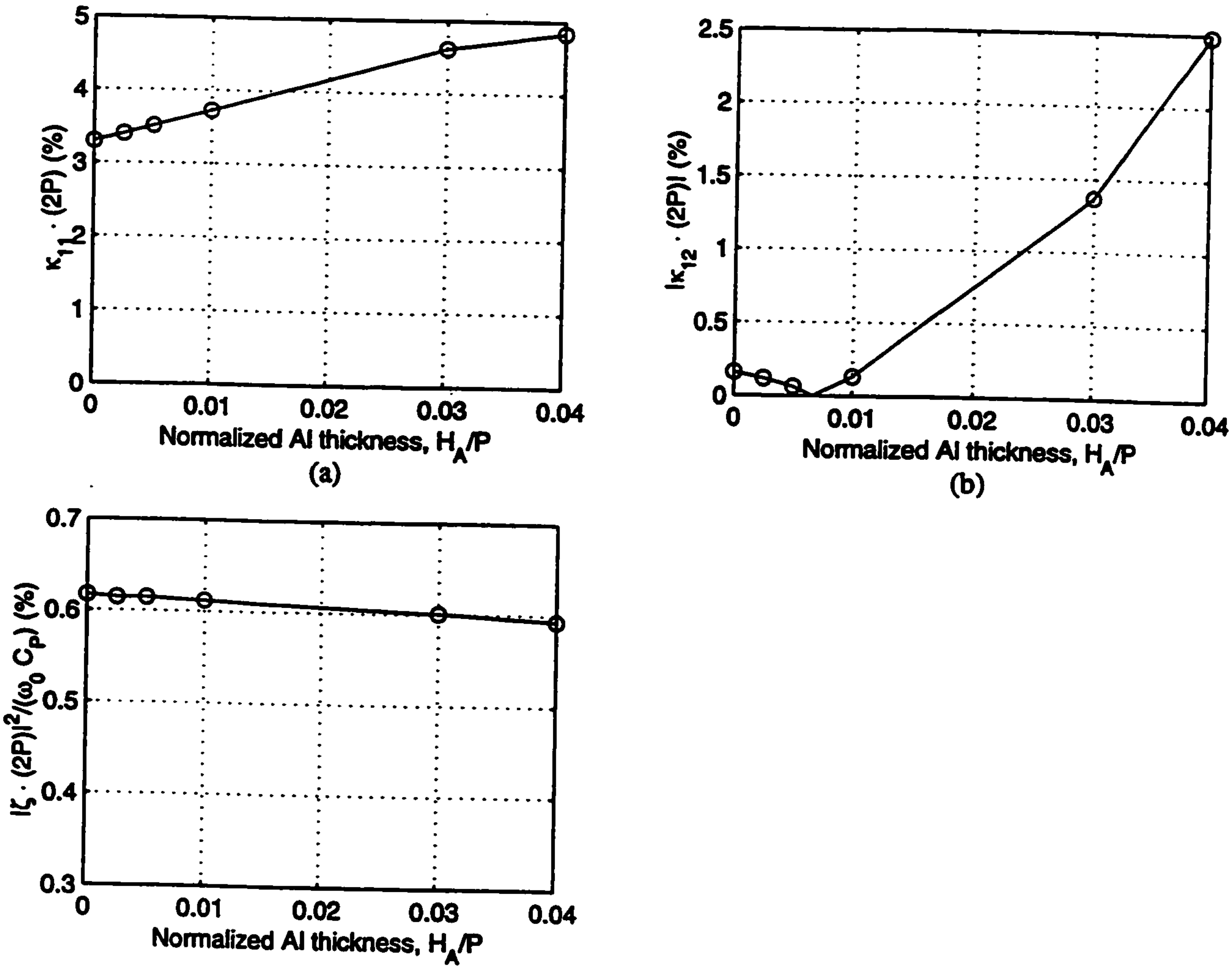

(a)

(b)

(c)

Figure 3.31: The coupling-of-modes (COM) parameters as a function of Al thickness for the first Sezawa mode when $H_Z = 1.75P/\pi$. (a)Self coupling coefficient $\kappa_{11} \cdot (2P)$. (b)Mutual coupling coefficient $\kappa_{12} \cdot (2P)$. (c)Transduction coefficient $|\zeta \cdot (2P)|^2/(\omega_0 C_P)$.

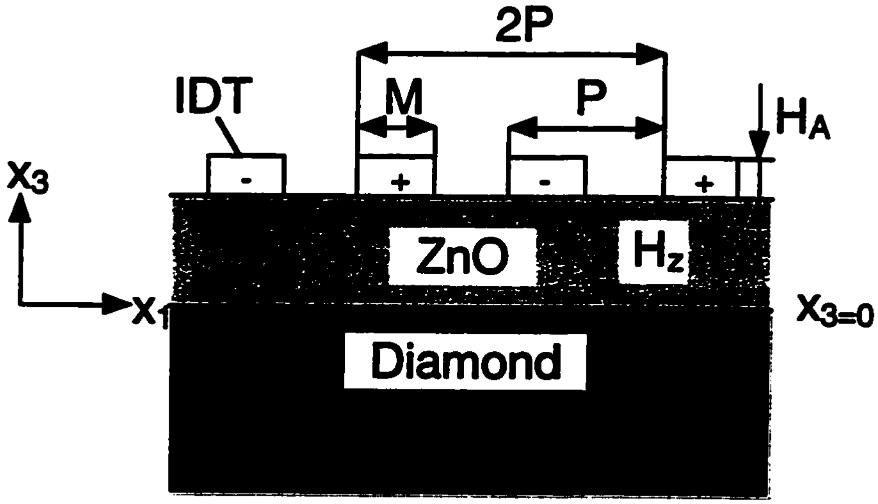

Figure 3.32: An infinite grating structure on ZnO/Diamond substrate. The positive and the negative voltages are applied to the adjacent grating electrodes alternately.

Under the condition (3.56), we can deal with this problem using a similar manner as used for the eigenvalue problem, which has a period P, not $2P$. From eqs.(3.1) and (3.3), the quantities U_i can be expanded by using space harmonics with the following wavenumbers

$$k_n = k_0 + \frac{2\pi}{P}n = \frac{\pi}{P} + \frac{2\pi}{P}n = \frac{\pi}{P}(1+2n) \qquad \text{(n:integer)} \tag{3.57}$$

where $k_0 = \pi/P$ is a constant value determined by the grating period, P, as opposed to the eigenvalue problem case in (3.3).

The resultant space harmonic expressions for the particle displacements U_i ($i = 1, 2, 3$) and the electric potential U_4 in each region are the same as in eqs.(3.8)-(3.11), except that we impose the normalized wavenumber $\gamma = 1$ for this case. We get

$$\text{diamond: } U_i^d = \sum_{m=-\infty}^{\infty} \sum_{n=1}^{4} A^{(m,n)} \beta_i^{(m,n)} e^{j\frac{\pi}{P}\left[\alpha^{(m,n)}x_3+(1+2m)x_1-f(2P)t\right]}$$

$$(i = 1, 2, 3, 4) \tag{3.58}$$

$$\text{ZnO: } U_i^z = \sum_{m=-\infty}^{\infty} \sum_{n=5}^{12} A^{(m,n)} \beta_i^{(m,n)} e^{j\frac{\pi}{P}\left[\alpha^{(m,n)}x_3+(1+2m)x_1-f(2P)t\right]}$$

$$(i = 1, 2, 3, 4) \tag{3.59}$$

$$\text{Al electrode: } U_k^m = \sum_{m=-\infty}^{\infty} \sum_{n=13}^{18} A^{(m,n)} \beta_k^{(m,n)} e^{j\frac{\pi}{P}\left[\alpha^{(m,n)}x_3+(1+2m)x_1-f(2P)t\right]}$$

$$(k = 1, 2, 3) \tag{3.60}$$

$$\text{free space: } U_4^f = \sum_{m=-\infty}^{\infty} A^{(m,19)} \beta_4^{(m,19)} e^{j\frac{\pi}{P}\left[\alpha^{(m,19)}x_3+(1+2m)x_1-f(2P)t\right]} \tag{3.61}$$

The decaying factors $\alpha^{(m,n)}$ and the relative magnitudes of the partial wave vector $\beta_k^{(m,n)}$ are determined by following the same procedures used in Sec. 3.2 (p. 48). The weighting factors $A^{(m,n)}$ are determined from the boundary conditions.

The expressions for the boundary conditions are identical to those for the eigenvalue problem, which will be repeated here. However, the potential on the grating is the external applied voltage in this case.

The mechanical boundary conditions are expressed as

$$\text{diamond} \ : \ P_i^d = P_i^z \ (\text{ on } \Gamma_2^{d[M]}) \ , (i = 1,2,3), \tag{3.62}$$

$$\text{ZnO} \ : \ U_i^z = U_i^d \ (\text{ on } \Gamma_1^{z[M]}) \ , (i = 1,2,3), \tag{3.63}$$

$$P_i^z = P_i^m \ (\text{ on } \Gamma_2^{z[M]}) \ , (i = 1,2,3), \tag{3.64}$$

$$\text{metal IDT} \ : \ U_i^m = U_i^z \ (\text{ on } \Gamma_1^{m[M]}) \ , (i = 1,2,3), \tag{3.65}$$

$$P_i^m = 0 \ (\text{ on } \Gamma_2^{m[M]}) \ , (i = 1,2,3), \tag{3.66}$$

The electrical boundary conditions are

$$\text{diamond} \ : \ P_4^d = P_4^z \ (\text{ on } \Gamma_2^{d[E]}) \ , \tag{3.67}$$

$$\text{ZnO} \ : \ U_4^z = U_4^d \ (\text{ on } \Gamma_1^{z[E]}) \ , \tag{3.68}$$

$$P_4^z = P_4^f \ (\text{ on } \Gamma_{2a}^{z[E]}) \ , \tag{3.69}$$

$$U_4^z = V_0 e^{-j2\pi f t} \ (\text{ on } \Gamma_{2b}^{z[E]}) \ , \tag{3.70}$$

$$\text{free space} \ : \ U_4^f = U_4^z \ (\text{ on } \Gamma_{1a}^{f[E]}) \ , \tag{3.71}$$

$$U_4^f = V_0 e^{-j2\pi f t} \ (\text{ on } \Gamma_{1b}^{f[E]}) \ , \tag{3.72}$$

where V_0 is the magnitude of the applied voltage on the metal gratings, $P_i (i = 1, 2, 3)$ are the stress components and P_4 is the electrical displacement as before. $P_i (i = 1, 2, 3, 4)$ for this generation problem can be obtained by setting $\gamma = 1$ in eqs.(3.26)-(3.31).

These boundary conditions are rewritten as boundary integrals, as was done in Subsec. 3.2.3.

$$\begin{aligned}
\text{diamond} \quad : \quad & \int_{\Gamma_2^{d[M]}} Re[(P_i^{z*} - P_i^{d*})\delta U_i^d] d\Gamma \\
& + \int_{\Gamma_2^{d[E]}} Re[(P_4^{z*} - P_4^{d*})\delta U_4^d] d\Gamma = 0 \qquad (3.73) \\
\text{ZnO} \quad : \quad & \int_{\Gamma_1^{z[M]}} Re[(U_i^z - U_i^d)\delta P_i^{z*}] d\Gamma + \int_{\Gamma_2^{z[M]}} Re[(P_i^{m*} - P_i^{z*})\delta U_i^z d\Gamma \\
& + \int_{\Gamma_1^{z[E]}} Re[(U_4^z - U_4^d)\delta P_4^{z*}] d\Gamma + \int_{\Gamma_{2a}^{z[E]}} Re[(P_4^{f*} - P_4^{z*})\delta U_4^z] d\Gamma \\
& + \int_{\Gamma_{2b}^{z[E]}} Re[(U_4^z - V_0 e^{-j2\pi ft})\delta P_4^{z*}] d\Gamma = 0 \qquad (3.74) \\
\text{metal IDT} \quad : \quad & \int_{\Gamma_1^{m[M]}} Re[(U_i^m - U_i^z)\delta P_i^{m*}] d\Gamma \\
& + \int_{\Gamma_2^{m[M]}} Re[(-P_i^{m*})\delta U_i^m] d\Gamma = 0 \qquad (3.75) \\
\text{free space} \quad : \quad & \int_{\Gamma_{1a}^{f[E]}} Re[(U_4^f - U_4^z)\delta P_4^{f*}] d\Gamma \\
& + \int_{\Gamma_{1b}^{f[E]}} Re[(U_4^f - V_0 e^{-j2\pi ft})\delta P_4^{f*}] d\Gamma = 0 \qquad (3.76)
\end{aligned}$$

where the asterisk (*) denotes the complex conjugate. δU_i and δP_i represent the virtual increments of U_i and P_i, respectively.

Following the same procedures as in Sec. 3.2 (p. 48), we get the following set of equations in terms of the real and the imaginary parts of the weighting factors

$A^{(m,n)}$ for a given applied voltage amplitude V_0,

$$F_R^{(m',n',)}(V_0, A^{(-\infty,1)}, \ldots, A^{(m,n)}, \ldots, A^{(\infty,19)}) = 0 \tag{3.77}$$

$$F_I^{(m',n',)}(V_0, A^{(-\infty,1)}, \ldots, A^{(m,n)}, \ldots, A^{(\infty,19)}) = 0 \tag{3.78}$$

where $m' = -\infty$ to ∞ and $n = 1$ to 19.

This set of equations, combined with two more equations given by the information about the applied voltage of the electrodes,

$$V_0 = Re(V_0) + jIm(V_0) \tag{3.79}$$

form the matrix equation,

$$\mathbf{C} \cdot \mathbf{Y} = \mathbf{b} \tag{3.80}$$

where each element of the rows above 2 of matrix **C** can be calculated from the set of equations (3.77) and (3.78). In terms of rows 1 and 2 of **C**, we have $\mathbf{C}(1,1) = 1$ and $\mathbf{C}(2,2) = 1$ and zeros elsewhere. The **Y** vector consists of the real and the imaginary parts of the applied voltage magnitude, V_0, and the unknowns, $A^{(m,n)}$,

$$\begin{aligned}\mathbf{Y} = {} & [Re(V_0), Im(V_0), Re(A^{(-\infty,1)}), Im(A^{(-\infty,1)}), \ldots, \\ & Re(A^{(m,n)}), Im(A^{(m,n)}), \ldots, \\ & Re(A^{(\infty,19)}), Im(A^{(\infty,19)})]^T,\end{aligned} \tag{3.81}$$

The vector **b** is given by

$$\mathbf{b} = [Re(V_0), Im(V_0), 0, \ldots, 0]^T \tag{3.82}$$

From eq.(3.80), we can calculate the weighting factors, $A^{(m,n)}$ for the specific applied voltage and frequency.

Once the weighting factors, $A^{(m,n)}$, are given, we can easily calculate the charge density, P_4. The total charge on one electrode, Q^m, is determined by integrating the charge density along the electrode surface, Γ.

$$Q^m = \oint_{electrode} P_4 d\Gamma = Q_r + jQ_i \tag{3.83}$$

If we denote the real and the imaginary parts of the total charge, Q^m, as Q_r and Q_i, respectively, they have the following relations between the real and the imaginary parts of the admittance, $Y_r(f)$ and $Y_i(f)$ $(Y(f) = Y_r(f) + jY_i(f))$

$$\begin{aligned} Q_r &= \frac{Y_i(f)}{2\pi f}(2V_0) = \frac{Y_i(f)}{\pi f}V_0 && (3.84) \\ Q_i &= \frac{Y_r(f)}{2\pi f}(2V_0) = \frac{Y_r(f)}{\pi f}V_0 && (3.85) \end{aligned}$$

where the expressions for $Y_r(f)$ and $Y_i(f)$ were previously given as (2.92) and (2.93) by using the COM equations.

From the equivalent circuit model [48] [5], one electrode pair can also be represented by the equivalent circuit shown in fig. 3.33, where the admittance

$$\begin{aligned} Y_r(f) &= G_a(f) = \frac{\lambda_0 4\zeta^2 \alpha_L}{\left\{\frac{2\pi}{\lambda_0}\left(\frac{f}{f_0} - 1\right) + \kappa_{11} + \kappa_{12}\right\}^2 + \alpha_L^2} && (3.86) \\ Y_i(f) &= 2\pi f C_P + B_a(f) \\ &= 2\pi f C_P - \frac{\lambda_0 4\zeta^2 \left\{\frac{2\pi}{\lambda_0}\left(\frac{f}{f_0} - 1\right) + \kappa_{11} + \kappa_{12}\right\}}{\left\{\frac{2\pi}{\lambda_0}\left(\frac{f}{f_0} - 1\right) + \kappa_{11} + \kappa_{12}\right\}^2 + \alpha_L^2} && (3.87) \end{aligned}$$

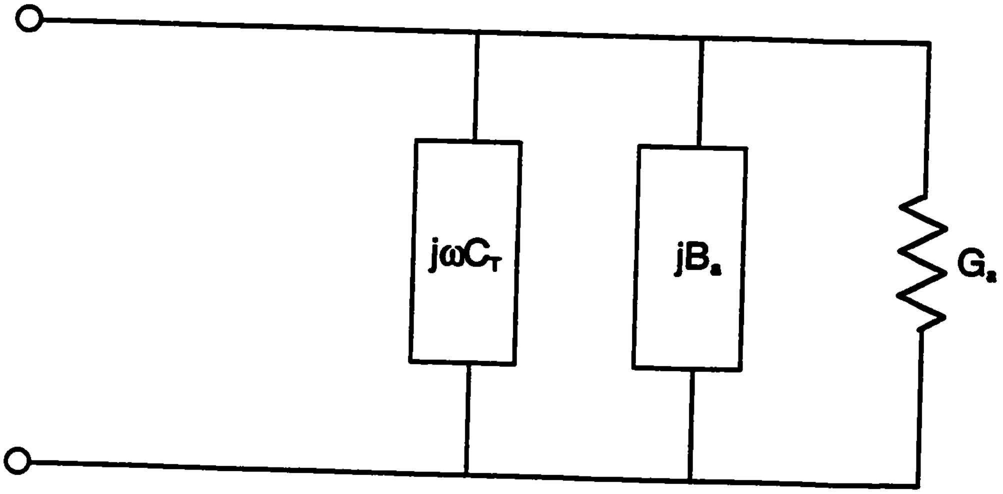

Figure 3.33: The equivalent circuit for one electrode pair.

G_a and B_a are frequency dependent conductance and susceptance, which are attributed to the generation of SAW by the applied voltage. C_P is a capacitance for one electrode pair with no frequency dependency.

3.4.2 The Procedure for Simulation

The admittance curve as a function of the frequency is obtained by way of the following procedure. At first, the normalized frequency $(f \cdot 2P)$ is set. $\alpha^{(m,n)}$ and $\beta_i^{(m,n)}$ are calculated for each space harmonic and for the each partial wave inside every layer. The boundary condition integrals are calculated and lead to a set of equations in terms of the real and the imaginary parts of the weighting factors and the applied voltage amplitude. The coefficient matrix, **C**, is set up. For the given applied voltage, the weighting factors, $A^{(m,n)}$ are calculated from (3.80). Using these calculated weighting factors, the total charge on an electrode is evaluated, which leads to the determination of the admittance (3.84) (3.85) for that frequency.

Fig. 3.34 shows a flowchart of a computer program for the calculation of the admittance curve as a function of the frequency.

In this procedure, the two dimensional optimization in terms of the complex wavenumber is not necessary, as was the case when getting the dispersion diagram for the eigenvalue problem in Sec. 3.2. This will significantly reduces the computational effort.

In the calculations, we truncate the number of space harmonics m to some

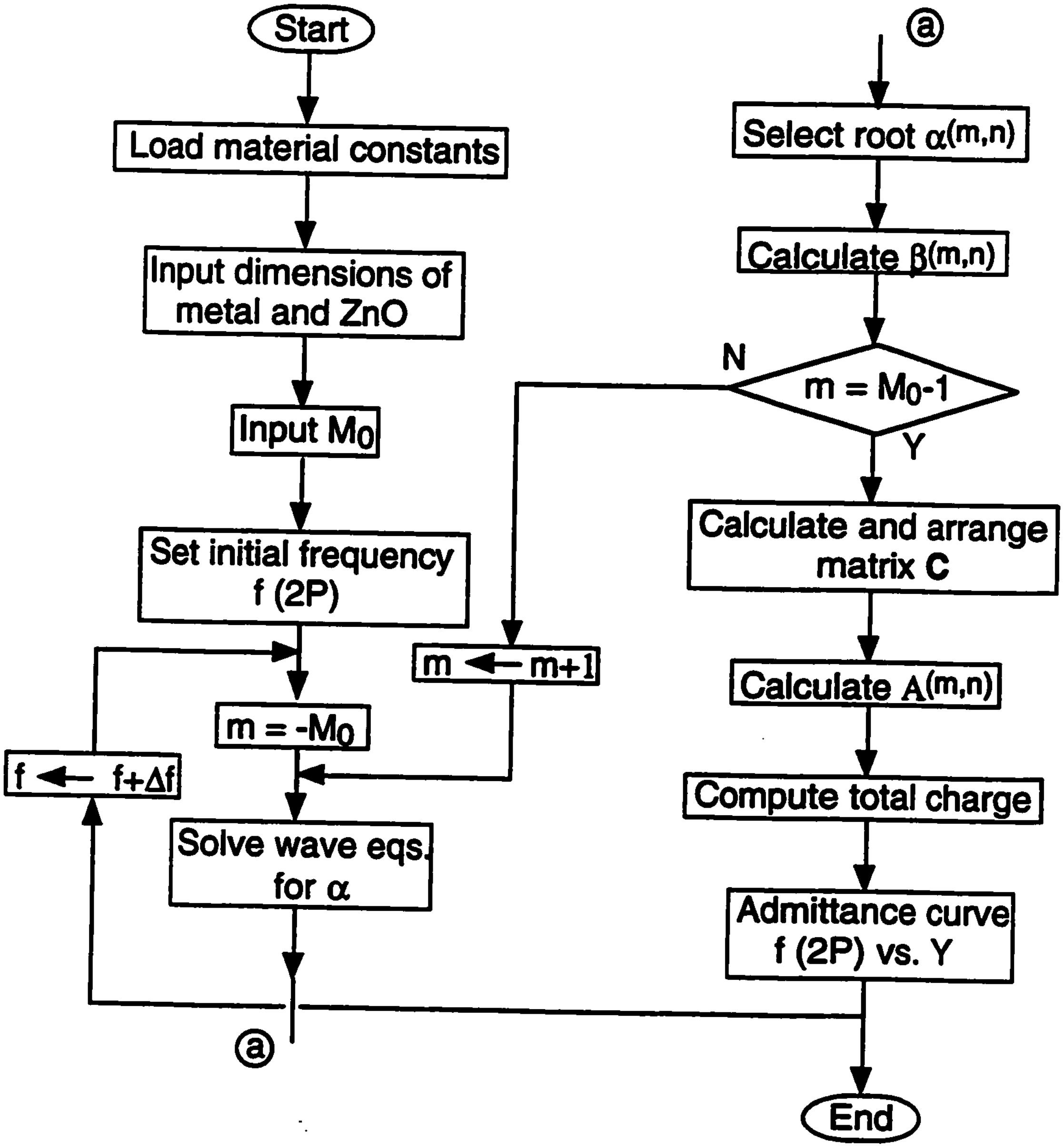

Figure 3.34: A flowchart of our calculation procedure.

specific value $2M_0$. In this case, the space harmonics ranges from $m = -M_0$ to $m = M_0 - 1$. The size of the resultant matrix **C** is $(76M_0 + 2) \times (76M_0 + 2)$. The following calculation uses $2M_0 = 40$. The width of the grating is set to $M = 0.5P$.

3.5 Results and Discussion for the Generation Problem

Fig. 3.35 shows the real part of the calculated charge for an Al/ZnO/Diamond structure when $H_Z = P/\pi$ and $H_A = 0.005$, with $2M_0 = 40$. From this figure, we see that there are multiple SAW excitations which correspond to a series of Sezawa modes. The wave around $f \cdot 2P = 6,500$ (m/s) corresponds to the 0th order Sezawa wave, that around $f \cdot 2P = 7,280$ (m/s) to the 1st order Sezawa wave and the 2nd order Sezawa wave appears around $f \cdot 2P = 11,550$ (m/s). The height and the width of the resonant structure of each mode will depend on the strength of the transduction and the propagation loss α_L introduced by numerical errors due to the truncation of the number of space harmonics.

From eqs.(3.84) and (3.87), the static capacitance can be evaluated from the real part of the total charge at the frequency where there is no influence due to SAW excitation. Therefore, we can estimate the capacitance from the calculated real charge by interpolation at $f \cdot 2P = 0$. The total real charge per unit length in the x_2 direction for $H_Z = P/\pi$ and $H_A = 0.005P$ is $1.75 \times 10^{-10} (C/m)$ when the applied

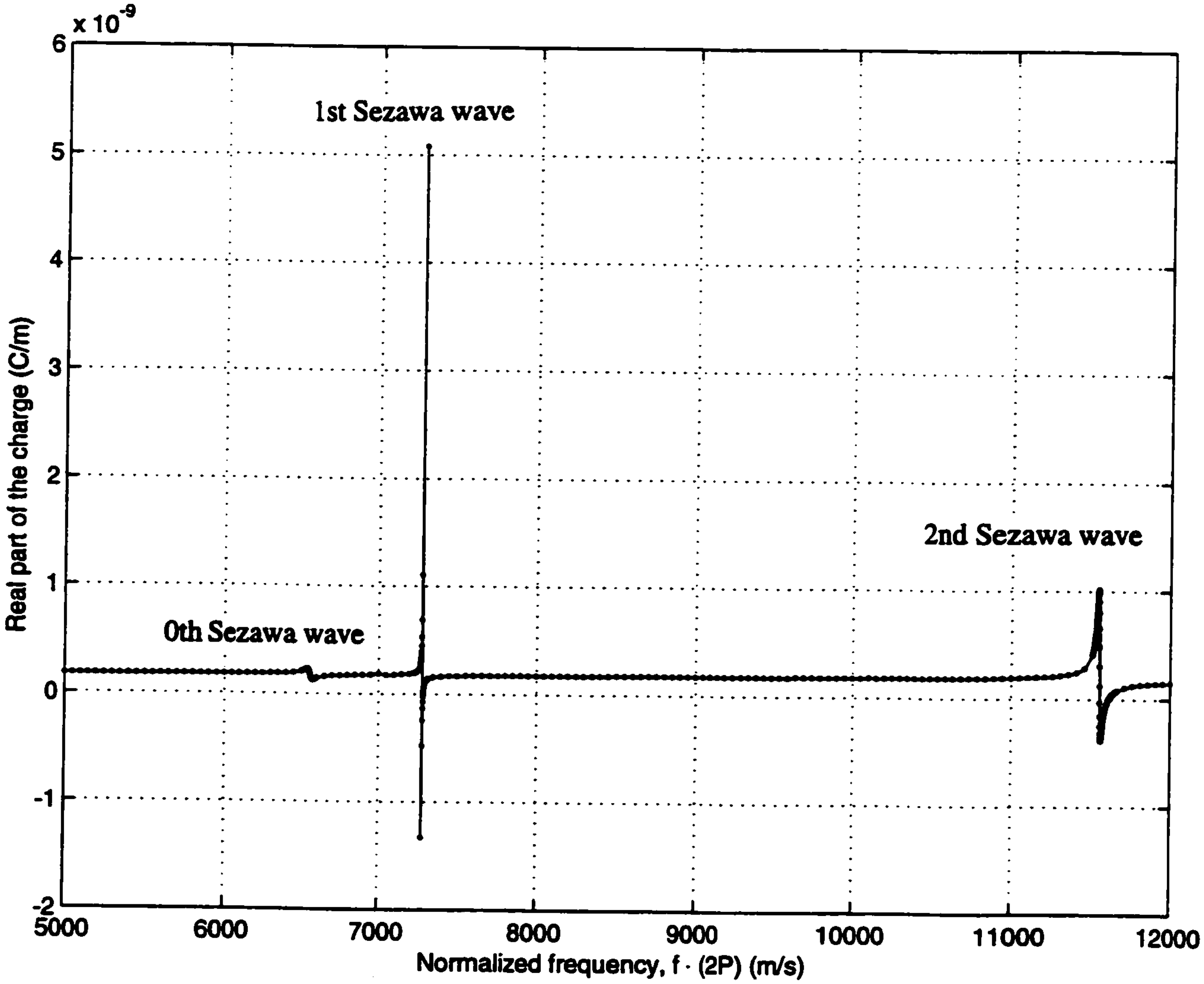

Figure 3.35: The real part of the total charge as a function of the normalized frequency when $H_Z = P/\pi$ and $H_A = 0.005P$.

voltage amplitude $V_0 = 1(V)$. Then, the calculated capacitance for one electrode pair with unit length in the x_2 direction is estimated to be $87.5(pF/m)$ when $H_Z = P/\pi$ and $H_A = 0.005P$.

Fig. 3.36 shows the static capacitance for one electrode pair per unit length in the x_2 direction as a function of Al grating thickness when $H_Z = P/\pi$, $H_Z = 1.5P/\pi$ and $H_Z = 1.75P/\pi$. The static capacitance of one electrode pair increases as the ZnO thickness increases and it is also a linear function of the Al thickness.

In fig. 3.37, the admittance curves for the second mode when $H_Z = P/\pi$ and $H_A = 0.005P$ are shown. There is an expected resonant shape for the susceptance, which consists of the static capacitance and the remaining component due to the excitation of the SAW. For the real part, the conductance should have a sharp peak corresponding to the SAW generation [5]. The calculated conductance (the imaginary charge), however, becomes zero everywhere, which leads to no energy dissipation corresponding to the generation of the SAW. Zero imaginary charge (zero conductance) comes from the fact that the contribution from mth and $-m$th space harmonics are complex conjugates of each other regardless of the frequency. And the total imaginary charge cancels out at every frequency. This complex conjugate nature originates in the fact that we are dealing with an infinite structure and there is no change in the positive and the negative travelling waves in the x_1 direction, as far as they have the same magnitudes of the wavenumber.

Physically, this situation can be interpreted as follows. At the SAW excitation

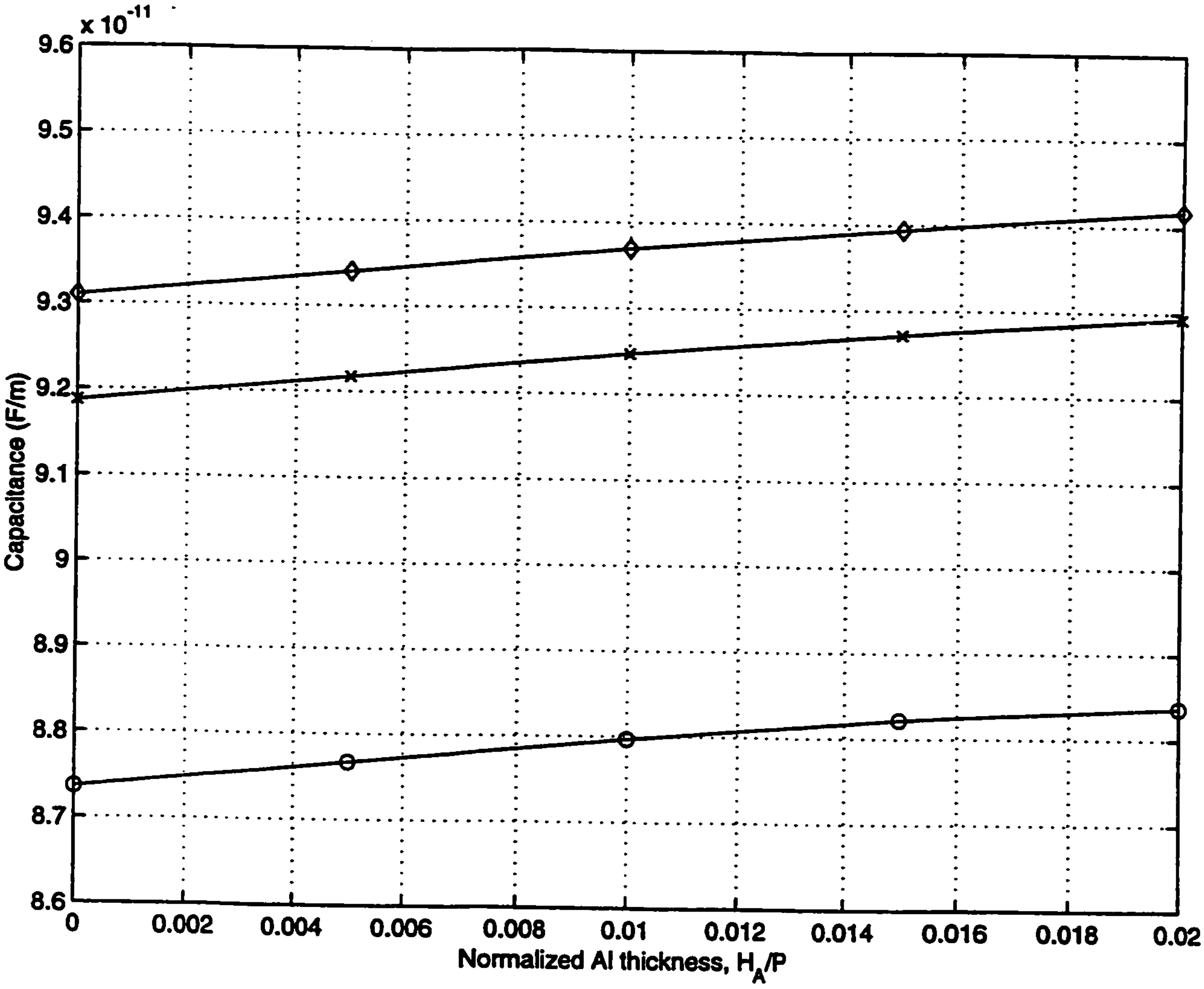

Figure 3.36: The static capacitance for one electrode pair per unit length when $H_Z = P/\pi$ ('o'), $H_Z = 1.5P/\pi$ ('×') and $H_Z = 1.75P/\pi$ ('◇').

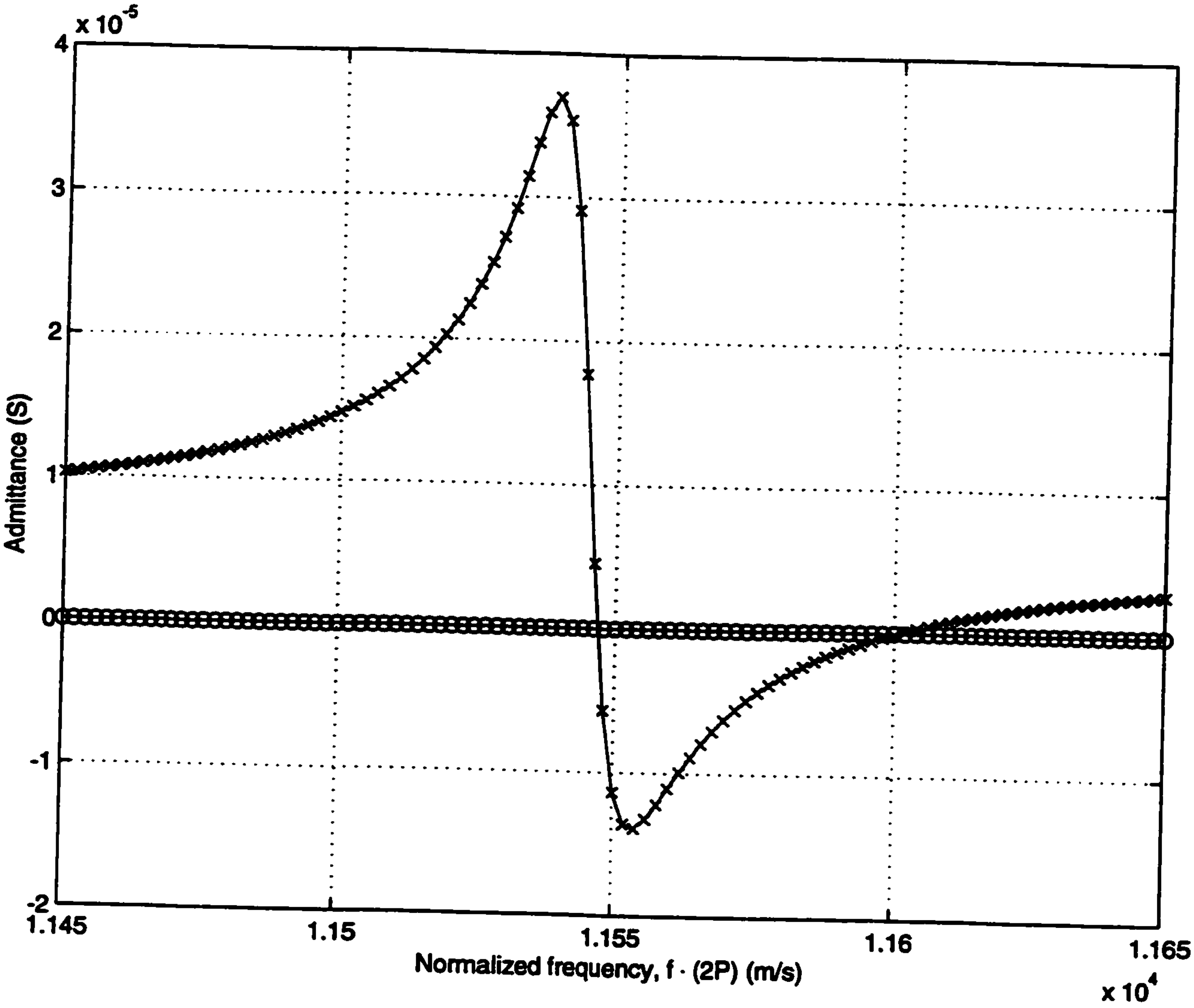

Figure 3.37: The admittance curves for the second Sezawa mode when $H_Z = P/\pi$ and $H_A = 0.005P$. Susceptance '×' and conductance 'o'.

frequency, the wave becomes a standing wave, because the wave travelling to the right and the wave travelling to the left are identical. Therefore, the amount of the energy emanating from or entering one period of the structure must be same due to the symmetry of the structure. Therefore, there is no net electrical energy dissipation attributed to the excitation of the SAW. In the real situation, however, the structure is not infinite and the energy gets converted when the SAW is excited, which leads to the sharp conductance peak at the specific frequency of the SAW generation.

By way of trial, "the conductance" is calculated by summing only the contributions from the space harmonics with the positive wavenumber, which is shown in fig. 3.38. this figure shows the sharp peak, and the result is due to the SAW generation. The magnitude, however, is more than 2 order less than expected. As a result, we have to conclude that the conductance can not be directly calculated from a SHM treatment based on the Floquet's theorem.

The relation between the conductance and the susceptance around the SAW generation frequency is known to be a Hilbert transform [5]. If the conductance is estimated by performing a Hilbert transform on the calculated susceptance, then the result shown in fig. 3.39 is obtained.

Fig. 3.40 shows the displacement distribution for the second Sezawa mode when the applied voltage magnitude is $V_0 = 1(V)$ at the resonant frequency. This figure is for $H_Z = P/\pi$ and $H_Z = 0.005P$ and at $t = 0$ in the expressions (3.58)-(3.61). At this frequency, displacements and the potential become standing waves and the

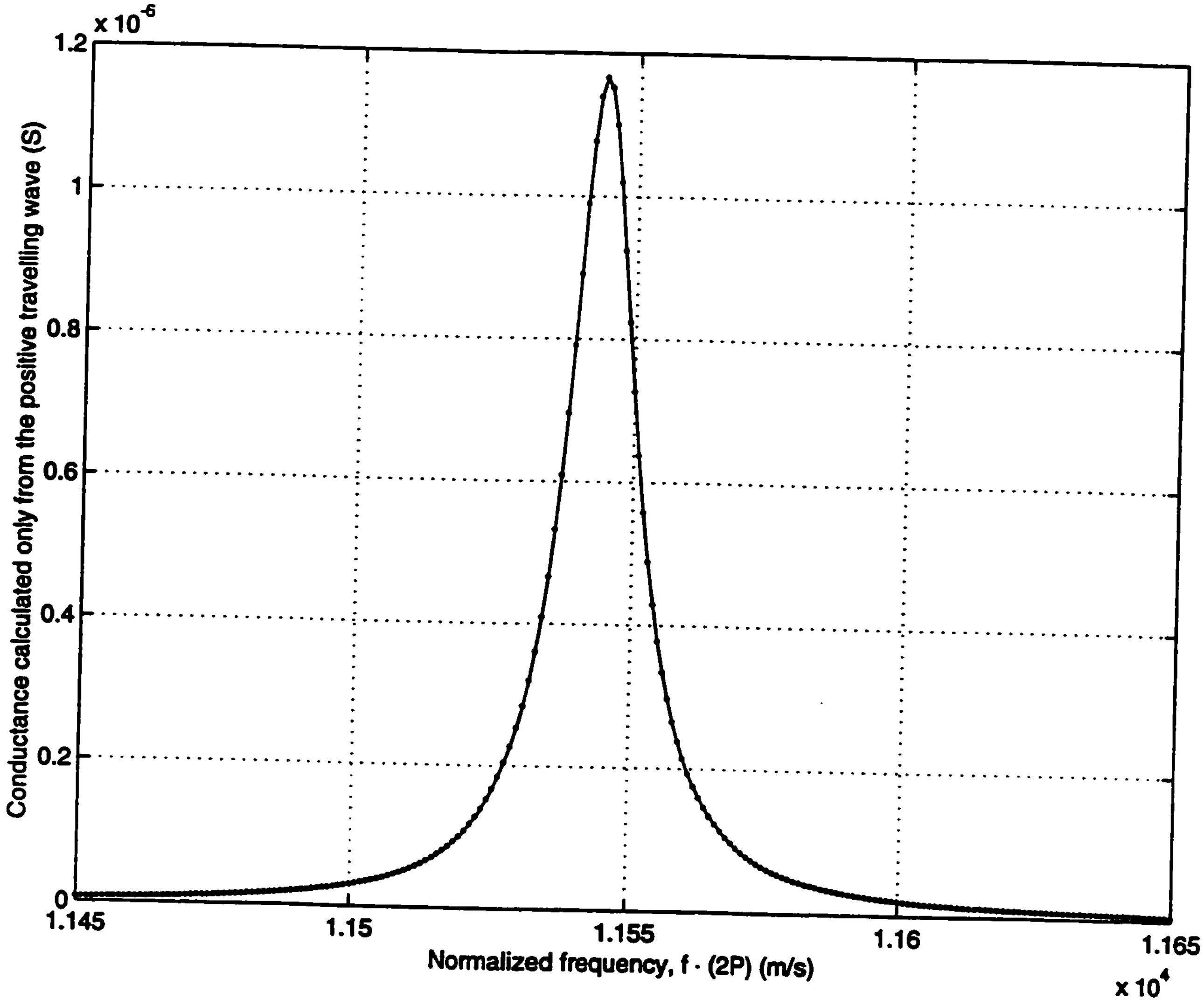

Figure 3.38: The calculated conductance curves for the second Sezawa mode when $H_Z = P/\pi$ and $H_A = 0.005P$ where only the contributions from the positive travelling waves are summed up.

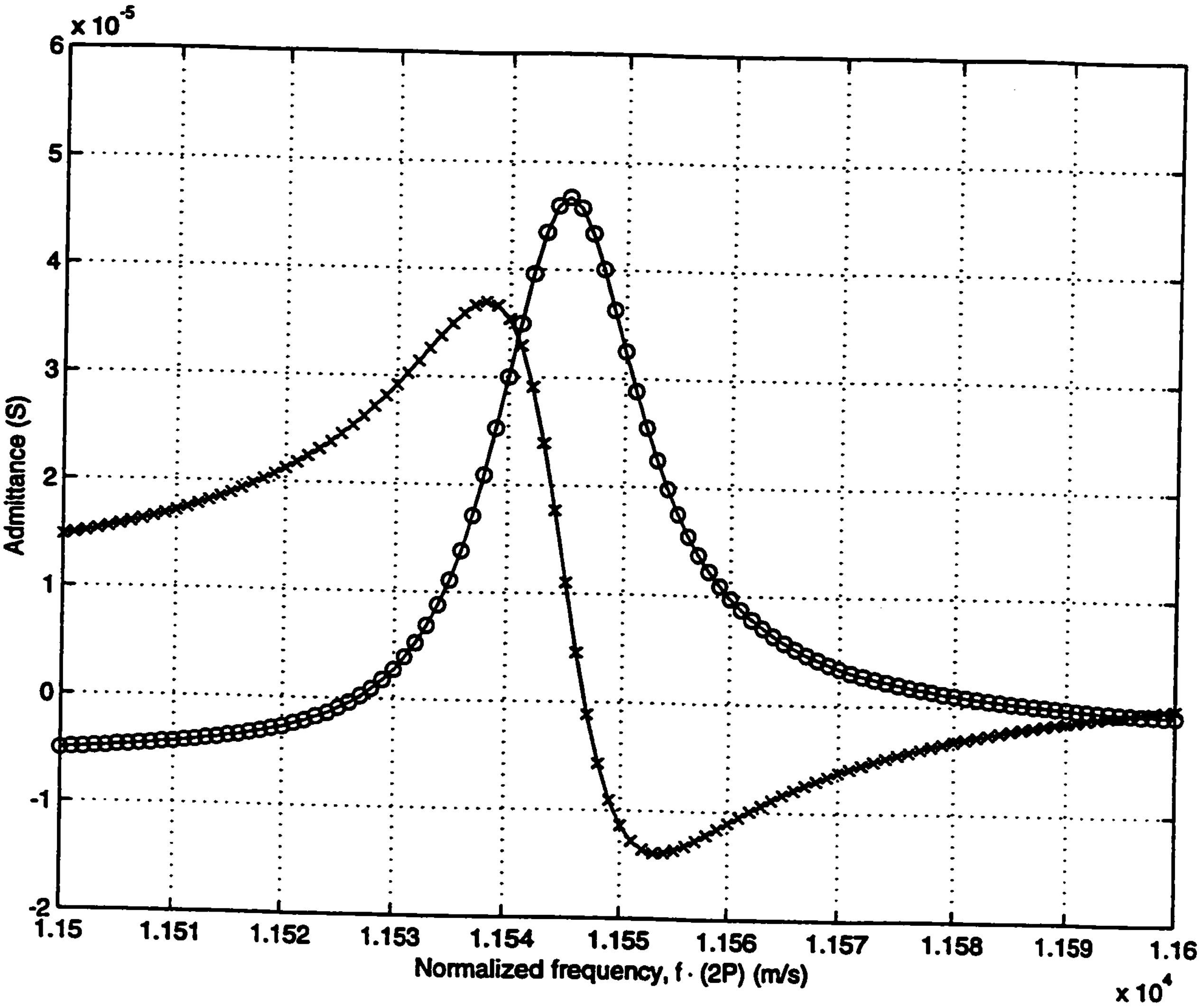

Figure 3.39: The conductance curves for the second Sezawa mode when $H_Z = P/\pi$ and $H_A = 0.005P$ calculated from the Hilbert transform. Calculated susceptance '×', and conductance 'o' calculated from the Hilbert transform.

magnitudes are maximum at this time instance. The magnitude of the displacement is about $10 \times 10^{-10}(m)$ for U_1 at the Al/ZnO interface. On the other hand, the magnitude for U_3 is around $2 \times 10^{-10}(m)$ at the Al/ZnO interface, and it grows inside the diamond substrate until it reaches $4 \times 10^{-10}(m)$. In terms of the electrostatic potential, it becomes very large inside ZnO and dies out quickly inside the diamond layer.

The transduction parameter is estimated from the calculated susceptance curve by using the derivation in Sec. 2.6. We have

$$\frac{|\zeta \cdot (2P)|^2}{\omega_0 C_P} = 0.835\% \tag{3.88}$$

for the second Sezawa mode when $H_Z = P/\pi$ and $H_A = 0.005P$. This value is about 5 % less than that (0.879%) estimated from the dispersion property in fig. 3.30.

3.6 Conclusion

In this chapter, we have presented the space harmonic analysis of acoustic wave propagation and excitation under infinite grating structures on ZnO/Diamond multi-layered substrates. We have extended the SHM model to include multi-layered structures and to the wave generation problem. The dispersion diagrams are obtained for wavenumbers around the first Bragg wavenumber. From the dispersion curves, we theoretically derive the COM parameters, including the self coupling coefficient, the mutual coupling coefficient and the transduction coefficient, which can be used for

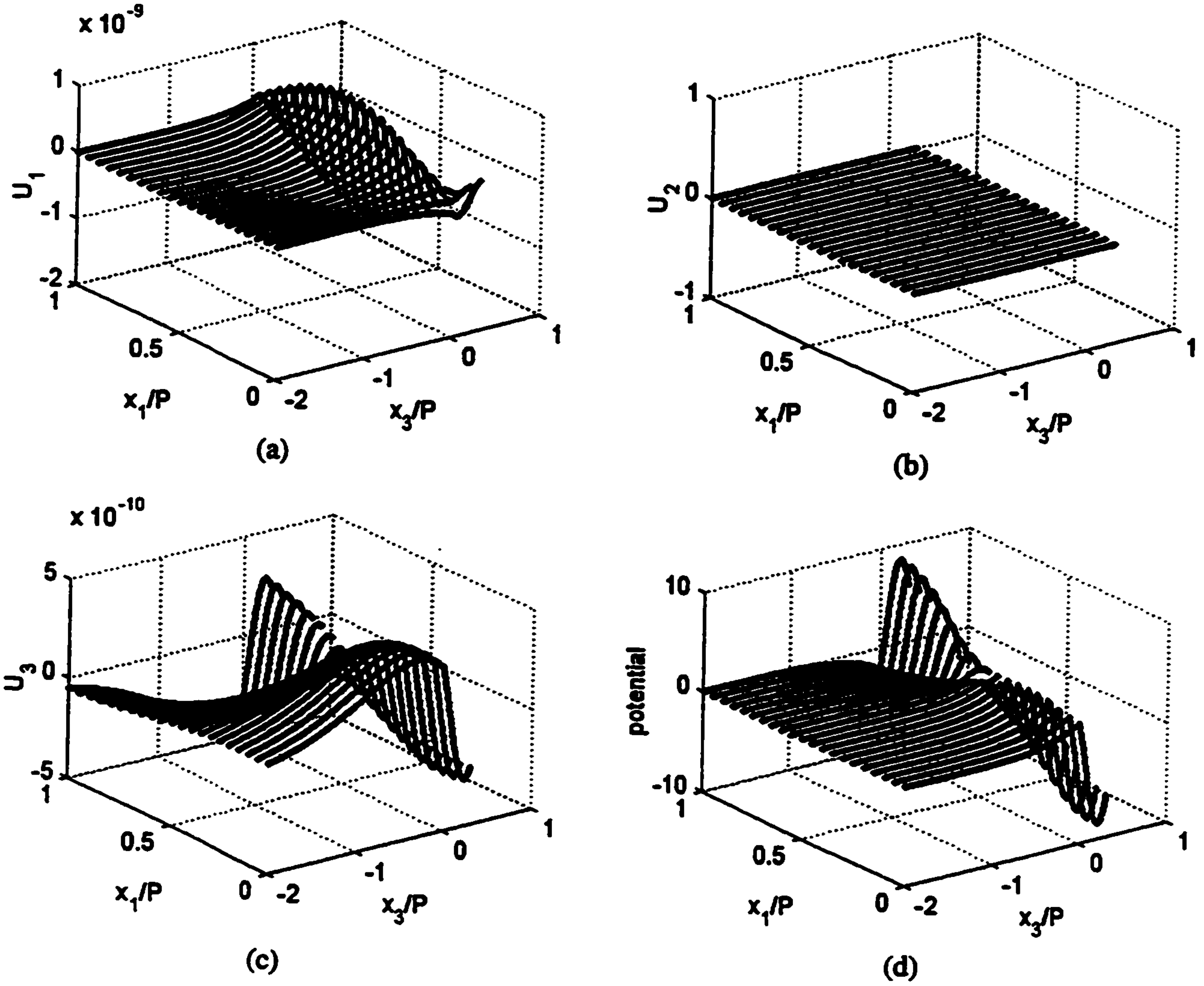

Figure 3.40: Displacement distribution of the second Sezawa mode for an applied voltage of $1(V)$. $H_Z = P/\pi$ and $H_A = 0.005P$. $f \cdot 2P = 11,544(m/s)$. (a)Displacement distribution in the x_1 direction. (b)Displacement distribution in the x_2 direction. (c)Displacement distribution in the x_3 direction. (d)Potential distribution.

device design. The self coupling coefficient increases linearly as a function of the Al thickness both for the first and the second Sezawa modes. The mutual coupling coefficient for the second Sezawa wave decreases as the Al thickness increases and becomes 0 around $H_A = 0.006P$ when $H_Z = P/\pi$ and $H_A = 0.004P$ when $H_Z = 1.5P/\pi$, where it changes to a negative value. The mutual coupling coefficient for the first mode also decreases as a function of the Al thickness. However, it changes from a positive real value to a positive imaginary around $H_A = 0.008P$, which means a $\lambda/8$ difference between the centers of transduction and of reflection. This, however, does not lead to the natural single phase unidirectionality on a uniform grating structure on a symmetrical ZnO/Diamond substrate. The transduction coefficient is insensitive or slightly dependent on the Al thickness regardless of the mode.

The calculated displacement distributions show the typical characteristics of a higher order Sezawa wave. The energy distributions inside each layer are calculated, and they shows that the energy of the second mode inside the diamond and the ZnO layer are similar in magnitude when $H_Z = P/\pi$. For $H_Z = 1.5P/\pi$, the energy inside the diamond reduces to 30% of that inside ZnO, due to the thicker ZnO layer. The energy inside the diamond turns out to be concentrated to within 2 wavelengths of the ZnO/Diamond interface.

From the wave generation analysis using the SHM method, we have calculated the admittance curves as a function of the frequency of the applied voltage. The conductance curve can not be calculated by the SHM based on the Floquet's theorem, due to the assumption of an infinite structure. The static capacitance of one electrode pair can be calculated theoretically, and the result is also necessary for SAW filter design by the COM method. We can show that the calculated admittance curve can be used as an alternative way of estimating the COM parameters as shown in Sec. 2.6 and Sec. 3.5.

Chapter 4

Conclusion

The SAW propagation and generation under an infinite grating structure on ZnO/Diamond multi-layered substrates have been studied in this Thesis. We have established rigorous analytical methods for the evaluation of SAW propagation and excitation properties on multi-layered structures with surface electrodes. In these analyses, both electrical and mechanical perturbations due to the existence of the surface electrodes are considered for an arbitrary shape of grating electrode.

In Chap.2, we review the coupling-of-mode (COM) theory and the COM equations. This Chapter forms a basis for the interpretations of the calculated results obtained by the analytical models, which are explained in Chap.3. The general COM equations are derived from the first principles. The relations between the two commonly used sets of COM equations are clarified. The dispersion diagrams are obtained from the COM equations, and the relations between the unknown COM parameters and the stopband edges are derived. SAW generation phenomena are also discussed and related to the COM equations. The admittance curve as a function of the frequency of an applied voltage is obtained in terms of the COM parameters.

In Chap.3, the space harmonic method (SHM) is discussed. The SHM is extended to the SAW propagation analysis under shorted and open grating structures on ZnO/Diamond multi-layered substrates. Dispersion diagrams are calculated around the first Bragg wavenumber, where stopbands of finite width are observed. The COM parameters (the self coupling coefficient, the mutual coupling coefficient and the transduction coefficient) are evaluated theoretically from the calculated dispersion diagrams, based on the relations discussed in Chap.2. These parameters are obtained for several ZnO and Al thickness conditions and different propagation modes. We found that the self coupling coefficient increases linearly as a function of the Al grating thickness both for the first and the second Sezawa modes. The mutual coupling coefficient for the second mode changes from a positive real value to a negative real value as the grating thickness increases, which leads to a situation with no reflections at some specific Al thickness. For the first mode for $H_Z = 1.75P/\pi$, the mutual coupling coefficient becomes a pure imaginary value when H_A is larger than $0.008P$. This indicates a $\lambda/8$ difference between the centers of transduction and reflection.

We also examine the physical propagation behaviour of ZnO/Diamond multi-layered substrates, which gives us a better understanding of the SAW propagation and generation inside multi-layered substrates. The displacement distributions and the standing wave patterns are calculated inside ZnO/Diamond substrates. We calculate and compare the energy density distribution inside each layer. The ratio of the energy inside diamond to that inside ZnO decreases almost linearly as the thickness of ZnO increases regardless of the mode, 71% for $H_Z = P/\pi$ and 7% for $H_Z = 1.75P/\pi$. The energy inside the diamond layer is concentrated to within two wavelengths of the ZnO/Diamond interface.

A modified SHM is also developed to analyse the SAW generation due to an applied voltage under an infinite periodic electrode. The admittance curves are calculated as a function of the frequency of an applied voltage. Another important parameter for the SAW filter design, the static capacitance of one electrode pair, is evaluated from the calculated admittance curve as a function of the Al and ZnO thicknesses. This model is also shown to be useful for evaluating the transduction coefficient.

4.1 Suggestions for future work

As is explained earlier, multi-layered substrates have been gaining wide attention in the modern communications environment due to their possibilities of having high SAW velocity and of combining properties of the materials of each layer. They also give us the unlimited freedom of the selections of the composite materials and their thickness conditions, which may lead to SAW filters with improved performance.

Versatility of multi-layered substrates, on the other hand, have several drawbacks. The design parameters must be extracted for each thickness condition. The SAW properties are also dispersive and very sensitive to the thin layer material thickness, unlike single layer substrates where they are constant. These facts make the conventional experimental parameter extraction unrealistic.

Our established theoretical analyses enable the parameters derivations for any set of the substrate thickness conditions fairly easy without worrying the thickness error of the fabricated thin film. Our methods are easily applied for any multi-layer substrate configurations where the electrode is located either on top of or within the the multi-layered substrate. And, as is shown in [16], our modified SHMs are also easily applied to the leaky SAW problems with the proper selection of the partial waves of the very bottom layer. For example, the first mode on ZnO/Diamond substrate becomes a leaky SAW when the ZnO thickness is thin, and a SAW velocity of around 15,000 m/s is predicted with an acceptable level of propagation loss [19]. The COM parameters of this substrate will be easily derived by a minor change of the program, and would enable the design of 5GHz SAW filters with an electrode width 0.75 μm.

In addition to the ZnO/Diamond substrates, the temperature compensation using SiO_2 layers have been reported [9] [10], with temperature stability better than that of quartz. 2 to 3 GHz retiming filters and resonators are already in the market using SiO_2/IDT/ZnO/Diamond structures. The additional SiO_2 top layer doesn't affect the theoretical framework of our analyses, and the methods can be easily adapted. Moreover, potential narrow band filter applications of these substrates will make a COM based treatment preferable.

The diamond based SAW filter is known to have a high power durability [8], which is qualitatively explained as a high heat transfer coefficient of diamond. A quantitative discussion would be possible by using the physical behaviour analysis, such as energy distribution that we have shown in this study.

For the first Sezawa mode, we found that the centers of the reflection and the transduction are $\lambda/8$ different each other. This is a quite unusual and strange phenomenon, especially for the symmetric ZnO/Diamond substrate. This is predicted not only by the calculated stopbands but also by the standing wave patterns. At first, experimental verification is necessary, and the physics behind this rapid change in the position of the reflection center should be examined with the help of the physical behaviour analysis inside each layer. This effect may have possibile applications in new SAW filter structures.

Bibliography

[1] L. Rayleigh, "On waves propagated along the plane surface of an elastic solid," *Proc. London Math. Soc.*, Vol. 17, pp. 4-11, 1885.

[2] K. Sezawa, "Dispersion of elastic waves propagated on the surface of stratified bodies and on curved surfaces," *Bull Earthq. Res. Inst.*, Vol. 3, pp. 1-18, 1927.

[3] R. M. White and F. W. Voltmer, "Direct piezoelectric coupling to surface elastic waves," *Appl. Phys. Lett.*, Vol. 7, pp. 314-316, 1965.

[4] B. A. Auld, *"Acoustic Fields and Waves in Solids 2nd ed.,"* Robert E. Krieger Publishing Company Inc., Malabar, FL, 1990.

[5] D. P. Morgan, *"Surface-Wave Devices for Signal Processing,"* Elsevier Science Publishing Company Inc., New York, NY, 1991.

[6] S. Shikata, H. Nakahata, K. Higakai, A. Hachigo and N. Fujimori, "1.5GHz SAW bandpass filter using poly-crystalline diamond," *IEEE Ultrasonics Symp. Proc.*, pp. 277-285, 1993.

[7] H. Nakahata, A. Hachigo, K. Higaki, S. Fujii, S. Shikata and N. Fujimori, "Theoretical study on SAW characteristics of layered structures including a diamond layer," *IEEE Trans. Ultrasonics, Ferroelectric. Freq. Contr.*, Vol. 42, No. 2, pp. 362-375, 1995.

[8] K. Higaki, H. Nakahata, K. Kitabayashi, S. Fujii, K. Tanabe, Y. Seki and S. Shikata, "High power durability of diamond surface acoustic wave filter," *IEEE Trans. Ultrasonics, Ferroelectric. Freq. Contr.*, Vol. 44, No. 6, pp. 1395-1400, 1997.

[9] H. Nakahata, H. Kitabayashi, S. Fujii, K. Higaki, K. Tanabe and S. Shikata, "Fabrication of 2.5GHz SAW retiming filter using SiO_2/ZnO/Diamond structure," *IEEE Ultrasonics Symp. Proc.*, pp. 285-288, 1996.

[10] H. Nakahata, H. Kitabayashi, T. Uemura, A. Hachigo, K. Higaki, S. Fujii, Y. Seki, K. Yoshida and S. Shikata, "Study on surface acoustic wave characteristics of SiO_2/Interdigital-Transducer/ ZnO/Diamond structure and fabrication of 2.5 GHz narrow band filter," *Jpn. J. Appl. Phys.*, Vol. 37, No. 5B, pp. 2918-2922, 1998.

[11] W. R. Smith, "Analysis of Interdigital Surface Wave Transducers," *IEEE Trans.*, MTT-17, 856-864, 1969.

[12] R. C. Peach, "A general Green function analysis for SAW devices," *IEEE Ultrasonics Symp. Proc.*, pp. 221-225, 1995.

[13] W. Liu and P. M. Smith, "Dyadic Green's functions for SAW and leaky wave devices," *IEEE Ultrasonics Symp. Proc.*, pp. 93-98, 1997.

[14] M. Koshiba, S. Mitobe and M. Suzuki, "Finite-element solution of periodic waveguides for acoustic waves," *IEEE Trans. Ultrasonics, Ferroelectric. Freq. Contr.*, Vol. 34, No. 4, pp. 472-477, 1987.

[15] M. Koshiba, N. Shichishima, K. Ohbuchi and Y. Tsuji, "Software for a multilayered surface acoustic wave device based on the finite element method and coupling-of-mode theory," *Jpn. J. Appl. Phys.*, Vol. 36, No. 5B, pp. 3060-3063, 1997.

[16] T. Sato and H. Abe, "Propagation of longitudinal leaky surface waves under periodic metal grating structure on lithium tetraborate," *IEEE Trans. Ultrasonics, Ferroelectric. Freq. Contr.*, Vol. 45, No. 2, pp. 394-408, 1998.

[17] R. F. Milsom, N. H. C. Reilly and M. Redwood, "Analysis of generation and detection of surface and bulk waves by interdigital transducers," *IEEE Trans. Son. Ultrason.*, Vol. SU-24, No. 3, pp. 147-166, 1977.

[18] C. Wang and D. P. Chen, "Generalized Green's functions of surface excitation of elastic wave fields in a piezoelectric half-space," *Chinese J. of Acoustics*, Vol. 4, No. 4, pp. 297-313, 1985.

[19] E. L. Adler, "SAW and pseudo-SAW properties using matrix methods," *IEEE Trans. Ultrasonics, Ferroelectric. Freq. Contr.*, Vol. 41, No. 6, pp. 876-882, 1994.

[20] P. M. Smith, "Dyadic Green's functions for multi-layer substrates," *IEEE Ultrasonics Symp. Proc.*, pp. 137-141, 1999.

[21] P. Ventura, J. M. Hode and M. Solal, "A new efficient combined FEM and periodic Green's function formalism for the analysis of periodic SAW substrates," *IEEE Ultrasonics Symp. Proc.*, pp. 263-268, 1995.

[22] J. Koskela V. P. Plessky and M. M. Salomaa, "Suppression of the leaky SAW attenuation with heavy mechanical loading," *IEEE Trans. Ultrasonics, Ferroelectric. Freq. Contr.*, Vol. 45, No. 2, pp. 439-449, 1998.

[23] Q. Xue and Y. Shui, "Analysis of leaky-surface-wave propagating under periodic metal grating," *IEEE Trans. Ultrasonics, Ferroelectric. Freq. Contr.*, Vol. 37, No. 1, pp. 13-25, 1990.

[24] V. M. Bright and W. D. Hunt, "Analysis of Bleustein-Gulyaev wave propagation under thin periodic metal electrodes," *J. Appl. Phys.*, Vol. 70, No. 2, pp. 594-602, 1991.

[25] H. Meier, B. Schneiderbauer and P. Russer, "Propagation of leaky surface acoustic waves under thin periodic metal electrodes," *IEEE Ultrasonics Symp. Proc.*, pp. 441-444, 1992.

[26] T. Sato, Y. Ohkubo and H. Abe, "Propergation of longitudinal leaky surface waves under periodic SiO_2/Al structure on $Li_2B_4O_7$ substrate," *IEEE Trans. Ultrasonics, Ferroelectric. Freq. Contr.*, Vol. 46, No. 2, pp. 383-391, 1999.

[27] J. R. Pierce, "Coupling of modes of propagation," *J. Appl. Phys.*, Vol. 25, No. 2, pp. 179-183, 1954.

[28] H. Kogelnik, "Coupled wave theory for thick hologram gratings," *Bell System Technical Journal*, Vol. 48, No. 2, pp. 2909-2947, 1969.

[29] A. Yariv, "Coupled wave theory for guided wave optics," *IEEE J. Quant. Electron.*, Vol. QE-9, No. 2, pp. 919-933, 1973.

[30] Y. Suzuki, H. Shimizu, M. Takeuchi, K. Nakamura and A. Yamada, "Coupled wave theory for guided wave optics," *IEEE Ultrasonics Symp. Proc.*, pp. 297-302, 1976.

[31] Y. Koyamada and S. Yoshikawa, "Coupled mode analysis of a long IDT," *Rev. Electrical Comm. Labs.*, Vol. 27, pp. 432-444, 1979.

[32] M. Koshiba and S. Mitobe, "An analysis of reflection characteristics of Surface-Acoustic-Wave gratings," *Jpn. J. Appl. Phys.*, Vol. 27, Suppl. 27-1, pp. 148-150, 1988.

[33] Z. H. Chen, M. Takeuchi and K. Yamanouchi, "Analysis of the film thickness dependence of a single-phase unidirectional transducer using the coupling-of-mode

theory and the finite-element method," *IEEE Trans. Ultrasonics, Ferroelectric. Freq. Contr.*, Vol. 39, No. 1, pp. 84-92, 1992.

[34] D. P. Chen and H. A. Haus, "Analysis of metal-strip SAW gratings and transducers," *IEEE Trans. Sonics Ultrason.*, Vol. SU-32, No. 3, pp. 395-408, 1985.

[35] M. Takeuchi and K. Yamanouchi, "Field analysis of SAW single-phase unidirectional transducers using internal floating electrodes," *IEEE 1988 Ultrasonics Symp. Proc.*, pp. 57-61, 1988.

[36] T. Sato and H. Abe, "Prapagation properties of longitudinal leaky surface waves on lithium tetraborate," *IEEE Trans. Ultrasonics, Ferroelectric. Freq. Contr.*, Vol. 45, No. 1, pp. 136-150, 1998.

[37] G. Tobolka, "Mixed matrix representation of SAW transducers," *IEEE Trans. Son. Ultrason.*, Vol. SU-26, No. 6, pp. 426-428, 1979.

[38] C. K. Campbell, *"Surface acoustic wave devices for mobile and wireless communication.,"* Academic Press, Inc., 1998.

[39] J. Koskela, V. P. Plessky and M. M. Salomaa, "SAW/LSAW COM parameter extraction from computer experiments with harmonic admittance of a periodic array of electrodes," *IEEE Trans. Ultrasonics, Ferroelectric. Freq. Contr.*, Vol. 46, No. 4, pp. 806-816, 1999.

[40] H. Nakahata, K. Higaki, S. Fujii, A. Hachigo, K. Kitabayashi, K. Tanabe, Y. Seki and S. Shikata, "Theoretical study on SAW characteristics of layered structures including a diamond layer," *IEEE Ultrasonics Symp. Proc.*, pp. 361-370, 1995.

[41] H. Nakahata, A. Hachigo, S. Shikata and N. Fujimori, "High frequency surface acoustic wave filter using ZnO/diamond/Si structure," *IEEE Ultrason. Symp. Proc.*, pp. 377-380, 1992.

[42] J. J. Campbell and W. R. Jones, "A method for estimating optical crystal cuts and propagation directions for excitation of piezoelectric surface waves," *IEEE Trans. Son. Ultrason.*, Vol. SU-15, No. 3, pp. 209-217, 1968.

[43] R. V. Schmidt and F. W. Voltmer, "Piezoelectric elastic surface waves in anisotropic layered media," *IEEE Trans. Microwave Theory and Technique,*, Vol. MTT-17, No. 11, pp. 920-926, 1969.

[44] C. S. Hartmann, P. V. Wright, R. J. Kansy and E. M. Garber, "An analysis of SAW interdigital transducers with internal reflections and the application to the design of single-phase unidirectional transducers," *IEEE Ultrasonics Symp. Proc.*, pp. 40-45, 1982.

[45] K. Yamanouchi and H. Furuyashiki, "New lowl-loss SAW filter using internal floating electrode reflection types of single-phase unidirectional transducer," *Electronics Lett.*, Vol. 20, pp. 989-990, 1984.

[46] M. Takeuchi and K. Yamanouchi, "Coupled mode analysis of SAW floating electrode type unidirectional transducers," *IEEE Trans. Ultrasonics, Ferroelectric. Freq. Contr.*, Vol. 40, pp. 648-658, 1993.

[47] P. V. Wright, "The natural single-phase unidirectional transducer: A new low-loss SAW transducer," *IEEE Ultrasonics Symp. Proc.*, pp. 58-63, 1985.

[48] W. R. Smith, "Analysis of interdigital surface wave transducers," *IEEE Trans. Microwave Theory and Technique,*, Vol. MTT-17, No. 11, pp. 856-864, 1969.

[49] E. L. Adler and L. Solie, "ZnO on diamond: SAWs and pseudo-SAWs," *IEEE Ultrasonics Symp. Proc.*, pp. 341-344, 1995.